# ABSTRACT


| | |
|---|---|
| Title of Dissertation: | MEASURING AND TRAPPING QUASIPARTICLES IN SUPERCONDUCTING COPLANAR WAVEGUIDE RESONATORS |
| | Ashish Alexander, Doctor of Philosophy, 2021 |
| Dissertation directed by: | Dr. Christopher Richardson, Laboratory of Physical Sciences |



Measuring the internal quality factor of coplanar waveguide superconducting resonators is an established method of determining small losses in superconducting devices. Traditionally, the resonator losses are only attributed to two-level system (TLS) defects using a power dependent model for the quality factor. However, excess non-equilibrium quasiparticles can also limit the quality factor of the planar superconducting resonators used in circuit quantum electrodynamics. At millikelvin temperatures, quasiparticles can be generated by breaking Cooper pairs via high-energy particles or sub-gap microwave photons from the measurement signal.

In this thesis, I developed a two-temperature, power, and temperature dependent model to evaluate resonator losses for isolating TLS and quasiparticle loss simultaneously. The model combines a standard TLS model with a new modified two-temperature quasiparticle model where the driven quasiparticle density is defined by an effective temperature that may be different than the bath temperature. This model

also explores the power and temperature dependence of the internal quality factor. To investigate the model, resonators were fabricated from epitaxial molecular beam epitaxy-grown aluminum and titanium nitride grown on float-zone refined silicon. The resonators have high-quality factors above 1M. The presented model is used to determine that the analyzed TiN resonator had comparable TLS and quasiparticle loss at low power and low temperature, while the low-temperature Al resonator behavior was dominated by non-equilibrium quasiparticle loss.

Additionally, a small bandgap superconductor in contact with a larger bandgap superconductor as a quasiparticle trap is also explored. The quasiparticles can be confined away from the larger bandgap superconductor into the smaller one. Here, Al and TiN were used as two superconductors. Finite difference method (FDM) simulations of the coupled phonon and quasiparticle systems of both superconductors are performed, suggesting that the quasiparticle traps on the ground plane may be effective for setback distances less than 200 μm away from TiN waveguide features. Experimentally, a thin layer of Al is grown in-situ on TiN using molecular beam epitaxy (MBE) with a negligible dielectric layer between the two superconductors to increase the trapping efficiency of the Al. The quarter-wavelength resonators in TiN with an Al layer with varying setback distances (1 μm – 150 μm) from the active region of the TiN were also fabricated using custom-designed mask sets. These devices are then analyzed for different powers and temperatures. The resonators with setback greater than 20 μm outperform the plain TiN resonators at low temperatures. The device with a setback of 150 μm had 1.5x the quality factor at medium powers at low temperatures.

# MEASURING AND TRAPPING QUASIPARTICLES IN SUPERCONDUCTING COPLANAR WAVEGUIDE RESONATORS

by

Ashish Alexander

Dissertation submitted to the Faculty of the Graduate School of the
University of Maryland, College Park, in partial fulfillment
of the requirements for the degree of
Doctor of Philosophy
2021

Advisory Committee:
Professor Julius Goldhar, Chair
Dr. Christopher Richardson. Co-Chair/Advisor
Prof. Steven Anlage
Prof. Romel Gomez
Prof. Frederick Wellstood, Dean's Representative

# Dedication

To my mom and dad, wife Mini, little Abigail, and

the One to whom all the glory is due.

# Acknowledgements

First and foremost, I would like to thank my research advisor, Dr. Christopher Richardson, for being an excellent role model. Thank you for introducing me to the world of superconducting resonators and teaching me new experimental techniques. His mentorship and direction helped me become a better researcher by emphasizing rigor and detailed analysis to understand any experiment results better. I also thank him for all the MBE-grown thin films for devices used in the thesis.

I would like to thank Professor Julius Goldhar, my academic advisor, for all the guidance and assistance over the years. His timely advice has always pushed me to improve my work.

I also take this opportunity to thank the members of my defense committee for taking time out of their busy schedules. I genuinely appreciate their response and constructive feedback towards my thesis and the defense.

I would especially like to thank Chris Weddle for his help with the packaging of resonator dies and operating ADR. I would also like to thank all of my present and former lab mates at LPS (Margaret Samuels, Chris Weddle, Nathan Siwak, Brian McSkimming, Chomani Gaspe, Kevin Dwyer, Austin Thomas, Thomas Farinha, Alan Kramer, Nicholas Grabon) for their time in regular technical and fun discussions. These productive discussions always helped me to learn more and think outside the box to find solutions.

I would like to thank the members of the cleanroom staff (Toby Olver, Jim Fogleboch, Steve Brown, Dan Hinkel, Warren Berk, Curt Walsh, and Paul Hannah) for

their assistance in device fabrication procedures, the many hours of cleanroom training, and patient help in maintenance.

I also thank the machinists Donald Crouse and Ruben Brun in the LPS machine shop for always being ready to help fabricate different parts essential for my experiments.

I would also like to thank my friends and teachers who have motivated me to pursue my dreams and achieve this far. I thank my church family for their prayer support.

Finally, I would like to thank my mother, Susan, and my father, Alexander, for their love, support, and motivation throughout this journey. And also, my mother-in-law, Mary, for tirelessly rustling up delicious dishes to keep me motivated in my final leg of this journey. I thank my wife, Mini, for her patience, love, support, and comfort through this journey. My little Abigail, thank you for making the past year a lot more fun and rewarding.

# Table of Contents

# List of Tables

# List of Figures

# List of Abbreviations

| | |
|---|---|
| QED | Quantum Electrodynamics |
| MBE | Molecular Beam Epitaxy |
| ADR | Adiabatic demagnetization refrigerator |
| TLS | Two-level system |
| QP | Quasiparticles |
| CPW | Coplanar waveguide |
| BCS | Bardeen Cooper Schrieffer theory of superconductivity |
| RF | Radio frequency |
| TiN | Titanium Nitride |
| Al | Aluminum |
| DC | Direct Current |
| PCB | Printed circuit board |

# Symbols

| | |
|---|---|
| $\Delta$ | Superconducting gap parameter |
| $2\Delta$ | Bandgap of superconductor |
| $k_B$ | Boltzmann constant |
| $\hbar$ | Plank's constant |
| $N(0)$ or $N_o$ | normal state single-spin density of states at the fermi level |
| $n_{qp}$ | Quasiparticle number density |
| $n_{cp}$ | Cooper pair number density |
| $w$ | Width of the central conductor of CPW resonator |
| $g$ | Gap between the central conductor and ground plane |
| $f(E)$ | Fermi Dirac distribution |
| $\rho(E)$ | Density of states of quasiparticles |
| $\omega_{res}$ | Resonator resonance frequency |
| $\lambda_o$ | Wavelength corresponding to a resonant frequency |
| $n_p$ | Average photons present in the resonator |

| | |
|---|---|
| $T_c$ | Critical temperature |
| $T_b$ | Bath temperature |
| $T_{qp}$ | Effective quasiparticle temperature |
| $Q_I$ | An internal quality factor of a resonator |
| $Q_c$ | Coupling quality factor |
| $Q_T$ | Total quality factor |
| $Q_{TLS}$ | Quality factor corresponding to TLS and is inverse of TLS loss |
| $Q_{TLS}^o$ | Temperature and power independent TLS loss prefactor. Characteristic of material properties. |
| $n_c$ | Critical photon number of TLS loss |
| $\alpha$ | Power exponent in TLS loss |
| $Q_{QP}$ | Quality factor corresponding to quasiparticle |
| $I_{ext}$ | External quasiparticle generation rate |
| $s$ | Quasiparticle trapping rate |
| $\kappa$ | Phenomenological excess quasiparticle loss parameter |
| $Q_A$ | Non-TLS, non-QP temperature and power independent quality factor |
| $n_{qp}$ | Quasiparticle number density |
| $x_{qp}$ | Normalized quasiparticle number density |
| $s_b$ | Setback distance. The distance of the quasiparticle trap from the CPW ground plane edge |

# Chapter 1 : Introduction

## *1.1 Quantum Computing*

Quantum computing[1], [2] is a form of computing that harnesses quantum effects such as quantum superposition and entanglement to process information. In a quantum computer, information is stored in quantum bits or "qubits" instead of conventional binary bits. A qubit can be treated as a pair of pure quantum states of a quantum system, which are denoted as $|0\rangle$ and $|1\rangle$. Often, the two states of the qubits are the ground and the excited state of a physical system. The quantum nature of the qubit allows the system to be placed in a coherent superposition of the $|0\rangle$ and $|1\rangle$ states according to,$|\psi\rangle = \alpha|0\rangle + \beta\,|1\rangle$ where $|\alpha|^2 + |\beta^2| = 1$. The quantum state of a single qubit can be represented on the Bloch sphere, as shown in Fig. 1.1(a), with $|\psi\rangle$ written as following

$$\psi\rangle = \cos\left(\frac{\theta}{2}\right)|0\rangle + e^{i\Phi}\sin\left(\frac{\theta}{2}\right)|1\rangle \tag{1.1}$$

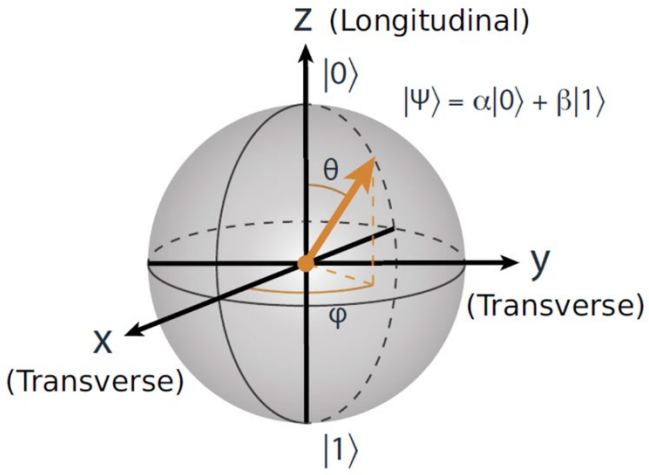


*Fig. 1.1: Bloch sphere representing the state of a qubit* $|\psi\rangle = cos\left(\frac{\theta}{2}\right)|0\rangle + e^{i\phi}sin\left(\frac{\theta}{2}\right)|1\rangle$. *Figure is from ref.*[3]

In an open quantum system, such as a qubit that is not isolated from the environment, the qubit can lose information due to coupling with the environment. The useful computational lifetime of a qubit is defined by a few characteristic rates. First, in the presence of external noise, a qubit in its excited state can lose energy and relax to the ground state, i.e., $|1\rangle \rightarrow |0\rangle$, with an exponential decay rate denoted by $\Gamma_1 = 1/T_1$. Second, the fluctuation in the qubit frequency due to external noise or interaction with other quantum systems can lead to dephasing of the qubit, which is described by the dephasing rate $\Gamma_\phi = 1/T_\phi$. Third, coherence time (denoted by $T_2$) defines another timescale for which the qubit retains useful quantum information. It depends on both $T_1$ and $T_\phi$ which is given as

$$\frac{1}{T_2} = \frac{1}{2T_1} + \frac{1}{T_\phi}. \tag{1.2}$$

Fig. 1.2 shows an illustration of relaxation, dephasing, and coherence time in a Bloch sphere.

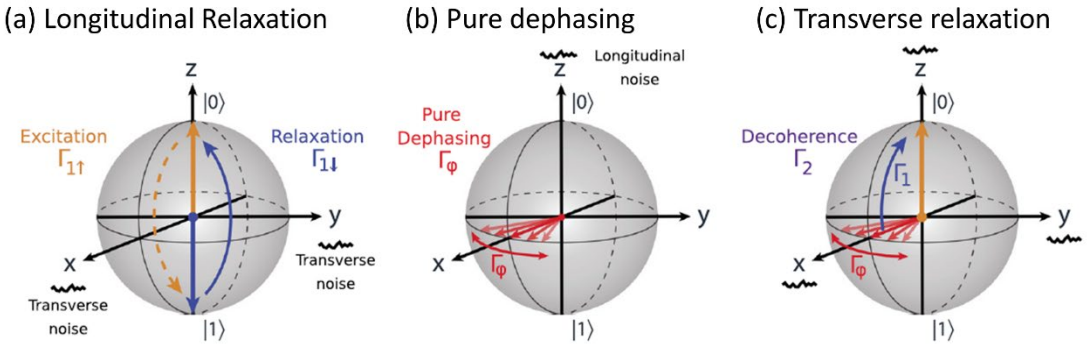


*Fig. 1.2: (a) Longitudinal relaxation of the qubit from* $|1\rangle$ *to* $|0\rangle$ *with a characteristic time,* $T_1=1/\Gamma_1$ *(b) Loss of the information in the transverse plane with dephasing time* $T_\phi = 1/\Gamma_\phi$. *(c) Coherence time* $T_2$ *results from the combination of both longitudinal relaxation and pure dephasing Figure is from ref.*[3]

Fig. 1.3 shows the relaxation and coherence time for a transmon qubit.

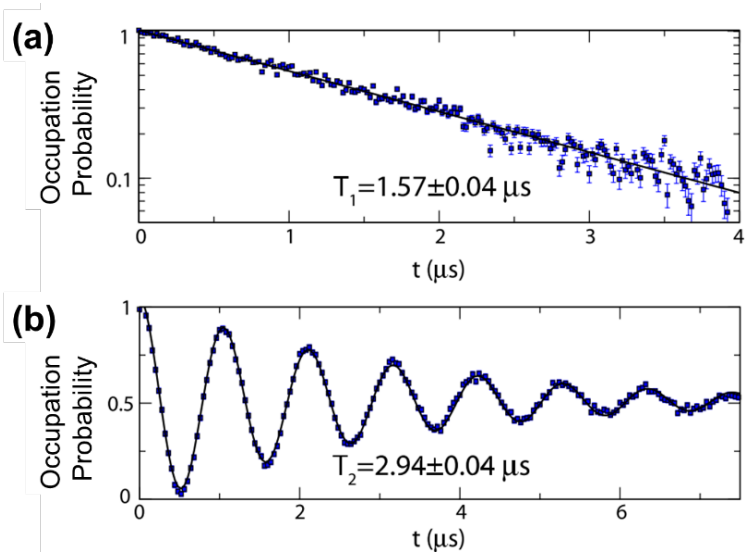


*Fig. 1.3: (a) Plot showing the relaxation of a transmon qubit from* $|1\rangle$ *to* $|0\rangle$ *with a characteristic time* $T_1$ *and (b) Spin echo measurement with dephasing time* $T_2$*. Figure is from ref.* [4]

The present day transmon qubits are not robust and lose the state's information relatively quickly compared to the typical gate operation time causing limitations on performing complex quantum computations.

The suitability of a quantum system for practical computations can be assessed using the DiVincenzo criteria[5]. They are as follows:

(1) Scalability of well-characterized qubits

(2) The ability to initialize the qubits in a well-determined quantum state.

(3) Availability of universal set of gates for computation

(4) Coherence times need to be longer than gate operation times

(5) Availability of qubit-specific measurement capability

Two additional criteria required for quantum communication are

(6) Interconversion between stationary and flying (moving) qubits

(7) Faithful transmission of flying qubits.

Additional practical requirements would be reproducible components, simple fabrication, and low operating costs from an engineering perspective.

Based on the above criteria, there are several ways the solid-state qubits have been engineered using a wide variety of material systems, including trapped ions, electron spins quantum dots, nitrogen vacancies in diamond, and superconducting circuits[6]. Ion trap qubits use alkali metal-like ions such as calcium and strontium to form qubits from the hyperfine electronic states of the ion as quantum states [7]. Qubits realized from quantum dots made out of silicon and germanium using electron spin states in electrostatically defined quantum dots as their quantum states[8]. The electronic spin states of the nitrogen-vacancy defect in a diamond can also define a qubit [9]. Similarly, qubits can be realized from superconducting quantum circuits created from aluminum, niobium, or titanium nitride thin films, where different states of an anharmonic resonator circuit serve as the quantum states[10].

## *1.2 Superconducting Qubits*

The development of qubits using superconducting materials is currently one of the significant research areas in quantum computing. Superconducting qubits are designed by lithographically made circuit elements such as wires, capacitors, inductors, and Josephson junctions. The presence of a superconductor ensures very low resistive loss and highly nonlinear and non-dissipating devices in the Josephson junction. Even though the Josephson junction has a macroscopic size, these qubits can display quantum behavior that is similar to that of single atoms. However, like all qubits, superconducting quantum circuits are susceptible to losing information via interactions with the environment, limiting coherence time [11].

Conceptually, a superconducting qubit can be formed by a simple harmonic oscillator formed from an inductor and capacitor. The Hamiltonian of an isolated harmonic oscillator can be written as.

$$\mathrm{H} = 4\mathrm{E_c n^2} + \frac{1}{2}\mathrm{E_L}\phi^2 \tag{1.3}$$

Here the quantum operator $n \equiv \frac{Q}{2e}$ is the excess charge Q on one plate of the capacitor, normalized by the magnitude of the charge of a Cooper pair charge $(2e)$. The reduced flux, or gauge-invariant phase $\phi \equiv \frac{2\pi\Phi}{\Phi_0}$, is the flux, $\Phi$, in the inductor normalized by the superconducting magnetic flux quantum, $\Phi_0$. The capacitive energy, $E_c = (e)^2/(2C)$, is the charging energy corresponding to each electron of a Cooper pair. The inductive energy, $E_L = \frac{\left(\frac{\Phi_o}{2\pi}\right)^2}{L}$, corresponds to the flux quantum.

The system described by Eq. (1.3) is a simple harmonic oscillator with capacitive energy behaving like kinetic energy and inductive energy as potential energy. This Hamiltonian gives equally spaced energy levels described by $H = \hbar\omega_r(a^\dagger a + \frac{1}{2})$ with $a^\dagger$ and $a$ are the creation and annihilation operators, and the resonant angular frequency is $\omega_r = 1/\sqrt{LC}$. In principle, any two levels of this oscillator could form the basis of a qubit. However, the equally spaced energy levels impede the ability to uniquely address just two quantum states by applying an external drive. The introduction of anharmonicity in the system is necessary to break the equal spacing between the energy levels.

A dissipationless Josephson junction behaves as a nonlinear inductor. A Josephson junction can be formed from a thin layer of insulating material sandwiched

between two superconductors. The current flowing through the junction depends on the difference between the superconducting phase of the superconductors on either side ($\phi = \phi_1 - \phi_2$). The key relations describing the Josephson junction are

$$I = I_c \, sin(\phi) \text{ and } V = \Phi_0 \frac{d\phi}{dt} \tag{1.4}$$

where $I_c$ is the critical current of the junction, which depends on the junction geometry and material properties of the insulator and the superconductor. The junction has an effective inductance.

$$L_J = \frac{\Phi_o}{2\pi I_C} \frac{1}{cos(\phi)} \tag{1.5}$$

and modified Hamiltonian of an isolation junction is

$$H = 4E_c n^2 - E_j \, cos(\phi) \tag{1.6}$$

where $E_C = \frac{(e)^2}{2C_\Sigma}, C_\Sigma = C_s + C_j$ is the charging energy, including any shunt capacitor, $C_s$, and junction self-capacitance, $C_j$, while $E_j = \frac{I_c \Phi_0}{2\pi}$ is the Josephson energy. The introduction of the Josephson junction converts the parabolic form of the potential energy to the cosinusoidal form, as shown in Fig. 1.4. For these systems to exhibit their quantum nature, the thermal fluctuations must be smaller than the transition energy between the states of the qubit states. Superconducting quantum circuits typically are chosen to operate in the 2 GHz (96mK) – 20 GHz (960mK) and at temperatures below 50 mK to ensure the qubits are not thermally excited[12].

Superconducting qubits can be broadly categorized into roughly three kinds – charge qubit, flux qubit, and phase qubit based on which quantum degree of freedom is more sharply defined. In a charge qubit, the charging energy $E_C$ is large compared to

$E_j$ and $E_c$ and the junction is controlled by applying a gate voltage source. In flux qubits, $E_c$ effectively dominates and control is achieved by the application of an external flux in a SQUID configuration. For phase qubits, phase is most sharply defined [12], [13]. Fig. 1.5 shows schematics of three different types.

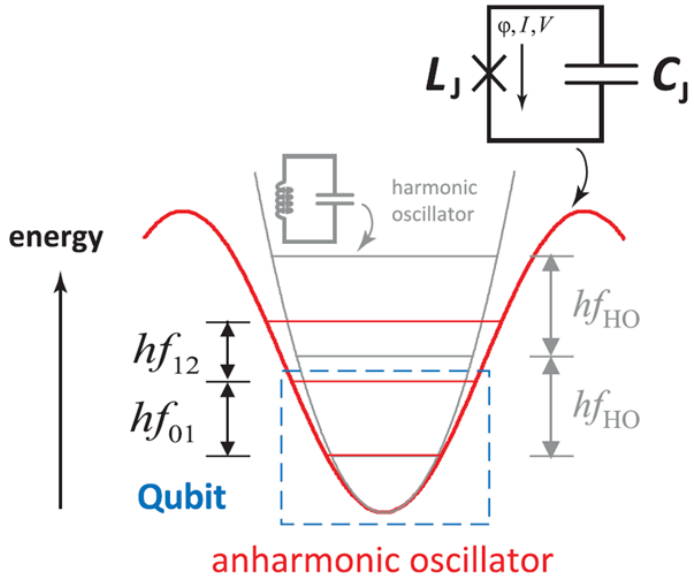


*Fig. 1.4: Energy levels of a harmonic and anharmonic oscillator. Fig. from ref.* [11]. *Nonlinear inductance in the Josephson junction breaks the harmonicity of the LC circuit*

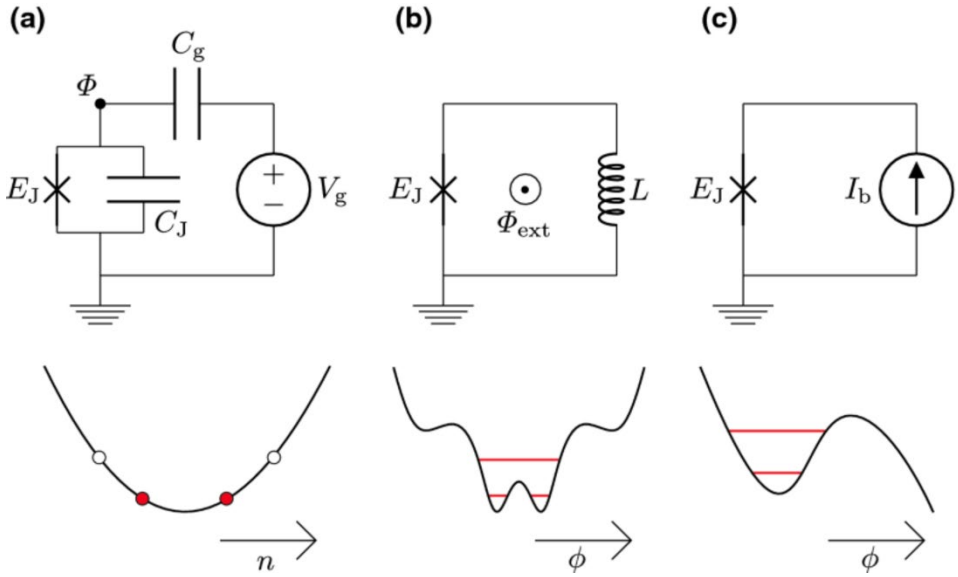


*Fig. 1.5: Schematics of the basic kinds of superconducting qubits (a) charge qubit (b) flux qubit, and (c) phase qubit. The cross represents the Josephson junction. Figure is from ref.*[13]

The transmon qubit is currently the most popular type of superconducting qubit. Transmons typically operate with $E_J/E_c \approx 50$ to reduce the qubit sensitivity to charge noise. The coherence times of qubits can be further boosted by isolating them from the environment by placing them in a resonant cavity that is detuned from the qubit transition frequency. A high-quality resonator only allows coupling to a very narrow band of frequencies, isolating the qubit from the undesired environmental noise. Near the resonance frequency, a resonator photon can be reflected back and forth many times, enhancing the effective coupling of the photon and the qubit. The qubit states also affect the resonant frequency of the qubit-resonator system enabling the resonator as a readout element, as shown in the inset of Fig. 1.6. Here, the interaction of superconducting qubits with resonator's quantized electromagnetic fields is in the microwave regime and is described by the circuit quantum electrodynamics (c-QED) [14].

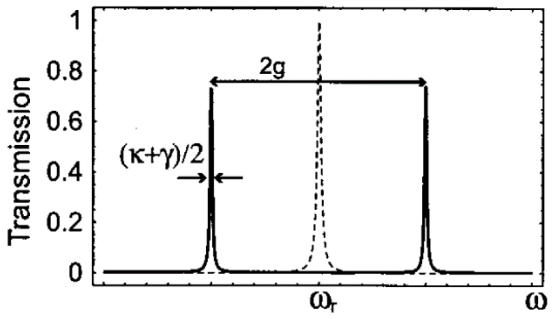


*Fig. 1.6: The resonator response in the absence of qubit(dashed line) and the presence of qubit* [14]

The coupling of the quantum electromagnetic modes of the resonator with the qubit modifies the circuit's Hamiltonian, which can be approximately described by the Jaynes-Cummings Hamiltonian[15],

$$\hat{H} = \hbar\omega_r\left(\hat{a}^\dagger\hat{a} + \frac{1}{2}\right) + \frac{1}{2}\hbar\omega_q\hat{\sigma}_z + \hbar g(\hat{a}^\dagger\hat{\sigma}_- + \hat{a}\hat{\sigma}_+), \tag{1.7}$$

where $\hat{a}^\dagger, \hat{a}$ are the creation and annihilation operators for the resonator. Here the resonant frequency of the resonator is $\omega_r$, and $\omega_q$ is the qubit transition frequency. Also, $\hat{\sigma}_z$ is the Pauli matrix and $\hat{\sigma}_-$ and $\hat{\sigma}_+$ are the creation and annihilation operator of the two-level qubit system. The first term of the Hamiltonian represents the energy of the resonators. The second is for the qubit, while the third represents the coupling between the qubit and the resonator.

In cQED, the resonators can be realized as planar 2-D designs using traditional lithographic techniques or 3-D cavities machined out of metal. A popular implementation of the superconducting qubits in cQED is coupling transmons with a 2-D transmission line resonator, as shown in Fig. 1.7. These devices have roughly shown two orders of magnitude increase in coherence time $T_2$ compared to charge qubit [10].

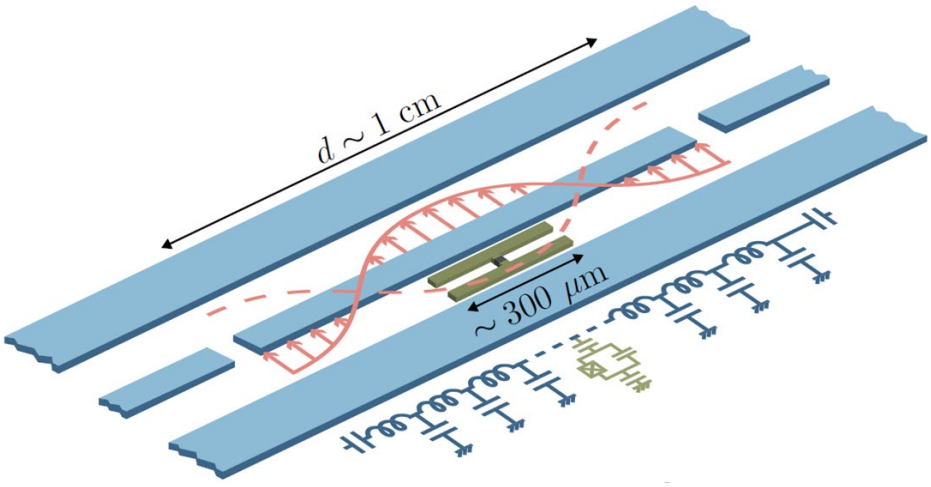


*Fig. 1.7: Schematic of a qubit with a transmon coupled with a resonator. Figure is from ref.* [15]. *The green block represents the transmon qubit.*

## *1.3 Role of resonators*

Resonators form the readout element of the cQED devices and the coherence times of qubits depend on the quality of the resonators. In planar 2D qubit architecture, two-dimensional resonators are realized from coplanar waveguide transmission lines. Additionally, the resonators are relatively easier to fabricate than the qubit. It makes the resonator an excellent tool for optimizing material selection and fabrication techniques to minimize loss. Fig. 1.8 summarizes a set of studies by few groups. Fig. 1.8(a) compares the various aluminum growth techniques by sputtering, E-beam deposition, and MBE. The MBE growth on the surface treated with the activated oxygen at high temperature generates the high-quality single-crystal film with a clean aluminum sapphire interface [16]. Fig. 1.8(b) compares three different etching techniques on titanium nitride resonators on silicon wafers. Fluorine RIE-etch outperforms the chorine RIE-etch and argon mill due to the smoother surface finish and reduced lossy post-etch residues [17]. Fig. 1.8(c) explores the deep etching of silicon substrates for reducing the intrinsic loss of the niobium-titanium nitride resonators. The deep etches moved the lossy surface from the high electric field region and improved the quality factor of the resonators. The resonator's internal quality factor, which is the inverse of the net loss in the resonator, is the metric to evaluate the resonator's quality.

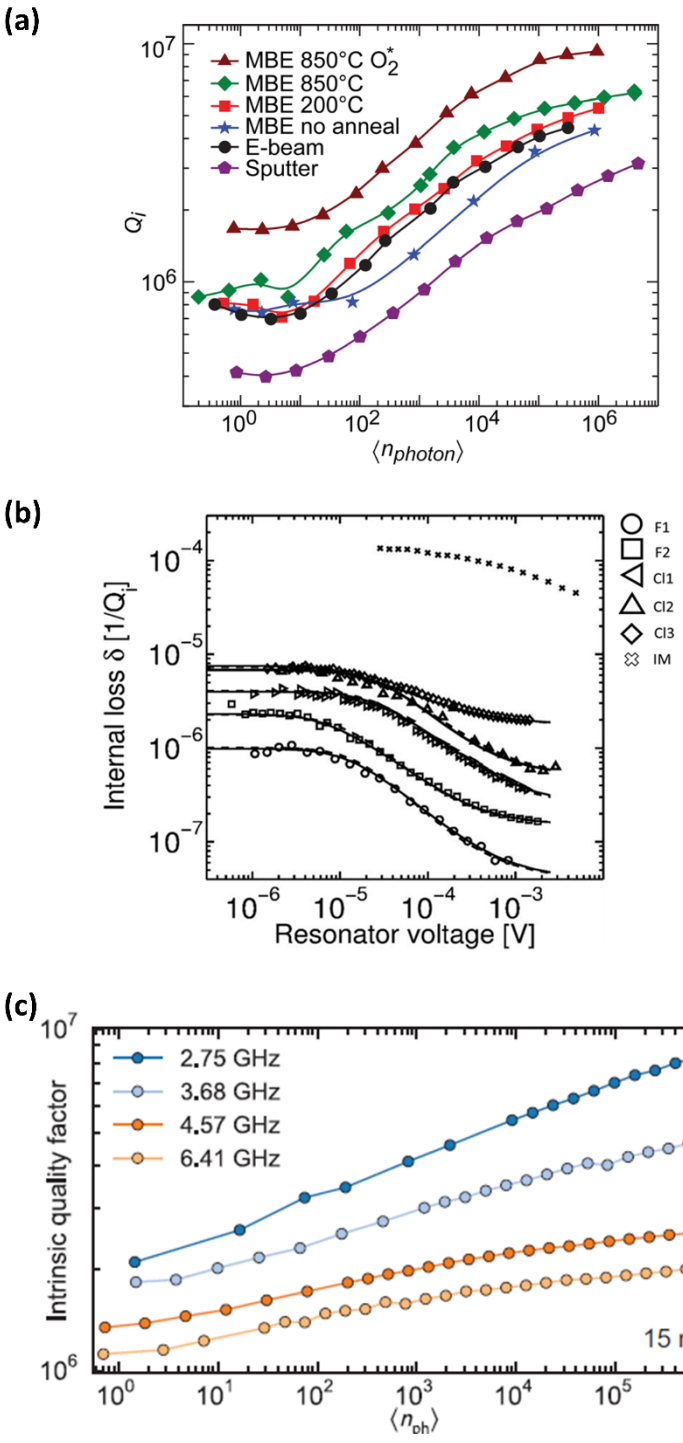


*Fig. 1.8: Resonator as a tool for material and fabrication characterization. (a) Comparison of growth technique*[16] *(b) Comparison of different etch techniques* [17] *(c) Investigation of deep etch in resonator*[18]

## *1.4 Model of power and temperature dependence of resonator quality factor*

As I noted above, resonators can serve as a tool to investigate some non-junction-related loss mechanisms that may also be responsible for loss in qubits. The loss can be expressed as a sum of parallel loss channels. These losses have a unique characteristic dependence on temperature, microwave power, magnetic field, and geometry, as shown in Eq. (1.8).

$$\frac{1}{Q_I} = \frac{1}{Q_{TLS}(T,\ P)} + \frac{1}{Q_{QP}(T,P)} + \frac{1}{Q_{rad}(w)} + \frac{1}{Q_{vortices}(B)} + \frac{1}{Q_{cavity}(\nu, \text{geometry})} \ldots \tag{1.8}$$

Ideally, each of these losses can be isolated and studied by controlling other degrees of freedom. The two-level system losses have microwave power and temperature dependence and may be dominant at low power and low temperature depending on the geometry and materials. Quasiparticles also can contribute to the loss in the resonator. They may or may not have a strong temperature dependence. According to BCS theory, in thermal equilibrium, as the temperature approaches zero, the quasiparticles should vanish, leading to high coherence times in superconducting devices. However, the experimental evidence suggests non-equilibrium quasiparticles [17–19] are found even at the lowest temperatures. These excess quasiparticles can also show a weak dependence on microwave power. Among other loss mechanisms, the loss of the resonator energy through radiation depends on the

resonator dimensions, frequency, and coupling to the outside environment, while losses from vortices depend on the number of trapped vortices and applied magnetic field.

In the literature[16]–[20], resonator performance is commonly quantified by measuring the internal quality factor of the resonator and its dependence on the applied microwave power. The two-level system (TLS) losses are generally used to describe power dependence. The rest of the losses are grouped into a constant loss. Additionally, the temperature dependence of the frequency shift due to $Q_{TLS}$ may also explored. At relatively high temperatures(above 200 mK in Al), the loss is often found to be dominated by thermal quasiparticles. All these losses are analyzed independently. In this thesis, I describe a new integrated temperature and power dependent model for isolating TLS and quasiparticle loss simultaneously.

The model I developed combines a standard temperature and power dependent TLS model and a modified quasiparticle model. In this model, the excess non-thermal quasiparticles are approximated by a thermal distribution described by an effective temperature. I apply the model to understand the loss in resonators at low temperatures where to qubits operate and compare the measurements on aluminum resonators, titanium nitride resonators, and novel quasiparticle trapping resonators.

## *1.5 Superconducting quasiparticle traps for resonator*

The presence of the non-equilibrium quasiparticles impacting the device performance has been an active area of research across various research communities. In superconducting qubits, quasiparticles give an undesired channel of relaxation[21]–[25]. In single-electron transistors[26], [27], they cause large charge fluctuations. Excess quasiparticles can also impact the cooling power in superconducting micro

coolers[28]–[30]. In resonators[31], [32] and kinetic inductive detectors[33], [34], they cause ohmic losses and background noise.

Many different techniques have previously been employed to reduce the density of non-equilibrium quasiparticle density. In the superconducting qubit community, attempts have been made to suppress excess quasiparticle generation by isolating the devices from the environment using the multistage radiation shielding in the fridges[35], improved cooling of signals in the microwave attenuators[36], and coupling quantum circuits with 3D resonant cavity[37]. Excess quasiparticles are confined away from the active regions at the device level by including magnetic flux vortices [25], [38] or normal metal [30], [32], [39], [40], which acts as quasiparticle traps. Both vortices and normal metal provide a zero-band gap, thus providing states for quasiparticles to relax when they enter the trapping layer. In the metal traps, inelastic scattering with electrons or phonons of the metal relaxes the quasiparticle[41]. In this study, I explore A small bandgap superconductor as a quasiparticle trap (instead of a normal metal). The small band gap superconductor, similar to the normal metal, provides lower energy states (compared to the primary superconductor) for the quasiparticle to relax. A theoretical study comparing traps made from normal metals and superconductors shows an increased trapping efficiency for the superconducting traps. They have a higher density of states than a metal trap, reducing the probability of entering quasiparticles to backflow out of the trap. Using superconductor quasiparticle traps also eliminates the resistive loss present in normal metal and can cause additional microwave loss[42].

I fabricated quasiparticle traps on resonator circuits by covering the ground plane with superconducting thin film with a lower critical temperature. Aluminum with $T_c \sim 1.2K$ forms the small bandgap superconductor while TiN with $T_C \sim 5.3K$ forms the large bandgap superconductor. The resonator performance was determined for different configurations of the small bandgap superconductor.

## *1.6 Overview of dissertation*

My dissertation is divided into the following chapters. In Chapter 2, I provide essential background on the resonator basics, two-level systems, and quasiparticle loss. In Chapter 3, I discuss the effective temperature quasiparticle loss model. In Chapter 4, I describe the design criteria of the small bandgap superconductor quasiparticle trap. In Chapter 5, I discuss the experimental methods of fabricating and measuring superconductor quarter-wave coplanar waveguide resonators. In Chapter 6, I explain the temperature and power dependence of the resonator loss for all resonators, and those results are compared with my power-temperature loss model. Chapter 7 summarizes the conclusions and possible directions of future work.

# Chapter 2 : Background

## *2.1 BCS Theory*

Superconductivity is described as the phenomenon when the electric DC resistance of certain materials vanishes below a critical temperature ($T_C$). It is accompanied by a perfect diamagnetism of the material where a penetrating magnetic field is expelled. The microscopic behavior of superconductors can be described by Bardeen-Cooper-Schrieffer (BCS) theory[43]. According to BCS theory, below the critical temperature, electrons close to the Fermi level with opposite spin and momentum can pair together in the presence of a weak attractive potential. In most metallic superconductors, a second-order interaction between the phonons and electrons creates a weak attractive potential that overcomes the screened electronic Columbic repulsion between the electrons. The energetically favorable paring leads to lower overall energy by Δ compared to the Fermi surface made of unpaired electrons. The paired electrons are defined as Cooper pairs. The net spin of a Cooper pair is zero, as electrons with opposite spin cancel, therefore Cooper pairs follow Bose-Einstein statistics. They condense into a ground state with macroscopic coherence with one wavefunction $|\Delta|e^{i\phi}$ leading to the existence of zero DC resistance in the material. Coherence length determines the length of this phase coherence and hence the size of the Cooper pairs. The coherence length is given as $\xi_0 = \frac{\hbar v_F}{\pi \Delta_0}$ with $v_f$ being the Fermi velocity[44]. The lowering of energy due to pairing also leads to opening the energy gap (Δ) between the superconducting ground state and the continuum of excited states.

These excited states are called quasiparticles. These quasiparticles are the superposition of the normal metal electron and hole states, but for the energies far above the Fermi level (compared to Δ), quasiparticles are primarily electron/hole-like. Fermi-Dirac statistics describe the quasiparticle distribution. More generally, electron conservation requires that excitations always be created or destroyed in pairs; hence the spectroscopic gap is 2Δ, not Δ.[45]

### 2.1.1 Superconducting Energy gap

The energy gap (Δ) of the superconductor is temperature dependent and depends on the quasiparticle distribution, and is determined by the self-consistency equation given as

$$\frac{1}{\mathrm{N}(0)V_{sc}} = \int_{\Delta(T)}^{k_B T_D} \frac{(1-2f(E,T))}{\sqrt{E^2-\left(\Delta(T)\right)^2}}\mathrm{dE} \tag{2.1}$$

where $\mathrm{N}(0)$ is the single spin density of states, $V_{sc}$ is the attractive potential. The critical temperature ($T_c$) is defined as the temperature where the gap goes to zero, $\Delta(T_c) = 0$. Fig. 2.1 shows the universal normalized temperature dependence of the bandgap with the normalized temperature. At 0K, quasiparticles density goes to zero, and the energy gap for a weak-coupling superconductor in terms of $T_c$ is defined as

$$\Delta_o = \Delta(0) \sim 1.764\, k_B T_C \tag{2.2}$$

where $k_B$ is the Boltzmann constant. Fig. 2.1 shows the temperature dependence of the bandgap. There is no exact analytical function describing this temperature dependence of the bandgap. The relation $\Delta(T) = \Delta_o \exp\left(-\sqrt{\frac{2\pi k_b T}{\Delta_o}}\, e^{-\frac{\Delta_o}{k_B T}}\right)$ follows the low-

temperature dependence pretty well but fails near $T_C$. The relation $\Delta(T) = \Delta_o \tanh\left(1.74\sqrt{\left(\frac{T_C}{T} - 1\right)}\right)$ follows high and low temperatures very well but deviates in the intermediate temperature. Both the approximations are valid for temperatures $\frac{T}{T_c} < 0.3$. I have used $\Delta(T) = \Delta_o \tanh\left(1.74\sqrt{\left(\frac{T_C}{T} - 1\right)}\right)$ in my calculation.

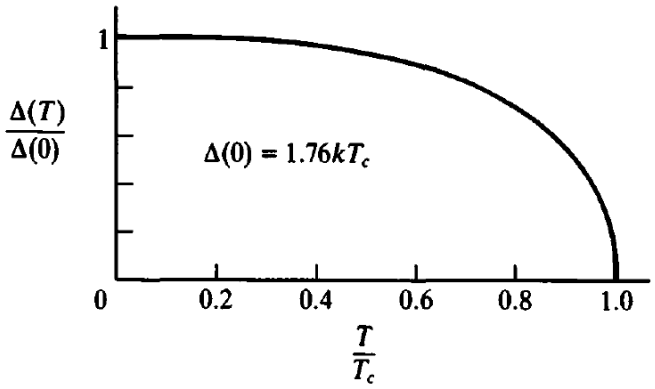


*Fig. 2.1: The normalized temperature dependent superconducting bandgap as a function of normalized temperature*[45]

### 2.1.2 Quasiparticle number density

The presence of a bandgap leads to the increase in the energy of quasiparticle ($E_k$) compared to its normal state equivalent ($\xi_k$). A quasiparticle with momentum k has the energy $E_k = \left(\xi_k^2 + \Delta^2\right)^{\frac{1}{2}}$. Hence there are no quasiparticle states within the bandgap. Above the gap, it has a divergent density of states dependent on the bandgap of the superconductor. The density of states of the quasiparticle is given by

$$\frac{N_s(E)}{N(E_F)} = \rho(E) = \begin{cases} \frac{E}{\sqrt{E^2 - \Delta^2}}, & E > \Delta \\ 0, & E < \Delta \end{cases} \tag{2.3}$$

where $N(E_F)$ is the normal state single-spin density of states at the fermi level. Fig. 2.2 shows the schematic energy diagram for a superconductor.

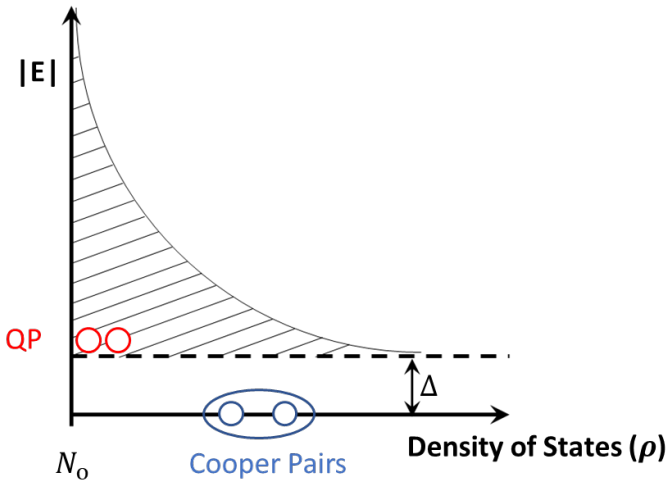


*Fig. 2.2 Schematic energy diagram of a superconductor showing Cooper pair band and Quasiparticle (QP) band.*

Using the quasiparticle density of states and Fermi-Dirac distribution, the total quasiparticle number density is defined as

$$n_{qp}(T) = 4N(0)\int_{\Delta}^{\infty} f(E,T)\rho(E,T)dE\,. \tag{2.4}$$

which is expanded as

$$n_{qp}(T) = 4N(0)\int_{\Delta}^{\infty} \frac{1}{\exp\left(\frac{E}{k_B T}\right)+1} \times \frac{E}{\sqrt{E^2-\Delta(T)^2}}dE \tag{2.5}$$

A factor of 2 comes from excitations above and below the bandgap, and an additional factor of 2 is from spin. For low temperatures, the quasiparticle density can be approximated as[46]

$$n_{qp}(T) = 2N(0)\sqrt{2\pi k_b T\Delta(T)}\exp\left(-\frac{\Delta(T)}{k_B T}\right) \tag{2.6}$$

On the other hand, the number density of the Cooper pairs is the function of the energy gap of its superconducting state and is given as follows[47].

$$n_{cp}(T) = 2N(0)\Delta(T) \tag{2.7}$$

Fig. 2.3 shows the variation of quasiparticle and Cooper pair density as a function of normalized temperature. For the temperature ($T/T_C < 0.2$), the quasiparticle number density is at least six orders smaller greater than the cooper pair density and hence is negligible compared to that of Cooper pair density.

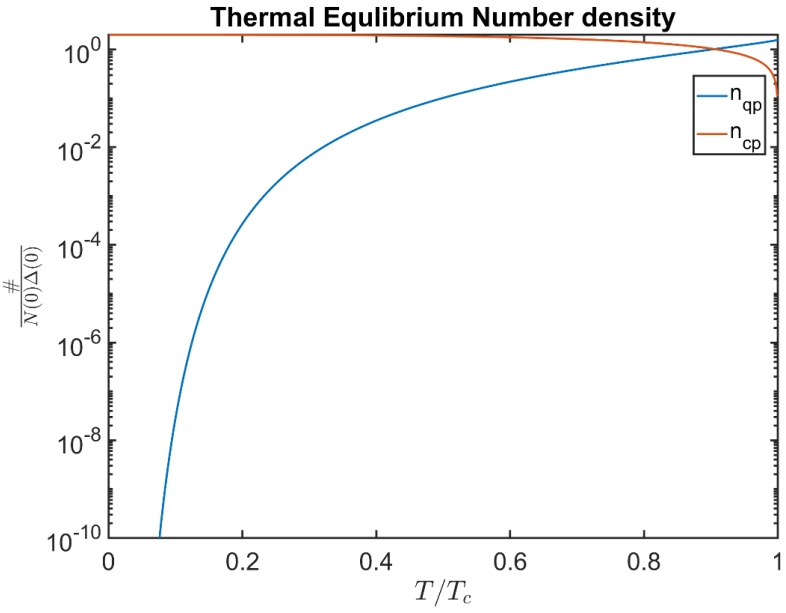


*Fig. 2.3: The normalized Cooper pair and quasiparticle density variation with normalized temperature.*

## *2.2 Quasiparticle dynamics*

Quasiparticle excitations have a finite lifetime. Two quasiparticles with opposite spin and momentum having energies $E$ and $E'$ combine to form a Cooper pair with the emission of a phonon with energy $\Omega = E + E' > 2\Delta$ and vice versa, phonons

with energy $> 2\Delta$ break a Cooper pair to generate quasiparticles. Hence phonons with energy $\Omega > 2\Delta$ play an essential role in the quasiparticle dynamics, and the phonon density is also included in rate equations.

### 2.2.1 Quasiparticle Recombination

The recombination process is a two-body process, for which the recombination rate is defined as

$$\frac{\mathrm{dn}}{\mathrm{dt}} = = R_{qp} n_{qp}^2 \tag{2.8}$$

where $n_{qp}$ is the quasiparticle number density, and $R_{qp}$ is the recombination constant. In thermal equilibrium, using $\frac{dn}{dt} = -n_{qp}/\tau_r$Kaplan[48] calculated the quasiparticle lifetime for quasiparticles at the gap edge to be

$$\frac{1}{\tau_{\mathrm{R}}} = \frac{\sqrt{\pi}}{\tau_o}\left(\frac{2\Delta}{k_b T_C}\right)^{\frac{5}{2}}\left(\frac{T}{T_c}\right)^{\frac{1}{2}} \exp\left(-\frac{\Delta}{k_b T}\right) = \frac{\tau_0}{n_{qp}}\frac{N(0)(k_B T_C)^3}{2\Delta^2}, \tag{2.9}$$

where $\tau_o$ is a material-specific time constant describing the electron-phonon coupling strength. The quasiparticle lifetime is inversely proportional to the quasiparticle number density, $n_{qp}$. Using the recombination lifetime, the recombination constant can be defined as $R_{qp} = \frac{1}{n_{qp}\tau_R}$ which can be rewritten as

$$R_{qp} = \left(\frac{2}{\tau_0}\right)\left(\frac{1}{N(0)\Delta(\mathrm{T})}\right)\left(\frac{\Delta(\mathrm{T})}{k_B T_C}\right)^3. \tag{2.10}$$

As per definition, $R_{qp}$ is independent of the quasiparticle density, and it is relatively constant as long as the gap energy, $\Delta$, doesn't change significantly. The relation also

holds even for non-equilibrium quasiparticle distributions[49]. Since $\tau_0$ is proportional to $\Delta^{-3}$[50], $R_{qp}$ is proportional to $\Delta^2$.

### 2.2.2 Pair Breaking

The phonons with energy $\Omega > 2\Delta$ can either break a Cooper pair to generate two quasiparticles or escape from the superconducting film into the underlying substrate. In thermal equilibrium, phonons generated by the recombing quasiparticles maintain equilibrium by breaking the Cooper pairs (generating quasiparticles) at equal rates. The pair breaking rate is also a material-specific parameter. Kaplan[48] formulates the pair breaking rate at energy $\Omega = 2\Delta$ as

$$\tau_B^{-1}(2\Delta(T)) = \frac{1}{\tau_0^{ph}} \frac{\Delta(T)}{\Delta(0)} \Big(1 - 2f\big(\Delta(T)\big)\Big) \tag{2.11}$$

where $\tau_0^{ph} = \frac{\hbar N}{4\pi^2 N(0)} \langle \alpha^2 \rangle_{av} \Delta(0)$ is a characteristic time constant with N and N (0) are the ion number density and single state spin number density, and $\langle \alpha^2 \rangle_{av}$ is the electron-phonon coupling function. For phonons with energy $2\Delta$, the breaking rate ~ $1/\tau_0^{ph}$. For temperatures, $\frac{T}{T_c} < 0.3$, the pair breaking rate is constant with respect to temperature for different values of $\Omega$[48].

### 2.2.3 Phonon Escape term

The phonon escape from the superconducting film to the substrate is described by an energy-independent escape time constant ($\tau_{esc}$). It depends on the thickness of the superconductor $d$, transmission probability $\eta$ and the speed of sound in the superconductor, $s$ and is given by

$$\tau_{esc} \approx \frac{4d}{\eta s}. \tag{2.12}$$

For a superconducting thin film (labeled with the subscript 1) on a substrate (labeled with the subscript 2), the transmission probability of phonons is a function of the ratio of the speed of sound $(s_2/s_1)$ and the ratio of the mass densities $(\rho_2/\rho_1)$. This probability is calculated from contour plots of $(s_2/s_1)$ and $(\rho_2/\rho_1)$ are presented in[51] and calculated for aluminum and titanium nitride on silicon.

### 2.2.4 Quasiparticle trapping rate

Quasiparticles can get trapped in the sub-bandgap density of states present in the superconductor. These defects can be vortices or normal metal islands. With the presence of many unoccupied states below the band edge at low temperature, excess quasiparticles can decay into sub-gap states. The inelastic process is led by electron-phonon or electron-electron interaction in the defects. The rate process of the quasiparticle trapping can be defined as

$$\frac{\mathrm{dn_{qp}}}{dt} = -\frac{n_{qp}}{\tau_{Trap}} \tag{2.13}$$

For relatively lower quasiparticle density $\frac{n_{qp}}{n_{cp}} < 10^{-4}$, trapping is a dominant mechanism compared to recombination for the case of non-equilibrium quasiparticles. [32], [39]. The trapping rate can be defined as $s = 1/\tau_{Trap}$. Fig. 2.4 shows the schematic of quasiparticle recombination, generation, trapping, and phonon escape into phonon bath.

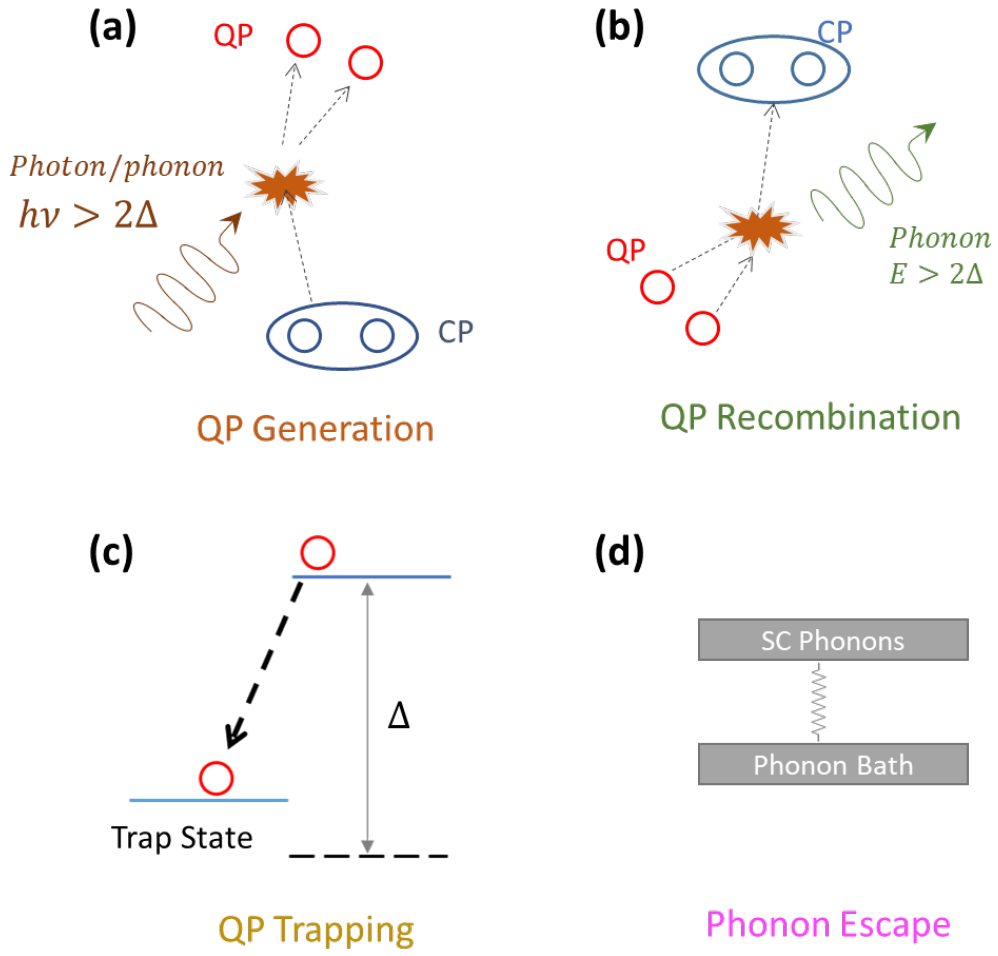


*Fig. 2.4: (a) QP generation by breaking of cooper pairs and (b)recombination of two QP (c) QP trapping by falling in a trap state (d) Escape of phonons into substrate*

## *2.3 Electrodynamics in superconductors:*

The electromagnetic field is expelled from the core of the superconductor. This phenomenon is known as the Meissner effect. The field inside the superconductor is blocked due to the surface currents. The relation between the screening currents under an electromagnetic field is defined by two phenomenological equations proposed by the London brothers[52].

$$\mathbf{j} = -\frac{\mathrm{n_s e^2}}{\mathrm{m}}\mathbf{A} \tag{2.14}$$

$$\frac{\mathrm{d}\mathbf{j}}{\mathrm{dt}} = \frac{\mathrm{n_s e^2}}{\mathrm{m}}\mathbf{E} \tag{2.15}$$

where $\boldsymbol{j}$ is the current density, $\boldsymbol{A}$ is the magnetic vector potential, $\boldsymbol{E}$ is the electric field, $n_s$ is the phenomenological superconducting electrons (Cooper pair) density, $e$ and $m$ are the electron charge and mass, respectively. Solving Eq. (2.14) gives rise to the characteristic London penetration length $\lambda_L(0) = \sqrt{\frac{m}{\mu_o n_s e^2}}$ where $\mu_0$ is permeability of vacuum. The EM field penetrates the superconductor by the characteristic length $\lambda_L$. Eq. (2.3) indicates that superconducting electrons would keep on accelerating. Solving it for finite frequency leads to an inductive response $\sigma_2 = -j\, n_s e^2/m\omega$ by the superconducting electrons. It leads to the presence of additional inductance by the superconductor called kinetic inductance.

Due to the finite response of Cooper pairs to the EM field, quasi-particles also contribute the conductivity leading to finite dissipation under high-frequency operation in superconductors. Phenomenologically, the high-frequency conductivity can be explained by a two-fluid model with Cooper pairs providing an inductive loss channel and the quasiparticles being dissipative provide an ohmic channel. Using the Drude model, the real part of the conductivity is given by $\sigma_1 = n_n e^2 \tau/m$, with $n_n$ the normal electron density and $\tau$ the elastic scattering time. The imaginary (inductive) part is described as above. While for a more accurate microscopic view, using Mattis-Bardeen theory, the complex conductivity $\sigma = \sigma_1 - j\sigma_2$ at the angular frequency, $\omega$ is given as[53], [54]

$$\frac{\boldsymbol{\sigma_1(\omega,T)}}{\boldsymbol{\sigma_n}} = \frac{2}{\hbar\omega}\int_{\Delta(T)}^{\infty}[f(E,T) - f(E+\hbar\omega,T)]g_1(E,T)\ dE$$
$$+\frac{1}{\hbar\omega}\int_{\min(\Delta(T)-\hbar\omega,-\Delta(T))}^{-\Delta(T)}[1-2f(E+\hbar\omega,T)]g_1(E,T)\ dE \quad (2.16)$$

$$\frac{\boldsymbol{\sigma_2(\omega,T)}}{\boldsymbol{\sigma_n}} = \frac{1}{\hbar\omega}\int_{\Delta(T)-\hbar\omega}^{\Delta(T)}[1-2f(E+\hbar\omega,T)]g_2(E,T)\ dE \quad (2.17)$$

Where $g_i(E,T)$, the product of the coherence factor and quasiparticle density of states is described as follows.

$$g_1(E,T) = \frac{(E(E+\hbar\omega)+\Delta(T)^2)}{\sqrt{E^2-\Delta(T)^2}\sqrt{(E+\hbar\omega)^2-\Delta(T)^2}} \quad (2.18)$$

$$g_2(E,T) = \frac{(E(E+\hbar\omega)+\Delta(T)^2)}{\sqrt{\Delta(T)^2-E^2}\sqrt{(E+\hbar\omega)^2-\Delta(T)^2}} \quad (2.19)$$

Here $\sigma_N$ is the normal state conductivity just before the transition. The first integral in $\sigma_1$ describes the conductivity due to the transition of quasiparticle after the absorption of the photon of energy $\hbar\omega$. It is proportional to the number of occupied states in E and unoccupied states at $(E+\hbar\omega)$. The second integral in the $\sigma_1/\sigma_n$ describes the pair breaking of Cooper pairs by the photons having energy greater than the superconducting bandgap ($\hbar\omega > 2\Delta$). For a microwave photon, the contribution from this term is zero as its energy is far below the superconducting bandgap and cannot break any Cooper pairs, so is neglected in further calculations.

The conductivity of the Cooper pairs and the quasiparticles also follow the same trend corresponding to their number density[45].

The Eqs. (2.16) and (2.17) can only be solved numerically. For the case $k_BT \ll \Delta$ and $\hbar\omega \ll \Delta$ , the analytic solution exists and is given as [55]

$$\frac{\sigma_1}{\sigma_n} = \frac{4\Delta_0}{\hbar\omega} e^{-\frac{\Delta_0}{k_B T}} \sinh\left(\frac{\hbar\omega}{2k_B T}\right) K_o\left(\frac{\hbar\omega}{2k_B T}\right) \tag{2.20}$$

$$\frac{\sigma_2}{\sigma_n} = \frac{\pi\Delta_0}{\hbar\omega}\left[1 - \sqrt{\frac{2\pi k_B T}{\Delta_0}} e^{-\frac{\Delta_0}{k_B T}} - 2e^{-\frac{\Delta_0}{k_B T}} e^{-\frac{\hbar\omega}{2k_B T}} I_o\left(\frac{\hbar\omega}{2k_B T}\right)\right] \tag{2.21}$$

where $I_o$ and $K_o$ is the modified Bessel function of first and second-order, respectively. Fig. 2.5 and Fig. 2.6 show the variation of the real and imaginary parts of the conductivity using numeric calculation and analytical expression. The analytical solution follows the numeric one throughout the temperature range but underestimates the quasiparticle density at higher temperatures.

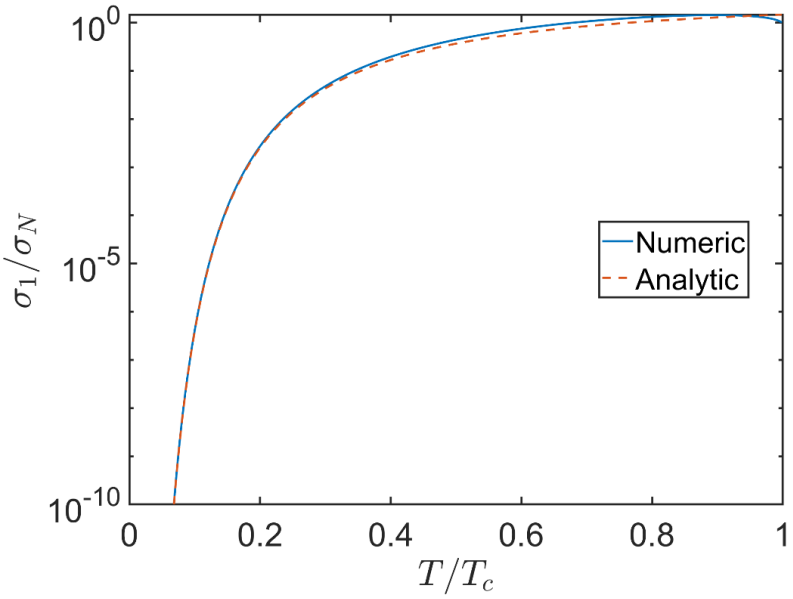


*Fig. 2.5: Temperature variation of the real part of the conductivity ($\sigma_1/\sigma_n$) for $T_c$ =1.2 K and f = 5 GHz for both the analytical approximation and numerical solution.*

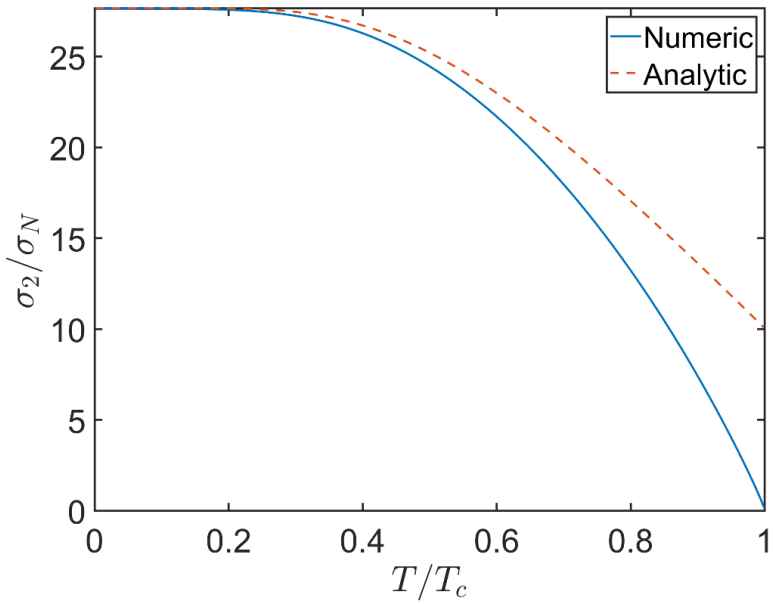


*Fig. 2.6 Temperature variation of the inductive portion of the conductivity ($\sigma_2/\sigma_n$) for $T_c$ =1.2 K and f = 5 GHz for both the analytical approximation and numerical solution.*

### 2.3.1 Surface Impedance of superconductors

The propagation properties of the resonator depend on the surface impedance, which relates the circuit parameters to the conductivity relations. The surface impedance of a conductor is determined by the ratio of the transverse components of the magnetic and electric field on the surface of the metal.

$$Z_s = \frac{E_x}{H_y}|_{z=0} \tag{2.22}$$

The surface impedance of the superconductor depends on the thickness of the film, d, coherence length, $\xi_o$, mean free path, $l$, and penetration depth, $\lambda$ of the superconductor[46]. Table 2-1 summarizes the conventional relationships between surface impedance and conductivity for various conditions.

*Table 2-1: Surface impedance of a superconductor in various limits*

| Name | Condition | Surface impedance |
|---|---|---|
| Thin-film limit | $l \approx d$<br>$l \ll \lambda$ and $l \ll \xi_o$ | $Z_s = \frac{1}{(\sigma_1 - j\sigma_2)d}$ |
| Thick film, local (dirty) limit | $l \ll \lambda$ and $l \ll \xi_o$ | $Z_s = \sqrt{\frac{j\mu_o\omega}{\sigma_1 - j\sigma_2}}$ |
| Thick film, Extreme anomalous limit | $\xi_o \gg \lambda$ and $l \gg \lambda$ | $Z_s = \frac{j\sqrt{3}\mu_o\omega}{2}\left[\frac{3\pi\omega}{4v_o\lambda^2}\frac{\sigma_1 + j\sigma_2}{\sigma_n}\right]^{-\frac{1}{3}}$ |

## 2.4 *Resonator Theory*

In this study, superconducting resonators are designed using coplanar waveguides. Its planar nature and ease in fabrication make it attractive in cQED. A coplanar waveguide (CPW) consists of a central conductor strip surrounded by two ground planes located on both sides of the central strip that are all placed on the top of the dielectric substrate, as shown in Fig. 2.7.

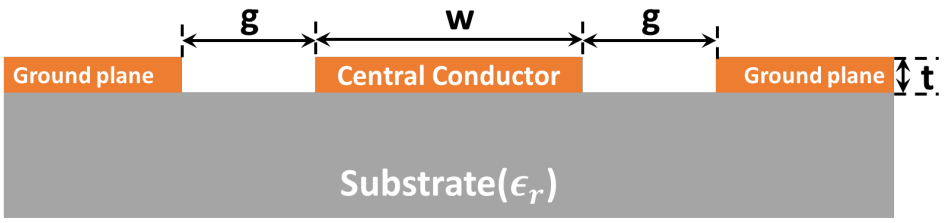


*Fig. 2.7: Schematic of a coplanar waveguide*

Due to the inhomogeneity of the dielectrics surrounding the conductors (substrate on underneath and vacuum above), CPWs support a quasi-TEM mode as its fundamental mode with a non-zero electric and magnetic field component along the direction of electromagnetic wave propagation. However, the non-TEM electric and

magnetic field components are small compared to the TEM fields[56]. Additionally, the presence of three conductors leads to both odd and even modes of TEM propagation. In the even mode, the electric field originates from the central conductor and terminates on the ground planes, while in the odd mode, the electric field originates from one of the ground planes and terminates on the other ground plane. The ground planes of the waveguide are shorted to ensure only the low dispersive even mode is supported. The characteristic capacitance and geometric inductance of the CPW can be analytically estimated using a conformal mapping technique. Using the first-order approximation for a zero-thickness film, the capacitance per unit length is given by [57]

$$C = \epsilon_{eff}\epsilon_o 4\frac{K(k)}{K(k')} \tag{2.23}$$

where $k = w/(w + 2g)$ with w is the width of the central conductor and g is the gap between the central conductor and ground plane. K(k) is the elliptical integral of the first kind, k′is defined as $k' = \sqrt{1 - k^2}$ and $\epsilon_{eff}$ is the effective dielectric constant of waveguide defined as $(1 + \epsilon_r/2)$ where $\epsilon_r$ is the relative dielectric constant of the substrate. Similarly, the inductance per unit length is given by [57]

$$L_g = \mu_o \frac{K(k')}{4K(k)} \tag{2.24}$$

The material's superconductivity also adds to the total inductance (defined as kinetic inductance) of the resonator, which depends on several parameters, including film microstructure, composition, and thickness[45]. However, the contribution of the kinetic inductance is often tiny compared to the geometric inductance. Therefore, the characteristic impedance of the waveguide is given as

$$Z_o = \sqrt{\frac{L}{C}} \approx \frac{30\pi}{\sqrt{\epsilon_{eff}}} \frac{K(k')}{K(k)}, \tag{2.25}$$

which depends only on the ratio of the central conductor width to the gap. Hence the characteristic impedance of the waveguide is independent of the dimensions of the conductors. For silicon or sapphire as substrate with dielectric constant, $\epsilon = 11.7$ and 11.5 respectively and $w/g = 0.5 \Rightarrow k = 0.5$, one finds $Z_o \sim 50\Omega$, which allows to match to 50 Ω cable impedance for maximum power transfer.Additionally, the electric fields present are calculated using a conformal mapping technique. For a zero thickness film, perfectly conducting film one finds[58]

$$E_y(z=0,x)_{air} = \frac{\frac{K(k)}{K(k')}}{\sqrt{[x^2-a^2][x^2-b^2]}} \text{ for } x < a \text{ or } x > b, \tag{2.26}$$

where a = w/2 and b = w/2 +g is the half of the distance between ground planes. The electric field is plotted in Fig. 2.8.

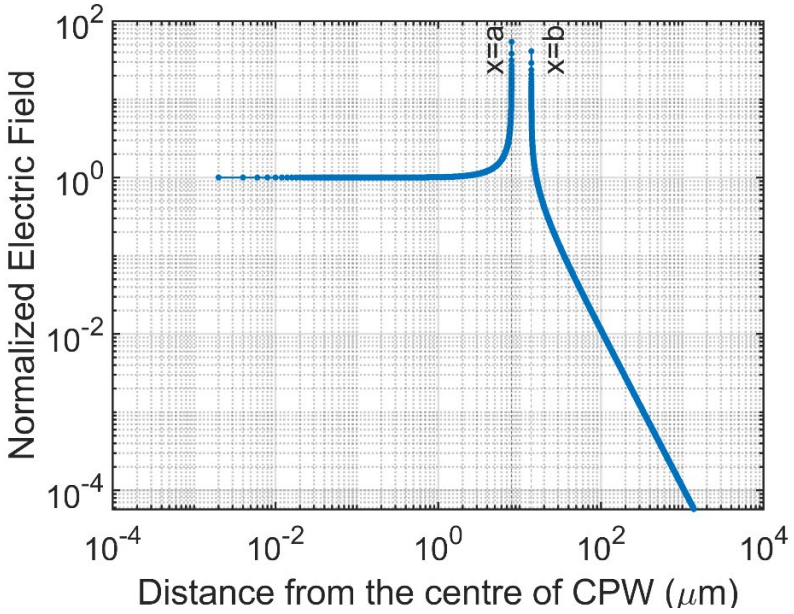


*Fig. 2.8: Normalized Electric field of the coplanar waveguide with a=16 and b = 32 and $z = 0$*

For my research, I designed quarter wavelength ($\lambda_o/4$) resonators from the CPW transmission line. According to the transmission line theory, the input impedance of a shorted quarter wavelength transmission line is given as

$$Z_{in} = Z_o \tanh(\alpha + j\beta l) \ = \mathrm{Z_o}\frac{1 - \mathrm{j}\tanh\alpha l \ \cot\beta l}{\tanh\alpha l - j\cot\beta l} \tag{2.27}$$

Where $\gamma = \ \alpha_p + j\beta_p = \sqrt{(R + j\omega L\,)(j\omega C)}$ is a complex propagation constant. For low-loss case ($R \ll \omega L$),

$$\alpha_p + j\beta_p = \frac{1}{2}R\sqrt{\frac{C}{L}} + j\omega\sqrt{LC}. \tag{2.28}$$

Here $R$ is the resistance per unit length due to the quasiparticles. Resonance at the fundamental frequency ($\omega = \omega_0$), $\beta_p l = \frac{2\pi}{\lambda_0} \times \frac{\lambda_0}{4} = \frac{\pi}{2}$ and the angular resonant frequency is given as

$$\omega_0 = \frac{\pi}{4l\sqrt{LC}} \tag{2.29}$$

Also, as the resonator reaches resonant frequency, $Z_{in}$ increases and for a lossless case $Z_{in} \to \infty$. This behavior is similar to the behavior of the parallel RLC circuit with resistance $\tilde{R}, \tilde{L}$ and $\tilde{C}$.

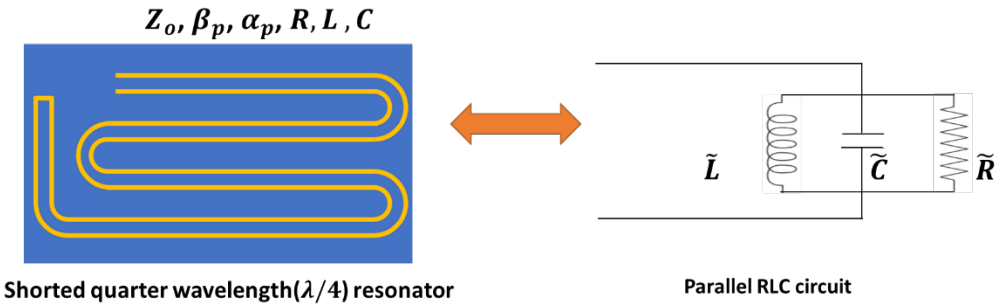


*Fig. 2.9: Equivalence of the fundamental mode of a quarter-wave resonator and a parallel RLC circuit*

The resonant frequency of the parallel RLC resonator is defined as $\omega_o = \frac{1}{\sqrt{\tilde{L}\tilde{C}}}$ and the quality factor as $Q = \omega_o \tilde{R}\tilde{C}$ [59]. The input impedance near resonance $\omega = \omega_0 + \Delta\omega$ is given as

$$Z_{in} \cong \frac{1}{\frac{1}{\tilde{R}} + 2j\Delta\omega\tilde{C}} \tag{2.30}$$

Now comparing it with the resonant frequency quarter-wave resonator for a small loss case ($\alpha l \ll 1$) and frequency close to the resonant frequency, $\beta_p l = \frac{\pi}{2} + \frac{\Delta\omega}{\omega_o}$ and $Z_{in}$ can be approximated as

$$Z_{in} \cong \mathrm{Z_o} \frac{1}{\alpha_p l - j\frac{\pi}{2}\frac{\Delta\omega}{\omega_0}} \tag{2.31}$$

Comparing Eq. (2.30) and (2.31) gives $\tilde{R} = \frac{2}{l}\frac{L}{RC}$ , $\tilde{C} = C\frac{l}{2}$ and $\tilde{L} = \frac{8l}{\pi^2}L$ which one put back in the relation for quality factor gives

$$\frac{1}{Q_i} = \frac{1}{\omega_o}\frac{R}{L} \tag{2.32}$$

In the superconducting resonator, the net inductance includes the contribution from both geometric($L_g$) and the kinetic inductance ($L_s$)into the relation and is given as the $L = L_s + L_g$. Hence the net quality factor can be rewritten as

$$\frac{1}{Q_i} = \frac{1}{\omega_o}\frac{R}{L_g + L_s} = \frac{1}{\omega_o}\alpha_{ki}\frac{R}{L_s} \tag{2.33}$$

Where $\alpha$ is the kinetic inductance defined as $\alpha_{ki} = \frac{L_s}{L_g + L_s} \sim \frac{L_s}{L_g}$. The contribution of the kinetic inductance and resistance towards the resonator gets modified by the waveguide geometry and is given as[22], [31]

$$\mathrm{R} = \left(\frac{\mathrm{g_{geom}}}{\mathrm{w}}\right)\Re(\mathrm{Z_s}) \tag{2.34}$$

$$L_s = \left(\frac{\mathrm{g_{geom}}}{w}\right)\Im(Z_s/\omega) \tag{2.35}$$

Where $\mathrm{g_{geom}}$ is defined as[60]

$$\mathrm{g_{geom}} = \mathrm{g_{ctr}} + \mathrm{g}_{gnd}$$

$$\mathrm{g_{ctr}} = \frac{1}{4K^2(k)(1-k^2)}\left[\pi + \log\left(\frac{4\pi a}{t}\right) - k\log\frac{1+k}{1-k}\right] \tag{2.36}$$

$$\mathrm{g}_{gnd} = \frac{k}{4K^2(k)(1-k^2)}\left[\pi + \log\left(\frac{4\pi a}{t}\right) - k\log\frac{1+k}{1-k}\right]$$

Here a is half the width of the center conductor ($a = \frac{w}{2}$) and b is half the distance between the left and right ground planes $\left(b = \frac{w+2g}{2}\right)$. $\mathrm{g_{ctr}}$ is the contribution from the central conductor plane while $\mathrm{g}_{gnd}$ is from the ground plane. Now, substituting Eq. (2.34)-(2.36) in (2.33) and using the values of inductance from Table 2-1 for thin-film limit.

$$\frac{1}{Q_i} = \frac{L_s}{L_g}\frac{\sigma_1}{\sigma_2} \tag{2.37}$$

Where $L_s = \frac{1}{\omega_o}\left(\frac{g_{geom}}{w}\right)\left(\frac{1}{d\sigma_N}\right)\left(\frac{1}{\sigma_2/\sigma_N}\right)$

## *2.5 Loss mechanisms in microwave resonators*

Even though the thermal quasiparticles do not limit the quality factor, other energy loss mechanisms hamper the resonator performance[61]. These mechanisms depend on the various material properties such as the choice of the superconductor and substrate, growth techniques of the superconductors, the geometry of the waveguide, and the various fabrication processes. Some of the primary sources of energy losses are

two-level systems (TLS) present in the dielectrics, dissipation by athermal quasiparticles, electromagnetic radiation losses through the transmission lines, the losses through the vortices present in the superconductor, and trapped flux. Hence the total internal quality factor can be summarized as

$$\frac{1}{Q_I} = \frac{1}{Q_{TLS}} + \frac{1}{Q_{QP}} + \frac{1}{Q_{rad}} + \frac{1}{Q_{vortices}} + \cdots \tag{2.38}$$

Imperfections in the material act like two-level systems that interact with the electric field of the incoming microwave signals, leading to losses especially at a low input signal power regime. The quality factor also decreases due to quasiparticles which provide a resistive path. These have a significant impact at a higher temperature range of the operating regime of the resonators. The design of the resonators can also affect the participation of the TLSs. With the increase in the central conductor width ($w$) and gap (g) between the central conductor and the ground plane, the electric field spreads out in the air and the substrate for a given input voltage. It causes the electric field concentration in the dielectrics to be reduced, which reduces the losses through TLSs. Therefore, CPW with a smaller central conductor size is explored to study TLSs in the CPW fabrication.[61]

### 2.5.1 Losses from Two Level System defects

At low temperatures, lack of crystalline order in amorphous solids leads to deviation of acoustic, thermal, and dielectric properties compared to its crystalline form[62]. These deviations have a universal nature and can be modeled as a broad spectrum of random two-level systems with an asymmetric double-well potential separated by a barrier introduced by Phillips[63]. An ion or electron residing between

two spatial quantum states can hop between the two states via tunneling or thermal activation. The microscopic origins of these TLSs are not known. Often these defects are associated with tunneling atoms, trapped charges, dangling bonds, or the presence of polar impurities such as $OH^-$ [62], [64]. Fig. 2.10: shows a schematic of TLS with energy offset between the wells as $\epsilon$ and tunneling amplitude $\Delta_o$. The corresponding TLS energy is defined as $\Delta_{TLS} = \sqrt{\epsilon^2 + \Delta_0^2}$[65], [66].

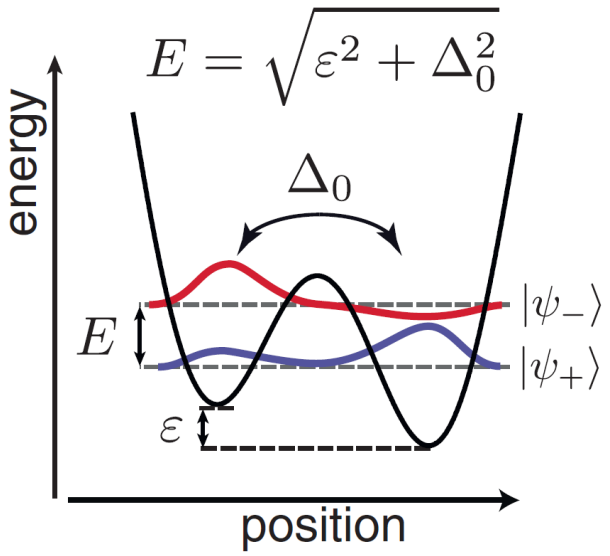


*Fig. 2.10: Generic model for a two-level system in an amorphous solid*[62]

Some defects have dipole moments due to the presence of charge in them. Although the TLSs have a broad distribution of energy splitting [63], TLSs with energy splitting close to the resonance frequency of resonators ($\Delta_{TLS} \sim hf_o$) are the primary loss sources. TLS are characterized by a finite lifetime and a relaxation rate. The relaxation rate determines the maximum rate at which energy can leak from the resonator through TLS[62]. The level population and the relaxation rates of these TLSs are very much dependent on the temperature and electric field. Due to lack of sufficient energy, at low temperatures ( $\Delta_{TLS} > k_B T$ ), the TLSs are in the ground state. In this scenario, for low

resonator electric field, the resonant TLSs couple with the resonant field and dissipate the energy via phonon relaxation to the external bath, leading to higher resonator loss resulting lower quality factor[11], [62], [67]. On the other hand, saturated TLSs have a reduced energy exchange between the resonator and the TLSs, and the resonator quality factor remains unaffected. Saturation of TLS happens due to increased thermal energy of the environment at higher temperatures. Higher electric fields also cause a faster precession of TLS compared to its relaxation rates leading to population saturation[68]. The impact of TLS on loss and resonant frequency shift is obtained from the variation in the complex dielectric function due to the TLSs in the microwave field[46], [68]. The variation in the imaginary part of the dielectric function describes the internal loss. A complete temperature and excitation power of the resonator dependent microwave loss by a single TLS in a uniform electric field is given as

$$\delta_{TLS} = F\delta_{TLS}^{0} \tanh\left(\frac{\hbar\omega}{2\mathrm{k_B T}}\right) \times \frac{1}{\sqrt{\left(1+\left(\frac{\langle \mathrm{E}\rangle}{\mathrm{E_s}}\right)^{2}\right)}} \tag{2.39}$$

Where $\delta_{TLS}^{0}$ is the intrinsic loss of the TLS, $\omega$ is the angular frequency. F is the filling factor of the dielectric containing TLSs. The term $\tanh(\hbar\omega/2\mathrm{k_B T})$ accounts for the thermal population difference between the two levels of TLS. A critical electric field determines the saturation of TLS by an electric field $\mathrm{E_s}$. It depends on the dipole moment of the TLS and its energy relaxation time ($\mathrm{T_1}$) and dephasing time ($\mathrm{T_2}$) of TLS and given as $E_S = \hbar/(p\sqrt{T_1 T_2})$ [68], [69]. $\langle \mathrm{E}\rangle$ is the rms electric field of the resonator. In the CPW resonators, there is an ensemble of TLSs present in the substrate or dielectrics present in any of the interfaces between metal, air, and substrate. Fig. 2.11

shows the simulated cross-sectional electric field of a coplanar waveguide. The electric field density is highest at the metal-substrate, substrate-air, and metal-air interface. The dielectrics present at these interfaces interact the most with the resonator electric field. These interfaces face the maximum fabrication steps and contain many TLSs due to leftover chemical residues or open bonds[70]. On the other hand, a high-quality substrate ensures a low loss number of TLSs[19], [70], [71]. The contribution from the TLSs present at the various interface is calculated in terms of participation ratios or fill factor $F_n$. The fill factor of the $i^{th}$ interface represents the fraction of total electric energy, $U_i/U_{tot}$ of the system stored in an interface and is defined as

$$F_i = \frac{U_i}{U_{tot}} = \frac{\int_{V_i} \epsilon_i |E|^2 ds}{\int_V \epsilon_i |E|^2 ds} \tag{2.40}$$

Here, $t_i$ is the thickness of the dielectric, $\epsilon_i$ is the dielectric constant, $V_i$ is the volume of the $i^{th}$ interface and V is the total volume of the resonator.

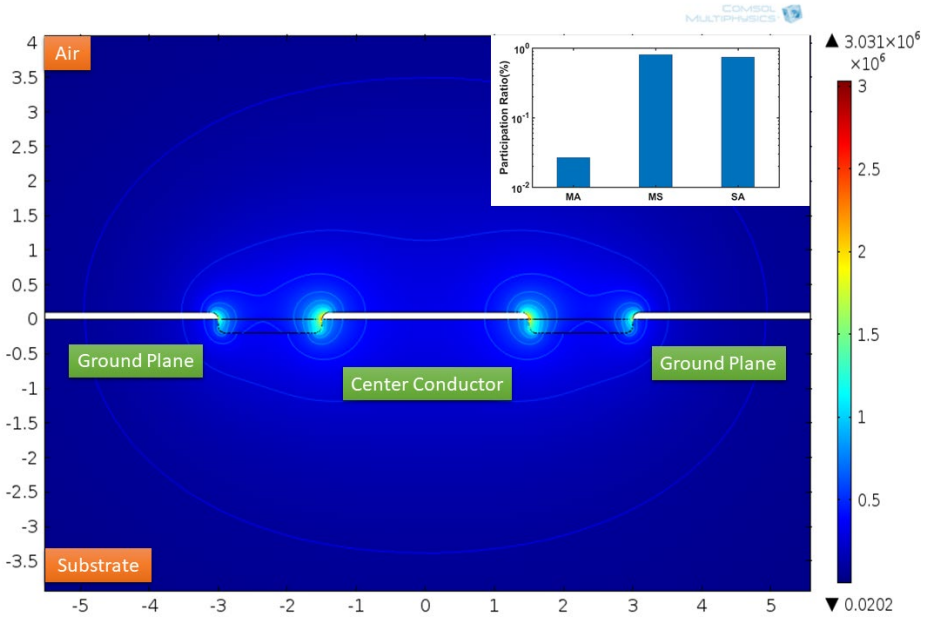


*Fig. 2.11: Electric field distribution in a CPW geometry. Inset shows the participation ratio of metal-air (MA), metal-substrate(MS), and substrate-air (SA) interface*

I performed finite element model (FEM) simulations with COMSOL to compare different interfaces indicate that the metal-substrate interface and substrate-air interface have an order of magnitude higher participation ratio than the metal-air interface, as shown in the inset of Fig. 2.11[72]. The overall TLS loss is now the sum of all the individual contributions from different TLS and is given as $\Sigma_i F_i \delta_{TLS}^i$. Hence the modified equation is given as

$$\frac{1}{Q_{TLS}} = \sum_i F_i \delta_{TLS}^i \frac{1}{\sqrt{1 + \left(\frac{\langle n \rangle}{n_C}\right)^{\alpha}}} \tanh\left(\frac{\hbar\omega}{2k_B T}\right) \tag{2.41}$$

The average electric field of the resonator is replaced by an easily measurable average photon (n) present in the resonator. The photon number is proportional to the power present in the resonator, which is proportional to the square of the resonator electric field. Hence the critical field is replaced by the critical photon number $n_c$ which defines the average saturation of the ensemble of TLSs. Due to various kinds TLSs with varying dielectric constant and loss tangents and CPW geometry, the exponent for the $n/n_c$ is no longer 1 but is replaced with a fit parameter $\alpha$.

The term $\alpha$ is challenging to define quantitively. As discussed earlier in the section, the original theoretically value from Philips[63] for one single TLS under a uniform electric field leads $\alpha$ equals 1. On other hand, CPWs have ensemble of different TLSs with different critical field and loss tangent at non-uniform electric field across the various vacuum, metal and substrate interfaces. Modelling of CPW with uniform dielectric layer with equal thickness across the interfaces lead to $\alpha$ equals 0.8 [73]. Experimentally $\alpha$ is a free fitting parameter, and reports have used $\alpha < 1$, but most

of them do not report it. The loss tangent and the low photon quality factor are the primary parameters that are reported quite often.

The standard nature of power dependency of TLS is shown in Fig. 2.12(a). For the power dependence at $n \ll n_c$, $\frac{1}{\sqrt{1+\left(\frac{n}{n_c}\right)^{\alpha}}} \rightarrow 1$ leading to the saturation of $Q_{TLS}$ to $Q_{TLS}^{0}$. While for $n \gg n_c$, $Q_{TLS}$ increases with power as $Q_{TLS} \propto \left(\frac{n}{n_c}\right)^{\frac{\alpha}{2}}$. The temperature dependence is shown in Fig. 2.12(b).

The saturation of TLS with increasing temperature leads to increasing $Q_{TLS}$ is determined by the term $\tanh\left(\frac{\hbar\omega}{2k_B T}\right)$ which is dependent only on the resonator frequency as $Q_{TLS} \propto 1/\tanh(\frac{\hbar\omega_{res}}{2k_B T})$. A transition temperature for a TLS loss for a given resonator can be defined as $T_{res} = \frac{\hbar\omega_{res}}{2k_B}$ . For temperatures $T \ll T_{res}$, $\tanh\left(\frac{\hbar\omega_{res}}{2k_B T}\right) \sim 1$ and $Q_{TLS}$ is temperature independent. While $T \gg T_{res}$, $\tanh\left(\frac{\hbar\omega_{res}}{2k_B T}\right) \sim \frac{\hbar\omega_{res}}{2k_B T}$ and hence $Q_{TLS}$ increases with temperature. At $T = T_{res}$, $\tanh\left(\frac{\hbar\omega_{res}}{2k_B T_{res}}\right) = \tanh(1) = 0.76$ which in turn means that at $T_{res}$, $Q_{TLS}$ increases by 30%. The resonators in the discussion have their resonant frequency ranging between 4-6 GHz, which corresponds to $T_{res}$ = 96 mK -144 mK.

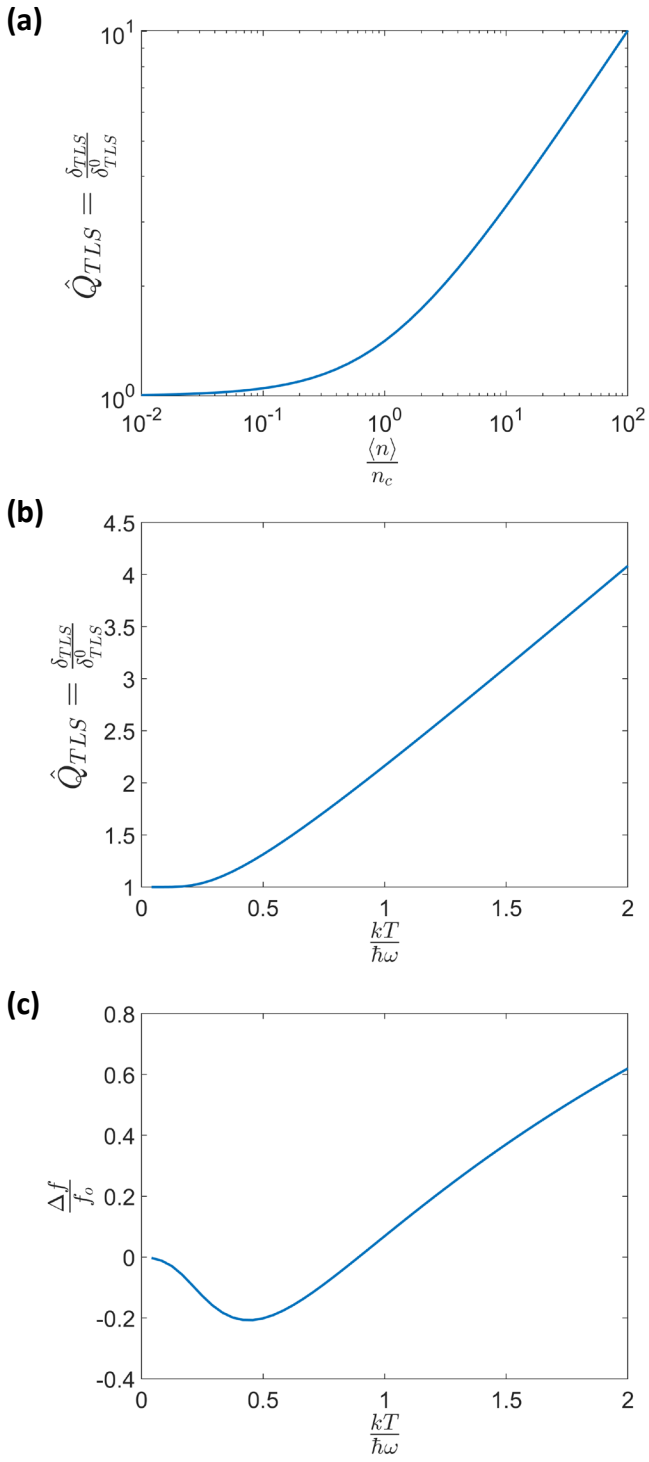


*Fig. 2.12: Theoretical TLS loss character with (a) power dependent (b) temperature. (c) shows the shift of the resonator frequency with temperature.*

The variation of the real part of the complex dielectric function due to TLS microwave interaction dictates the change in resonant frequency. Unlike microwave loss, where only resonant TLSs participate, non-resonant TLSs also contribute towards the frequency shift. Due to the broad spectrum of non-resonant TLS, not all the defects can simultaneously be saturated with a given electric field. This makes the frequency shift lesser dependent on the microwave field [68]. The frequency shift is given as follows

$$\frac{\Delta f}{f_o} = \frac{F\delta_{TLS}^0}{\pi}\left[\Re\left(\Psi\left(\frac{1}{2}+\frac{1}{2\pi i}\frac{\hbar\omega}{k_B T}\right)\right) - \log\frac{\hbar\omega}{k_B T}\right] \tag{2.42}$$

Here $f_o$ is the resonance frequency where there is no effect of TLS and $\Psi$ is a complex digamma function. Fig. 2.12(c) shows the change in frequency shift with temperature.

#### 2.5.1.1 Choice of superconducting material

The metal-substrate interface and dielectrics present at the metal vacuum interface depend highly on the choice of the superconductor. The metal vacuum interface with a lower participation ratio(as discussed in the previous section) can still contribute significantly towards loss due to lossy dielectrics present at that interface[20]. In circuit QED, aluminum is traditionally used as a superconductor due to its reasonable transition temperature and the availability of aluminum oxide as an excellent barrier needed for quantum elements like Josephson junction [12]. Until now, the highest reported single photon (low microwave power) quality factor for aluminum resonators is of the order of $10^6$ for MBE-grown crystalline aluminum on the sapphire substrate [16]. There is active research to find the alternative of aluminum as a superconductor. Elemental superconductors like niobium[74]–[76], tantalum [74], and

rhenium are also choice superconductors. Even though niobium and rhenium have a higher critical temperature, they suffer due to lossy metal substrate dielectrics leading to more significant losses[11], [61]. Low lossy dielectrics of nitride superconductors make them a better choice of materials. Titanium nitride (TiN) resonators have shown high-quality factors[77], [78]. A study comparing the various resonators made from different superconductors such as aluminum, rhenium, niobium, and TiN on either silicon or sapphire substrates reported that TiN could be used to make high-quality factor resonators [61].

Similarly, the TiN resonators explored in the 2D transmons qubits also show improved qubit performance [79]. The reasons for the improved performance of the TiN are not precisely known and are generally attributed to its better interface with the substrate. Some ternary nitride superconductors like niobium titanium nitride resonators also have shown high-quality resonators[80]. Additionally, varying composition leads to varying lattice parameters in the ternary superconductors, which offers an opportunity to produce no defect perfect metal substrate interface.

#### 2.5.1.2 Effect of processing steps

An important aspect associated with TLS loss is the impact of steps involved during the growth and processing of the resonators. Proper surface treatment of the substrate before deposition of metals reduces the TLS density and improves the thin film's crystalline quality. The silicon surface is treated with HF for silicon substrates to remove native oxide to reduce the TLS. Various groups have investigated the effect of different surface cleaning techniques on resonator performance. In one study, the

growth of aluminum on sapphire found that epitaxial aluminum has grown on oxygen plasma ($O_2^*$) treated and UHV annealed sapphire (0001) produced the highest quality factor Al resonators [16] while ion milling the sapphire substrate harmed the resonator performance. The surface treatment with oxygen plasma is believed to remove surface-bound hydroxyl molecules which act like TLS from the sapphire surface. In another case, hydrogen-terminated silicon substrates tend to have lower TLS loss compared to untreated Si [81]. As an example of processing impact, the lift-off patterning process led to higher contamination at the interface than using an etching process to pattern the resonators. Cleaning the post-lift-off process surface with low-energy oxygen plasma has also been shown to improve the quality factor of the resonators[19].

Similarly, for TiN resonators, the presence of a thin silicon nitride (SiN) layer between silicon and sputtered TiN led to the growth of (200) oriented TiN which led to the improved resonator performance [77]. Silicon nitride layers appear to have a lower TLS density compared to silicon dioxide. Another study observed that a fluorine-based ICP etch led to better performance than a chlorine-based etch for TiN based resonators[17]. In silicon substrates, native oxide grows within few hours of its removal from the surface. Hence just before loading the packaged sample, the treatment with HF has shown significant improvement, especially in TiN devices[82], [83].

The importance of various pre-deposition cleaning processes and processing steps in attaining high-quality factor resonators is clear from these previous studies. Therefore, special care is taken regarding the cleaning and processing steps to minimize TLSs from surfaces.

#### 2.5.1.3 Design constraints

The design of the resonators affects the participation ratio of the various dielectric present in the resonator. With the increase in the central conductor width ($w$) and gap (g) between the central conductor and the ground plane, the electric field spreads out in the air and the substrate for a given input voltage. It causes the electric field concentration in the dielectrics to be reduced, which reduces the losses through TLSs[61].

Another approach to making devices less sensitive to fabrication contamination is to over-etch the device creating trenches in the CPW gaps. Over-etching, the substrate-air region between the conductors, moves the TLS away from the highest electric field region. Over-etched resonators using TiN and NbTiN have shown improved resonator performance [18], [84]. Experimental studies have shown an improved resonator quality factor with an increase in the trench depth, with the effect saturated to a depth approximately one-tenth of the gap width [85].

To compare the impact of trench depth, I performed few simulations for CPWs having w/g = 2 using central conductor widths of 3, 5, and 10 $\mu m$ on the silicon substrate. Due to the better metal substrate quality in the MBE grown material, in this simulation, the metal substrate interface is ignored from the calculation. Since the coplanar waveguide supports a quasi-TEM mode, the field values are simulated using the electrostatics module of the COMSOL. The thickness of native oxide of both aluminum and silicon is estimated to be 1-2 nm [86], [87]. The dielectric constant for the metal oxides on the metal vacuum substrate is assigned 10 [72], while for the substrate vacuum interface, the dielectric constant of silicon oxide 3.9 is used. A typical

1-nm thick dielectric is used across the interfaces to ensure continuity of interfaces across the various region for the simulation, as shown in Fig. 2.13. The participation ratios are calculated as Eq. (2.40). Fig. 2.14 shows the simulation results for variation of the participation ratios with over-etch for the regions for the resonator with central conductor width of 3 $\mu m$.

The participation ratio of the corner edges of the substrate-air interface also decreases significantly with over-etch. A similar trend is followed for higher central conductor widths. Another significant difference is observed at the intersection of the metal, air, and substrate, where participation reduces with over-etch depth, but this effect saturates around 1 $\mu m$. While the largest participation change is for the substrate-air at the bottom of the trench, and the probability of finding chemical residue is higher at the substrate-air interface at the corner of the trench. The trends are similar to those of the base, and both support an over-etch depth to significantly help to subdue TLS related losses.

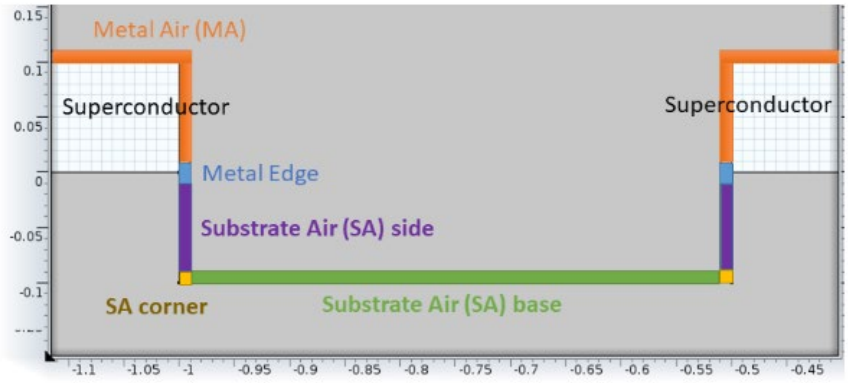


*Fig. 2.13 Schematic of regions for the participation ratios calculation*

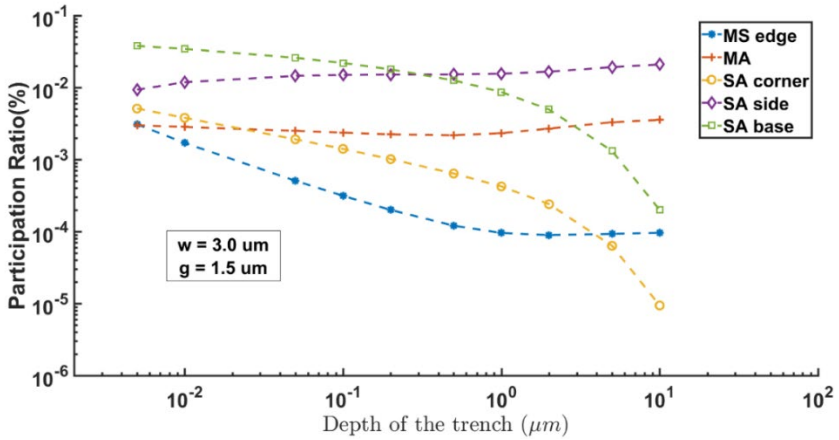


*Fig. 2.14: Participation Ratio calculated from the COMSOL simulation on different parts of the resonator surfaces.*

### 2.5.2 Losses from non-equilibrium quasiparticles

At low temperatures, the thermal quasiparticle density is negligible and minimally contributes towards loss which is the primary motivation to operate superconducting devices in low temperatures. Fig. 2.15 shows the temperature dependent quality factor due to thermal quasiparticles for an aluminum resonator. Losses are negligible compared to observed internal quality factors observed in the literature, at a qubit operating regime of T< 50 mK.

However, there is experimental evidence suggesting excess quasiparticles [11,12,57–60] contributing to the losses. In resonators, the losses are directly proportional to the excess quasiparticle density. These excess quasiparticles are one of the significant loss mechanisms in various devices by providing an undesired channel of energy relaxation. In qubits[21], [22] and single-electron transistors[26], tunneling quasiparticle through a Josephson junction competes with the Cooper pairs. In microwave detectors, they contribute to higher background noise.

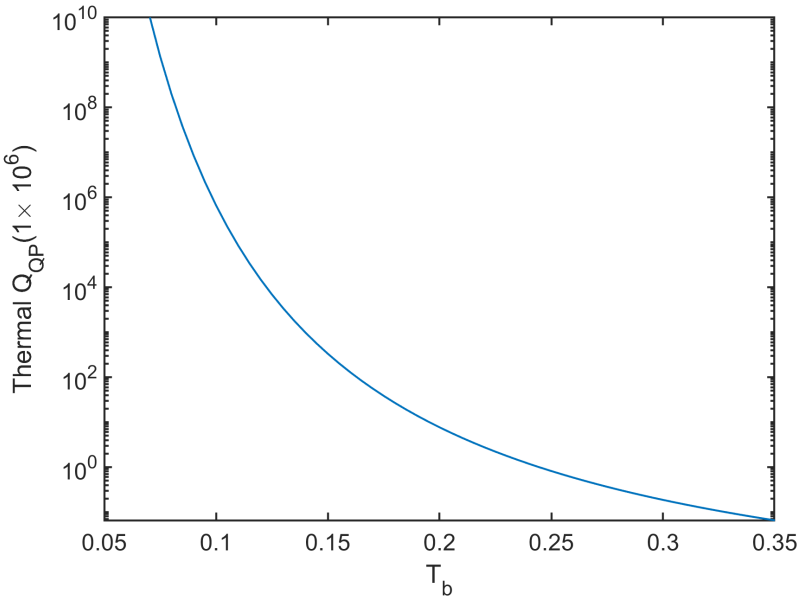


*Fig. 2.15: Quality factor calculated using* (2.37) *due to thermal quasiparticles for an Aluminum resonator with* $T_c$ *= 1.28K*

The precise origin of the excess quasiparticles is not clear. Any energy particle with energy greater than the superconducting gap (2Δ) generates quasiparticles by breaking Cooper pairs. The photons generated from stray infrared light from the higher temperature stages of the fridge[35], cosmic or gamma rays[88], or coupling of blackbody radiation with spurious antenna modes of the devices [89] can have significant energy relative to the superconducting bandgap and therefore have the potential to break Cooper pairs. The sequential absorption of probing sub-gap microwave photons can also excite a quasiparticle from the band edge to higher energy. When these higher energy quasiparticles relax, they may generate $\Omega > 2\Delta$ phonons capable of breaking Cooper pairs[90][91]. In the same way, non-thermalized input signals with a temperature greater than the bath temperature have increased the 2Δ phonon density number, which can further increase quasiparticle density[36].

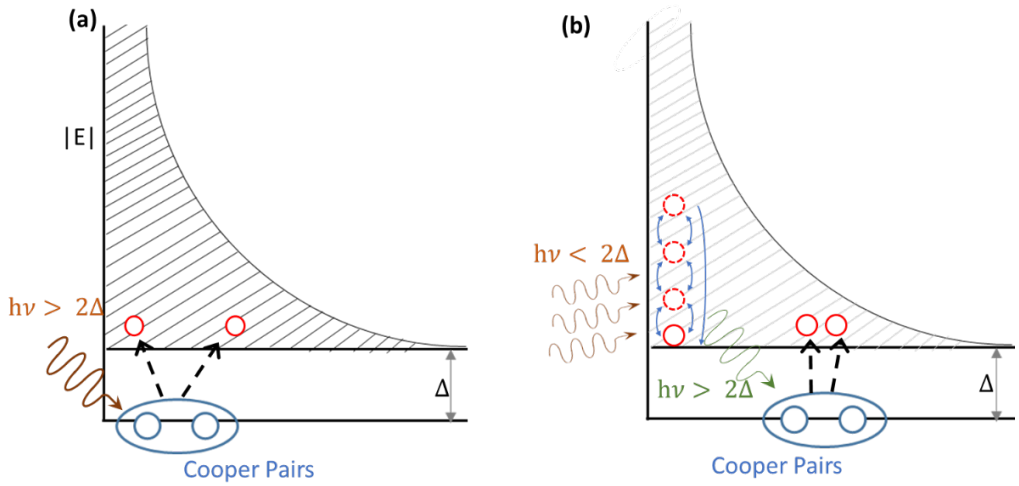


*Fig. 2.16:(a) QP generation with high energy photons like stray IR or gamma rays, (b) QP generation by multiple absorptions of microwave signals*

### 2.5.2.1 Coupled quasiparticle phonon distribution equations

There are various fully non-equilibrium non-thermal models described in the literature that rigorously track the quasiparticle ($f(E)$), and phonon distribution ($n(\Omega)$) functions. The distributions are calculated by solving coupled quasiparticle and phonon equations, first described by Chang and Scalapino[92]. The description of coupled equation follows the supplementary article of reference [32].

$$\frac{\partial}{\partial t} f(E) = I_{qp}(E) + \mathcal{I}_{em}(E) - \mathcal{I}_{rec}(E) - \mathcal{I}_{sct}(E) + \mathcal{I}_{pb}(E) \tag{2.43}$$

$$\frac{\partial}{\partial t} n(\Omega) = \; I_{ph}(\Omega) + \mathcal{L}_{em}(E) + \; \mathcal{L}_{rec}(E) - \; \gamma_{sc}(E) n(E) \\ - \; \gamma_{pb}(E) n(E) + - \frac{n(\Omega) - \; n(\Omega, \mathrm{T_b})}{\tau_l} \tag{2.44}$$

The individual terms of the quasiparticle distribution function are described in terms, $I_{qp}(E)$ and $I_{ph}(E)$ that describe the drive terms injecting non-equilibrium

quasiparticles (qp) and phonons (ph). The quasiparticle scattering with spontaneous emission of a phonon is described by

$$\mathcal{I}_{em}(E) = \frac{\beta}{\tau_0}\int_0^{\infty} d\Omega \frac{\Omega^2}{\Delta^3}\rho(E+\Omega)\left(1-\frac{\Delta^2}{E(E+\Omega)}\right)f(E+\Omega)[1-f(E)] \\ -\frac{\beta}{\tau_0}\int_0^{E-\Delta} d\Omega \frac{\Omega^2}{\Delta^3}\rho(E-\Omega)\left(1-\frac{\Delta^2}{E(\mathrm{E}-\Omega)}\right)f(E)[1-f(E-\Omega)], \tag{2.45}$$

and quasiparticle recombination is described by

$$\mathcal{I}_{rec}(E) = \frac{\beta}{\tau_0}\int_{\Delta+E}^{\infty} d\Omega \frac{\Omega^2}{\Delta^3}\rho(\Omega-\mathrm{E})\left(1+\frac{\Delta^2}{E(\Omega-\mathrm{E})}\right)f(\Omega-\mathrm{E})f(E). \tag{2.46}$$

The quasiparticle scattering from a phonon or stimulated emission and absorption of phonon is

$$\mathcal{I}_{sct}(E) = \frac{\beta}{\tau_0}\int_0^{\infty} d\Omega \frac{\Omega^2}{\Delta^3}\rho(E+\Omega)\left(1-\frac{\Delta^2}{E(E+\Omega)}\right)n(\Omega)[f(E)-f(E+\Omega)] \\ -\frac{\beta}{\tau_0}\int_0^{E-\Delta} d\Omega \frac{\Omega^2}{\Delta^3}\rho(E-\Omega)\left(1-\frac{\Delta^2}{E(\mathrm{E}-\Omega)}\right)n(\Omega)[f(E)-f(E-\Omega)]. \tag{2.47}$$

Cooper pair breaking is described by,

$$\mathcal{I}_{pb}(E) = \frac{\beta}{\tau_0}\int_{\Delta+E}^{\infty} d\Omega \frac{\Omega^2}{\Delta^3}\rho(\Omega-\mathrm{E})\left(1+\frac{\Delta^2}{E(\Omega-\mathrm{E})}\right)n(\Omega) \\ \times[1-f(\Omega-\mathrm{E})-f(E)]. \tag{2.48}$$

In this set of equations, $\beta = \frac{Z_1(0)\Delta^3}{(k_B T_C)^3}$ with $Z_1(0) = 1+\lambda$ where $\lambda$ is an electron-phonon coupling constant, and $\tau_o$ is the characteristic material-dependent quasiparticle-phonon interaction time constant[48].

The individual terms of the phonon distribution function are described as follows:

$\mathcal{L}_{em}(\Omega)$ describes the spontaneous phonon emission due to quasiparticle scattering

$$\mathcal{L}_{em}(\Omega) = 2\mathcal{L}_{pre}\int_{\Delta}^{\infty}\frac{dE}{\Delta}\rho(\mathrm{E}+\Omega)\rho(E)\left(1-\frac{\Delta^2}{E(\mathrm{E}+\Omega)}\right)f(\mathrm{E}+\Omega)[1-f(E)], \tag{2.49}$$

$\mathcal{L}_{rec}(\Omega)$ describes the recombination of two quasiparticles

$$\mathcal{L}_{em}(\Omega) = \mathcal{L}_{pre}\int_{\Delta}^{\Omega-\Delta}\frac{dE}{\Delta}\rho(\Omega-\mathrm{E})\rho(E)\left(1+\frac{\Delta^2}{E(\Omega-\mathrm{E})}\right)f(\Omega-\mathrm{E})f(E). \tag{2.50}$$

The scattering rate $\gamma_{sct}(\Omega)$ is described as

$$\gamma_{sct}(\Omega) = 2\mathcal{L}_{pre}\int_{\Delta}^{\infty}\frac{dE}{\Delta}\rho(\mathrm{E}+\Omega)\rho(E)\left(1-\frac{\Delta^2}{E(\mathrm{E}+\Omega)}\right)[f(E) - f(\mathrm{E}+\Omega)]. \tag{2.51}$$

The pair breaking rate $\gamma_{pb}(\Omega)$ is described as

$$\gamma_{pb}(\Omega) = \mathcal{L}_{pre}\int_{\Delta}^{\Omega-\Delta}\frac{dE}{\Delta}\rho(\Omega-\mathrm{E})\rho(E)\left(1+\frac{\Delta^2}{E(\Omega-\mathrm{E})}\right)[1-f(\Omega-\mathrm{E}) - f(E)]. \tag{2.52}$$

In this set of equations, $\mathcal{L}_{pre} = \frac{b\beta}{\tau_0}\frac{N(0)}{D(\Omega)}\frac{\Omega^2}{\Delta^2}$ with $D(\Omega)$ is phonon density of states per unit volume, and $b$ is a characteristic material constant corresponding to phonon density at low frequencies[48]. The final term in Eq. (2.44) describes the escape of phonons to the substrate with a phenomenological term $\gamma_{esc}$. The coupled kinetic equations relating quasiparticles and phonons are solved for different drive conditions by various research groups[91]–[93].

The solutions for the pair-breaking photons or phonons and sub-gap microwave photons are of great interest for resonators. The solution depends on the correct choice of quasiparticle or phonon drive terms. A pair breaking photon or phonon, $h\nu > 2\Delta$, breaks a Cooper pair creating quasiparticles with excess energy of $h\nu - 2\Delta$. For high-energy quasiparticles, scattering is faster than recombination[48]. The relaxation of these high-energy quasiparticles via electron-phonon interactions to the band edge releases the excess energy in the form of phonons. If the released phonon is greater than pair breaking energy, it can further break Cooper pairs or escape into the substrate. The phonon escape times depend on the film and substrate interface and material properties and may be long compared to the generation rate. Hence the absorption of a single high-energy photon can break more than one Cooper pair. The excess energy determines the modeling disturbance using phonons or quasiparticles drive term. A low energy pair-breaking photon ($E < 4\Delta$) break a single Cooper pair and is described by the quasiparticle drive term. On the other hand, the optical photons have energies almost $10^3$ -$10^4$ times the bandgap of superconductors, and hence the quasiparticles generated by a single photon would create multiple phonons before finally relaxing to the bandgap edge. Hence the optical phonon is better modeled as a phonon drive term than quasiparticle term[92], [93]. On the other hand, the stimulation by subgap microwave photons is described as a quasiparticle-driven term. [91], [92], which is given in Eq. (2.53)

$$\mathrm{I_{qp}}(E, \omega_p) = B\left(g(E, E + \hbar\omega_p) + g(E, E - \hbar\omega_p)\right)\Theta(E - \Delta) \qquad (2.53)$$

where $\Theta(E)$ is the Heaviside step function, $B$ depends on microwave photon absorption rate which in turn depends on the input power and $g(E, E')$ is defined as

$$g(E,E') = \rho(E')\left(1+\frac{\Delta^2}{EE'}\right)\big(f(E')-f(E)\big) \tag{2.54}$$

These systems of equations need to be recursively solved to obtain a steady-state solution. Fig. 2.17 shows quasiparticle distribution and phonon power flow as a solution of the coupled equations for various microwave power[91]. The microwave driven quasiparticle distribution has a characteristic $\hbar\omega_p$ spaced multipeak features where the $\hbar\omega_p$ is the microwave signal. This also gets reflected in the phonon power flow. One of the critical aspects is the increased power carried by low-energy phonons $\Omega < 2\Delta$ by scattering compared to the thermal distribution.

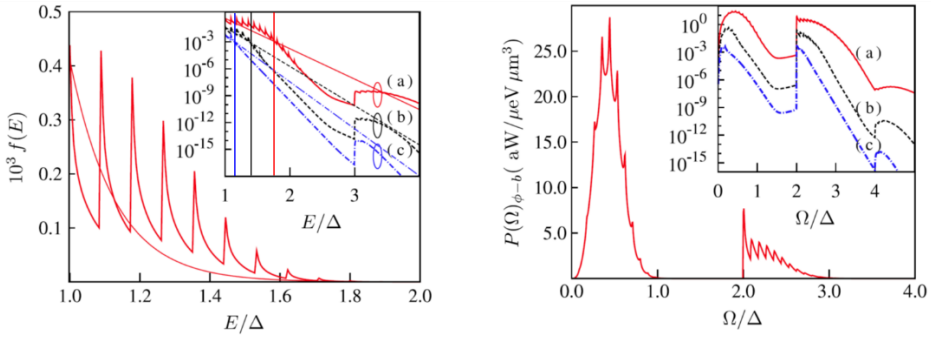


*Fig. 2.17: (a) The quasiparticle distribution for absorbed power 2 fWμm$^{-3}$ microwave signal for temperature $T_b/T_c$ = 0.1 with phonon escape rate being equal to cooper pair breaking rate. The inset also shows the distribution for energies 2 fWμm$^{-3}$, 20* aW *μm$^{-3}$*and 0.2 aW *μm$^{-3}$*. The dotted line shows the effective temperature for each distribution. (b) shows the corresponding power flow by excess phonons escaping from the film for each microwave power[91].

These calculations are extended to model a temperature and power dependent quality factor of an open half-wavelength CPW resonator. The resonators were fabricated on 65 nm thick sputtered aluminum film on a sapphire substrate with a resonant frequency f = 5.28 GHz and a coupling quality factor of 20k[49]. The resonators are measured for temperatures 65 mK to 350 mK with the readout power in the power range of -64 dBm to -100 dBm, which corresponds to photon numbers ranging $5 \times 10^4 - 10^8$. For temperatures less than 200 mK, the measured quality factor $Q_i$ decreases with

increasing power while at high temperatures $Q_i$ increases with increasing power. For the measured power range, the TLS losses are insignificant and non-equilibrium quasiparticles are the dominant loss mechanism. The result of the non-equilibrium model calculated by solving coupled equations is presented in Fig. 2.18. The model captures the trend for various microwave power levels for high temperature pretty well but at transition temperatures, overestimates $Q_i$ compared to the measured data. The non-trivial increase of $Q_i$ with power was explained by the depletion of quasiparticle distribution for $\Delta < E < \Delta + \hbar\omega$ leading to decreased losses.

The model was extended to include the contribution of pair breaking photons with sub-gap photons to calculate the quasiparticle generation efficiency in superconducting films [94]–[96]. The pair breaking photons ranged from $2\Delta \leq E \leq 10\Delta$ and solved for different materials such as Al, Nb and Ta.

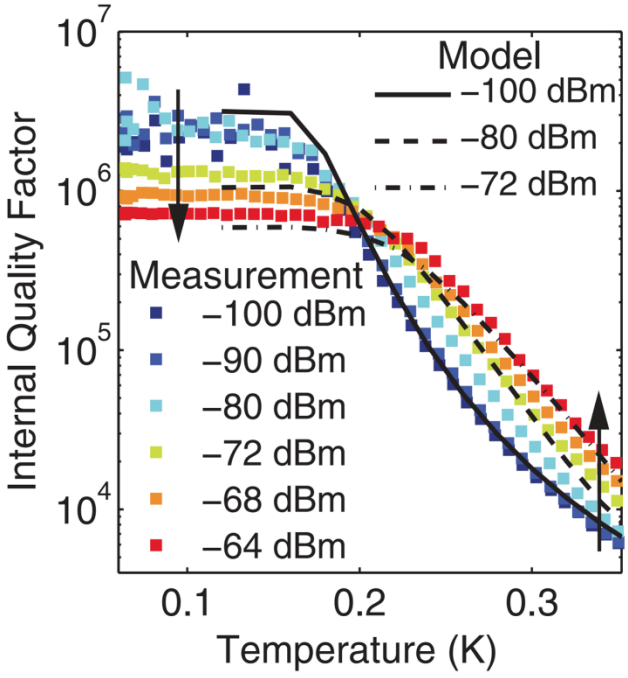


*Fig. 2.18: Temperature dependent quasiparticle quality factor modeled using complete non-equilibrium model*[49]

The non-equilibrium model has also been applied to model the impact of optical illumination on aluminum superconducting resonators[93]. The CPW resonators designed using lumped inductor and capacitor were fabricated on 200 nm sputtered aluminum film on sapphire. The fabricated resonator was coupled with a 3D cavity with a coupling quality factor of $8.5 \times 10^9$. The resonators were measured at microwave powers of -70 dBm to -45 dB, corresponding to rf photons of $5 \times 10^4 - 10^8$ for a temperature range of 25mK to 300mK. The optical illumination had energy E ~ 9000Δ which created significantly more pair breaking phonons after initial pair breaking by one photon. The significant feature of the measured data was the increase of quality factor with increasing power at all temperatures for resonators with and without illumination. The increasing $Q_i$ with increasing microwave power was explained by the reduction of the quasiparticle density at $\Delta \leq E \leq \Delta + \hbar\omega$. The data were fitted with the model where the optical drive is represented by the phonon drive term in Eq. (2.55) and the quasiparticle drive term is set by probing microwave signals by Eq. (2.53)

$$I_{ph}(\Omega) = \frac{1}{\tau_e} \begin{cases} 0, & \text{for } \Omega < 2\Delta \\ 1 \Big/ \left( e^{\frac{\Omega}{k_B T^*_{eff}}} - 1 \right) & \text{for } \Omega > 2\Delta \end{cases} \tag{2.55}$$

The phonon drive term is approximated by the non-thermal distribution of phonons with $\Omega > 2\Delta$. The Bose-Einstein thermal distribution with temperature, $T^*_{eff}$, approximates the total number of pair breaking phonons while low energy phonons are ignored[93].

### 2.5.2.2 Effective temperature approximation

Microwave-driven quasiparticle and phonon distributions are athermal. But it is computationally intensive to calculate the solution for every time step. Hence attempts were made to model the overall quasiparticle distribution with a thermal distribution described by an effective temperature, $T_{eff}$, such that the total number of quasiparticles calculated by athermal distribution can be described as

$$n_{qp} = 4N(0)\int_{\Delta(T_{eff})}^{\infty} f\left(E, T_{eff}\right)\frac{E}{\sqrt{\left(E^2 - (\Delta(T_{eff}))^2\right)}}dE. \tag{2.56}$$

A comparison of an athermal and "equivalent" thermal distribution due to sub-gap microwaves is shown in Fig. 2.17. For energy $E < \Delta + \hbar\omega$, the thermal approximation predicts a higher distribution than the non-equilibrium calculations while for the energy range, $\Delta + \hbar\omega < E < 2\Delta'$the driven distribution shows excess quasiparticles compared to the thermal equivalent. The difference between thermal and athermal distributions increases with increasing microwave power.

A comparison [96] of an athermal distribution due to high energy photons ($2\Delta \leq \hbar\omega \leq 10\Delta$) and microwave signal is shown in Fig. 2.19. The figure also includes the effective thermal distribution for each case. The simulation is performed for a high microwave signal average power of 2 fW $\mu m^{-3}$ with high energy photons with an average power of 2 aW $\mu m^{-3}$.

The presence of external stimulation (either microwave or high-energy) raises the quasiparticle distribution compared to the equilibrium thermal distribution. The critical difference between the quasiparticle distribution driven by a high energy infrared or optical photon (E>>2 Δ) and a low energy microwave photon (E<2 Δ) is

that the higher energy photons tend to create quasiparticles with energies near the band edge, while the microwave photons increase the quasiparticles above the band edge. Since the density of states is very high near the band edge, the high-energy photons do not significantly change the distribution of quasiparticles from a thermal distribution described with $T_{eff}$. Hence the steady-state quasiparticle distributions from pair breaking phonons or photons having energy range $2\Delta < E < 10\Delta$ is effectively estimated using a thermal distribution from an increased effective temperature [96][55], but may not be valid for high power microwave driven distributions.

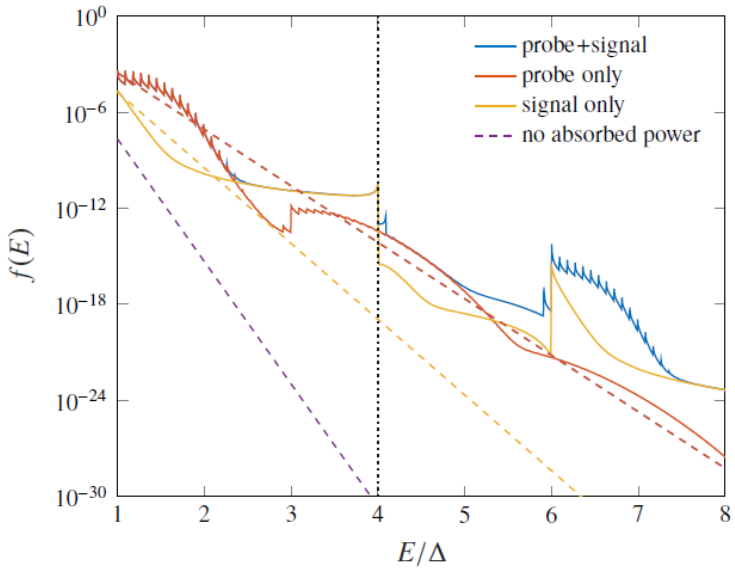


*Fig. 2.19: The comparison of QP distribution for different drive conditions of sub-gap microwave signal and pair breaking signals*[96]

### 2.5.2.3 Rothwarf Taylor equations

Rothwarf Taylor rate equations describe the quasiparticle and pair breaking phonon dynamics using their number density instead of distribution functions[97]. The pair-breaking phonon density,$N_{2\Delta}$, and quasiparticle densities, $n_{qp}$, are defined as follows.

$$N_{2\Delta} = N_{ion} \int_{2\Delta}^{\infty} n(\Omega\,) F(\Omega)\, d\Omega \tag{2.57}$$

$$n_{qp}\ = 4N(0) \int_{\Delta}^{\infty} f(E) \rho(E)\, dE \tag{2.58}$$

Where $n(\Omega)$ is the phonon distribution function and $f(E)$ is the quasiparticle distribution function, while $F(\Omega)$ and $\rho(E)$ are the phonon and quasiparticle density of states. The relationship between these equations is

$$\frac{\partial}{\partial t} n_{qp} = I_{ext} + \beta N_{2\Delta}\ - R n_{qp}^2, \tag{2.59}$$

$$\frac{\partial N_{2\Delta}}{\partial t} = \frac{1}{2} R_{qp} n_{qp}^2 - \frac{1}{2} \beta N_{2\Delta} - \gamma \left( N_{2\Delta} - N_{2\Delta, T_b} \right) \tag{2.60}$$

where $R_{qp}$ is the quasiparticle recombination rate, $\beta$ is the pair breaking rate, and $\gamma$ is the phonon escape rate. $I_{ext}$ is the combined external quasiparticle and phonon drive term.

Chang and Scalapino[92] derived the Rothwarf Taylor equations by integrating the quasiparticle distribution function, $f(E)$, for energies $E \geq \Delta$ and the phonon distribution function, *n(Ω),* for energies $\Omega \geq 2\Delta$. For $f(E)$, the terms related to scattering cancel each other, and only the terms related to pair breaking, and recombination remain apart from the quasiparticle drive term. For phonon distributions, the scattering term is either ignored or, in the presence of significant quasiparticles with $E > 3\Delta$, is combined with the drive term. The recombination constant and pair breaking term can be written in terms of $f(E)$ and $n(\Omega)$ as follows.

$$R_{qp} = \frac{2N(0)}{n_{qp}^2}\int_{\Delta}^{\infty} dE f(E)\rho(E)\int_{\Delta}^{\infty} dE'\,\rho(E')(E+E')^2 \times\left(1+\frac{\Delta^2}{EE'}\right)f(E')(n(E+E')+1) \tag{2.61}$$

$$\beta = \frac{2N(0)}{N_{2\Delta}}\int_{\Delta}^{\infty} dE\, f(E)\rho(E)\int_{\Delta}^{\infty} dE'\,\rho(E)\rho(E')(E+E')^2 \times\left(1+\frac{\Delta^2}{EE'}\right)(1-f(E))(1-f(E'))(n(E+E')) \tag{2.62}$$

### 2.5.3 Loss through vortices

In Type II superconductor, for the magnetic field higher than the lower critical field ($H_{C_1}$) of the material, the magnetic field is not completely expelled from the superconductor. There are regions in the material where penetration of the magnetic field creates current loops in the superconductor, with each of them carrying a single quantum flux $\Phi_o = \frac{hc}{2e}$. These vortices act as a material in the normal state with a gap parameter, $\Delta$, goes to zero at the center of these vortices[45]. Below certain critical thickness, thin films of bulk type-I superconductors behave like type-II superconductors in the presence of the magnetic field[98]. If vortices are present in a high current density region, it leads to losses. The loss depends on the magnetic field strength and a threshold cooling field where the vortices are trapped. This field is material-dependent.[99]. The wider superconducting traces are more susceptible to these losses.

### 2.5.4 Radiative loss

Resonators can lose energy by radiating the energy out of the transmission line to the free space to interact with the lossy package walls and lossy dielectrics. The loss due to radiation is device size and operating frequency-dependent[61]. Using the calculations for the fields for slot antennas, the radiative limit to a resonator quality factor is calculated as[100]

$$Q_{Rad} \approx 5 \times 10^{-3} \left(\frac{\lambda_o}{w}\right)^2, \tag{2.63}$$

where $\lambda_o$ is the free space wavelength of the microwave signal, and $w$ is the central conductor width of the resonator. Some of the techniques suggested to reduce radiation loss are lower frequencies, smaller resonator dimensions [62,79], and a superconducting package[67].

### 2.5.5 Parasitic modes

The resonator can couple with the unwanted modes in the packages and circuit and suffer loss. The most prominent is the slot line modes in the coplanar waveguides if the ground planes are not in the same potential. They are very dispersive in nature [57]. These modes can be eliminated by having wirebonds[101] or airbridges[102] between the ground planes. The parasitic capacitance due to the wirebonds can be reduced by having closely spaced and shorter wirebonds[101]. While connecting the signal line from PCB to chip, multiple wirebonds reduce the impedance mismatch and decrease the parasitic capacitance[103].

The package holding the resonator has cavity modes that can interact with the resonators[103]. The box-like cavity can only support TE or TM modes, and the cutoff frequency for the rectangular cavity is given as[59]

$$f_{mnl} = \frac{c}{2\pi\sqrt{\epsilon_r \mu_r}} \sqrt{\left(\frac{m\pi}{a}\right)^2 + \left(\frac{n\pi}{b}\right)^2 + \left(\frac{l\pi}{d}\right)^2} \tag{2.64}$$

Where m,n,l are the possible $TE_{mnl}$ or $TM_{mnl}$ mode and a, b, d are the dimensions of the package. The presence of the dielectrics in the package further reduces the cutoff frequency[104]. The correct choice of the cavity dimension can be used to eliminate any coupling between resonator and package.

The interaction between the chip and the underlying package floor can be further reduced by introducing an air cavity underneath it[105]. The balance between chip thermalization and coupling with cavity modes determines the cavity size underneath the chip.

# Chapter 3 : Non-equilibrium resonator quality factor

## *3.1 Modified quality factor due to non-equilibrium quasiparticles*

The energy-dependent equations are computationally intensive for the fully nonlinear model, and they include several poorly known material-dependent parameters required for the calculations. In this chapter, I explore the feasibility of a simpler model that relaxes the condition of thermal equilibrium between particles (quasiparticles, Cooper pairs, and phonons) and uses an effective temperature as a parameter to set the number density of a given particle type. That is, I assume that the highly athermal quasiparticle distribution can be modeled using an effective quasiparticle temperature that is not equal to the bath temperature. The model is a compromise that allows most non-equilibrium behavior to be captured but does not capture the rich athermal distributions that may be present during routine measurements in our laboratory experiments.

A similar approximation for the quasiparticle density can be performed by assuming a quasi fermi level [55]. As phonon density with energy $\Omega > 2\Delta$ and quasiparticle density are coupled, tracking phonon density, which follows a Bose-Einstein statistics, using the effective temperature model would be more reasonable to handle.

For the resonators in consideration for my work, the sources of non-equilibrium quasiparticles in the superconductor are pair-breaking background radiation photons that manage to couple into the resonator and the applied sub-gap microwave drive. The exact source of the non-equilibrium quasiparticles is unknown and but I assume it to

be broadband. I am interested in tracking losses at power ranges as low as a single photon number where TLS defects also contribute towards loss. The fully non-equilibrium simulated models described in the previous chapter operated at much higher photon numbers where TLS losses were not included. As discussed in the last chapter, for low microwave powers, the deviation from the thermal distribution is expected to be minor, hence an effective temperature model might be reasonable. Additionally, at low powers, the TLS losses cannot be ignored entirely. I evaluate the contribution from both TLS and quasiparticle in my study.

### 3.1.1 Relation between non-equilibrium and equilibrium QP

In a superconductor, the quasiparticle and phonons with energy $\Omega > 2\Delta$ are interdependent as quasiparticle creation via Cooper pair breaking is accompanied by phonon annihilation and vice versa. Hence to calculate the quasiparticle number density, the combined rate equations of phonon and quasiparticle number densities need to be solved. I used a modified version of Rothwarf Taylor equations[97].

$$\left(\frac{\partial}{\partial t} - D_{qp}\frac{\partial^2}{\partial x^2}\right) n_{qp} = I_{ext} + \beta N_{2\Delta} - R_{qp} n_{qp}^2 - s\left(n_{qp} - n_{qp,T_b}\right) \qquad (3.1)$$

$$\frac{\partial N_{2\Delta}}{\partial t} = \frac{1}{2} R_{qp} n_{qp}^2 - \frac{1}{2}\beta N_{2\Delta} - \gamma\left(N_{2\Delta} - N_{2\Delta,T_b}\right) \qquad (3.2)$$

Here $n_{qp}$ is the total number density includes both thermal and athermal quasiparticles, $N_{2\Delta}$ is the phonon number density of all phonons having an energy greater than $2\Delta$, which have sufficient energy to break Cooper pairs. In Eq. (3.1), the terms on the left include the spatial diffusion of quasiparticles with diffusivity, D, and the time variation of the quasiparticle density. The first term on the right include the excess

generation rate of quasiparticles, $I_{ext}$, the second term, $\beta N_{2\Delta}$, is the quasiparticles generated by phonons with $\Omega > 2\Delta$, the third term, $R_{qp}n_{qp}^2$, describes quasiparticle due recombination and the final term, $s\left(n_{qp} - n_{qp,T_b}\right)$, describes quasiparticle trapping. In Eq. (3.2), the first term, $\frac{1}{2}R_{qp}n_{qp}^2$, describes generation of $2\Delta$ phonons from quasiparticle recombination, the second term, $\frac{1}{2}\beta N_{2\Delta}$, describes the loss of phonons due to Cooper pair breaking, and the last term, $\gamma\left(N_{2\Delta} - N_{2\Delta,T_b}\right)$, is for phonons leaving the superconducting film.

For resonators, solving these equations in the steady-state such that quasiparticle or phonon numbers don't change temporally or spatially, the equations become:

$$0 = I_{ext} + \beta N_{2\Delta} - R_{qp}n_{qp}^2 - s\left(n_{qp} - n_{qp,T_b}\right) \tag{3.3}$$

$$0 = \frac{1}{2}R_{qp}n_{qp}^2 - \frac{1}{2}\beta N_{2\Delta} - \gamma\left(N_{2\Delta} - N_{2\Delta,T_b}\right) \tag{3.4}$$

For the case of equilibrium when the external generation rate, $I_{ext} = 0$, the particle numbers are in thermal equilibrium numbers with the bath temperature, $n_{qp} = n_{qp,T_b}$ and $N_{2\Delta} = N_{2\Delta,T_b}$. Under this situation, Eq. (3.4) gives

$$N_{2\Delta,T_b} = \frac{R_{qp}}{\beta}n_{qp,T_b}^2 \tag{3.5}$$

For the non-equilibrium case when $I_{ext} \neq 0$, solving eq. (*3.4)* for $N_{2\Delta}$ gives

$$N_{2\Delta} = \frac{R_{qp}}{(\beta + 2\gamma)}\left\{n_{qp}^2 + \frac{2\gamma}{\beta}n_{qp,T_b}^2\right\} \tag{3.6}$$

Substituting calculated $N_{2\Delta}$ back to Eq. (3.3) and defining effective recombination rate $r = \left(\frac{1}{R_{qp}}\left(1 + \frac{\beta}{2\gamma}\right)\right)^{-1}$ the external quasiparticle generation rate is

$$r\left(n_{qp}^2 - n_{qp,T_b}^2\right) + s\left(n_{qp} - n_{qp,T_b}\right) = I_{ext}. \tag{3.7}$$

For simplicity, I assumed $R_{qp}, \beta$ and $\gamma$ were independent of temperature for $\frac{T}{T_c} < 0.3$ and given by Eqs. (2.10) - (2.12). Substituting $R_{qp}$ from eq. (*2.10)* into eq. 3.7 yields

$$r = \left(\frac{1}{N(0)\Delta(\mathrm{T})}\right)\left(\frac{2}{\tau_0}\right)\left(\frac{\Delta(\mathrm{T})}{k_B T_C}\right)^3\left(1 + \frac{\beta}{2\gamma}\right)^{-1}. \tag{3.8}$$

Defining $n_{trap} = \frac{s}{2r}$ and $I_o = \frac{I_{ext}}{r}$ and solving Eq. (3.7) for $n_{qp}$ produces

$$n_{qp} = -n_{trap} + \sqrt{I_o + \left(n_{qp,T_b} + n_{trap}\right)^2}. \tag{3.9}$$

This relation can be further rewritten as

$$\left(n_{qp} + n_{trap}\right)^2 - \left(n_{qp,T_b} + n_{trap}\right)^2 = I_o \tag{3.10}$$

The quasiparticle number density can be normalized with respect to the single spin electron density and superconductor bandgap to get a value for the normalized quasiparticle density, $x_{qp} = \frac{n_{qp}}{N(0)\Delta_0}$. The modified equation is

$$x_{qp} = -x_{trap} + \sqrt{\left(I_o^* + \left(x_{qp,T_b} + x_{trap}\right)^2\right)} \tag{3.11}$$

where $x_{trap} = \frac{s}{2r^*}$ and $I_o^* = \frac{I_{ext}^*}{r^*}$ . Here the normalized external generation rate $I_{ext}^* = \frac{I_{ext}}{N(0)\Delta_o}$ and effective recombination rate is $r^* = r \times (N(0)\Delta_o) \sim \left(\frac{2}{\tau_0}\right)(1.76)^3\left(1 + \frac{\beta}{2\gamma}\right)^{-1}$. It helps in eliminating a material dependent parameter $N(0)$ from the set of equations.

### 3.1.2 Two temperature model

IN this section, I discuss the effective temperature model in which quasiparticle number density is assumed to have a thermal distribution with an effective temperature $T_{qp}$, which can be different from the bath temperature $T_b$ such that

$$n_{qp}(T_{qp}) = 4N(0)\int_{\Delta(T_{qp})}^{\infty} f(E,T_{qp})\frac{E}{\sqrt{(E^2-(\Delta(T_{qp}))^2)}}dE. \tag{3.12}$$

It is important to note that under an applied microwave drive or quasiparticle generated from higher energy photons, the actual quasiparticle distribution will not be accurately described by this equation. As I discussed the previously in chapter, the quasiparticle temperature, $T_{qp}$, used here is an effective quasiparticle temperature that is mainly used to set the quasiparticle density, while the impact on the distribution in energy distribution is undesirable.

The conductivity due to the quasiparticles and Cooper pairs (Eqs. (2.16) and (2.17) ) are modified by replacing the quasiparticle distribution function with the fermi distribution corresponding to effective temperature $T_{qp}$. The modified equations are:

$$\frac{\sigma_1(\omega,T_{qp})}{\sigma_n} = \frac{2}{\hbar\omega}\int_{\Delta(T)}^{\infty}\left[f(E,T_{qp}) - f(E+\hbar\omega,T_{qp})\right]g_1(E,T_{qp})\ dE \tag{3.13}$$

$$\frac{\sigma_2(\omega,T_{qp})}{\sigma_n} = \frac{1}{\hbar\omega}\int_{\Delta(T)-\hbar\omega}^{\Delta(T)}\left[1-2f(E+\hbar\omega,T_{qp})\right]g_2(E,T_{qp})\,dE \tag{3.14}$$

Where $g_i(E,T)$ is the product of coherence factor and density of states and expressed as:

$$g_1(E, T_{qp}) = \frac{\left(E(E+\hbar\omega) + \Delta(T_{qp})^2\right)}{\sqrt{E^2 - \Delta(T_{qp})^2}\sqrt{(E+\hbar\omega)^2 - \Delta(T_{qp})^2}} \tag{3.15}$$

$$g_2(E, T_{qp}) = \frac{\left(E(E+\hbar\omega) + \Delta(T_{qp})^2\right)}{\sqrt{\Delta(T_{qp})^2 - E^2}\sqrt{(E+\hbar\omega)^2 - \Delta(T_{qp})^2}} \tag{3.16}$$

Variation of the superconducting bandgap $\Delta$ depends on the quasiparticle distribution, as shown in Eq. (2.1). Hence the variation of the bandgap is made as a function of quasiparticle temperature. From the conductivity, the internal quality factor $Q_I$ can be rewritten as

$$\frac{1}{Q_I} = \frac{L_s}{L_g}\frac{\sigma_1(\omega, T_{qp})}{\sigma_2(\omega, T_{qp})} \tag{3.17}$$

where the kinetic inductance $L_s(\omega, T_{qp}, T_b) = \frac{1}{\omega}\left(\frac{g_{geom}}{w}\right)\left(\frac{1}{d\sigma_N}\right)\left(\frac{1}{\sigma_2(\omega,T_{qp})/\sigma_N}\right)$.

For a given external quasiparticle generation rate $I_{ext}$, the quasiparticle number, $n_{qp}$, is calculated from Eq. (3.9). Using Eq. (3.12), the effective quasiparticle temperature $T_{qp}$ is determined. This $T_{qp}$ is applied to Eq. (3.13)-(3.17) to calculate the quasiparticle quality factor.

## *3.2 Combined power and temperature dependent quality factor*

The total loss in a resonator can be calculated by combining loss from quasiparticles and TLSs with all other sources of loss. I assume that all the other losses are not dependent on power and temperature, and I combine them in a single term $Q_A$. The TLS loss from the standard distribution of TLSs can be modeled by 3 parameters: $Q_{TLS}^0$, $n_c$ and $\alpha$ that are adopted from Eq. (2.40). In my effective temperature model, the

quasiparticle loss is described by 4 parameters: $I_{ext}$, $s$, $\kappa$ and $T_c$. The total quality factor for a resonator is then given by

$$\frac{1}{\mathbf{Q_i(T_b, n_p)}} = \frac{1}{Q_A} + \frac{1}{Q_{TLS}^0} \frac{1}{\sqrt{1+\left(\frac{\mathbf{n_p}}{n_c}\right)^{\alpha}}} \tanh\left(\frac{\hbar\omega_{res}}{2k_B\mathbf{T_b}}\right) + \boldsymbol{\kappa}\frac{L_s(\omega_{res}, \mathbf{T_{qp}}, \mathbf{T_b})}{L_m}\frac{\sigma_1(\omega_{res}, \mathbf{T_{qp}}, \mathbf{T_b})}{\sigma_2(\omega_{res}, \mathbf{T_{qp}}, \mathbf{T_b})}. \quad (3.18)$$

In addition, Eq. (3.10) gives,

$$\left(n_{qp} + \frac{s}{2r}\right)^2 - \left(n_{qp,T_b} + \frac{s}{2r}\right)^2 = I_o \quad (3.19)$$

Using BCS theory, the relationship between the critical temperature and the superconducting gap is

$$\Delta(0) = 1.76 k_B T_c \quad (3.20)$$

The resonator frequency, $\omega_{res}$, applied microwave power, $n_p$, and sample (bath) temperature, $T_b$ , are three control variables. For the resonators I examined, the observed variation in the resonant frequency by calculating the ratio of the standard deviation of resonance frequency by mean resonance frequency for temperature and power separately. For power, the ratio is $10^{-6}$-$10^{-7,}$ while for temperature, the ratio is $10^{-5}$-$10^{-6}$. To simplify the analysis, I took the resonator frequency to be constant.

For the quasiparticle loss, I have included an additional phenomenological variable $\kappa$ to capture any excess loss that can't be described by the thermal distribution approximation of non-equilibrium quasiparticles. This phenomenological variable can be used as a measure of the fitness of the model. If $\kappa$ is close to 1, then the effective temperature model inadequately describes the loss. However, if $\kappa$ varies significantly from 1, other factors such as athermal particle distributions that are not captured well

with this model are essential. Additionally, the clear trend for the trapping rate, s, and excess quasiparticle loss parameter, $\kappa$, is unknown; they are therefore allowed to be a function of applied microwave power. The functional terms $n_{qp}$, $\sigma_1$, $\sigma_2$, $L_s$ and $\Delta(T)$ are defined in earlier sections, and the geometry inductance term is defined by Eq. (2.35). The recombination rate, pair breaking rate, and phonon escape rate defining effective recombination rate are taken from the literature. The different parameters describing the model are summarized below in Table 3-1.

*Table 3-1: Description of parameters of the temperature power model for resonator quality factor*

| **Parameter** | **RF Power dependence** | **Loss Mechanism** | **Detail** |
|---|---|---|---|
| $Q_A$ | No | Non-TLS, Non-QP | Terms including losses form vortices, packaging, and other loss terms |
| $Q_{TLS}^0$ | No | TLS | The average loss tangent of various TLS defects present on the dielectrics around a resonator |
| $n_c$ | No | TLS | Average critical photon number determining the electric field saturation of TLSs |
| α | No | TLS | The fit parameter to include power variation of an ensemble of TLSs |
| $T_c$ | No | QP | The superconducting critical temperature of the film |
| $I_{ext}$ | No | QP | External generation rate |
| $s$ | Yes | QP | Quasiparticle trapping rate |
| $\kappa$ | Yes | QP | Excess QP loss parameter to include loss which is not fully captured by the effective temperature approximation |

## 3.3 *Discussion*

The presence of non-equilibrium quasiparticles leads to a non-vanishing density and low-temperature saturation of $Q_{QP}$. The thermal quasiparticle density is negligible at low temperatures, and net quasiparticle density is given by Eq. (3.11) modifies into

$$x_{qp,T_{low}} = -x_{trap} + \sqrt{\left(I_o^* + x_{trap}{}^2\right)} \tag{3.21}$$

This equation is constant for temperature and is dependent on $x_{trap}$ and $I_o^*$ which in turn depends on the external generation rate $I_{ext}$ and trapping rate s. The saturation of quasiparticles at low temperatures leads to saturation of the corresponding quality factor. Increasing $I_{ext}$, increases $x_{qp,T_{low}}$ while increasing $s$ decreases $x_{qp,T_{low}}$. The impact on quasiparticle quality factor $Q_{Qp} \propto \frac{1}{x_{qp}}$ is shown in Fig. 3.1 and Fig. 3.2.

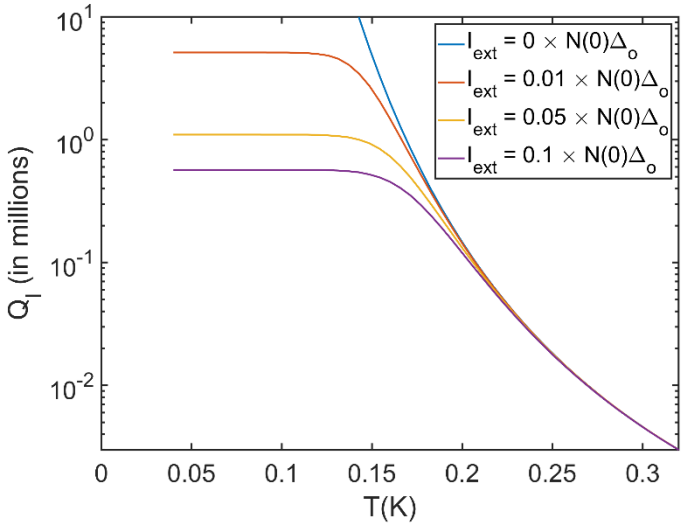


*Fig. 3.1: Impact of variation of $I_{ext}$ on quality factor for trapping rate $10^4$*

It is important to note that s and $I_{ext}$ cannot be uniquely determined from a single value of $n_{qp}$. For example, with all other parameters being the same, $I_{ext} =$

$0.1 \times N(0)\Delta_o$ and s = $10^4$ gives the similar $x_{qp,T_{low}}$ for $I_{ext} = 0.01 \times N(0)\Delta_o$ , s = $10^3$.

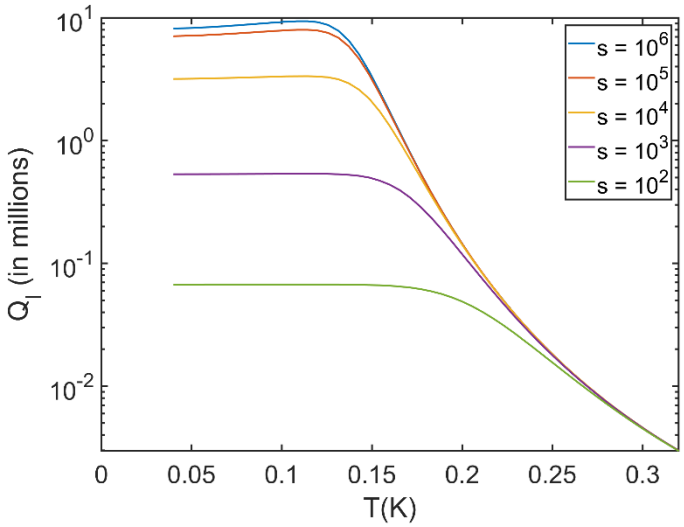


*Fig. 3.2 Variation of $Q_I$ with changing trapping rate for a given external generation rate $I_{ext}$*

On the other hand, $\kappa$ is directly proportional to the quasiparticle loss and hence increasing $\kappa$ decreases the $Q_{qp}$. The impact $\kappa$ is shown in Fig. 3.3. All these trends are plotted with negligible contribution from TLS and non-TLS, non-QP losses. Similar trends for the power dependence cannot be predicted as the exact power dependence of $I_{ext}$ and s is not known.

In the presence of the significant TLS loss, the curvature for the low and intermediate temperature region changes. For increasing temperature, an increasing $Q_{TLS}$ and a decreasing $Q_{QP}$ generate a quality factor peak at an intermediate temperature, as shown in Fig. 3.4. Hence, the fitting of my model at low temperatures is dictated by all TLS parameters and non-equilibrium QP parameters.

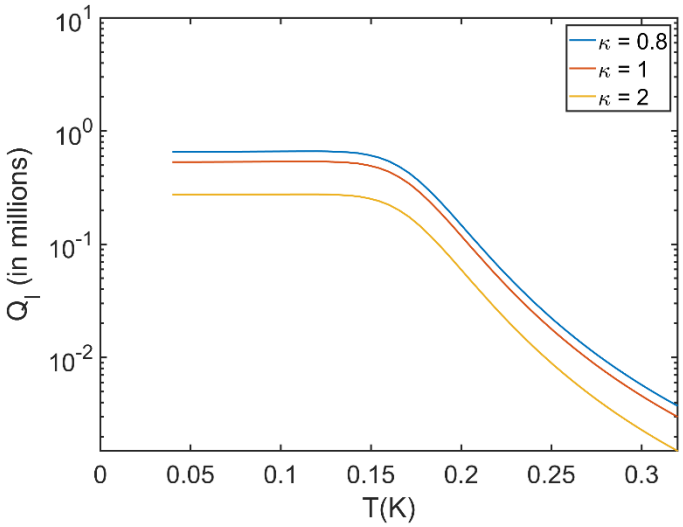


*Fig. 3.3: Variation of $Q_I$ versus temperature for different values of κ.. Increasing κ reduces $Q_I$*

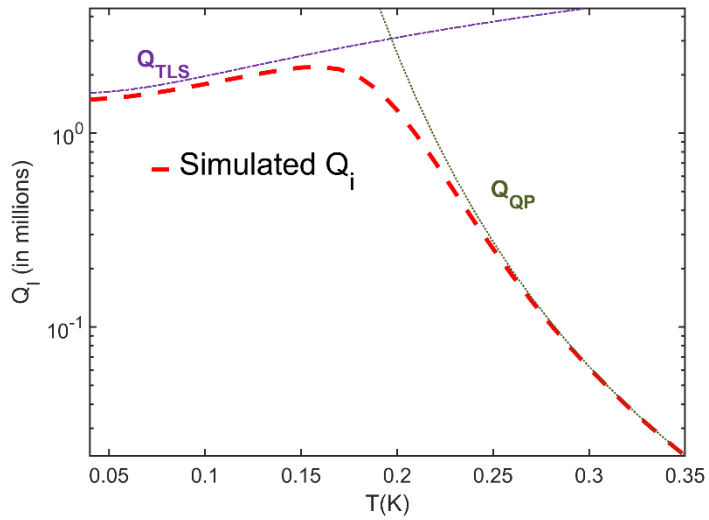


*Fig. 3.4: Simulated temperature dependence of a resonator loss dominated by TLS and quasiparticle losses.*

Similar effective temperature models for the non-equilibrium quasiparticle distribution have been previously reported in the literature[91], [94]. A significant difference between my proposed model and the previous work is the inclusion of a trapping term and my derivation of the complete relation starting from modified Rothwarf Taylor equations.

# Chapter 4 : Quasiparticle trap design and simulation

Various methods have been applied to reduce the quasiparticle density. These include adding shielding to reduce pair-breaking photons [1,2] and improving the components' thermalization to shield them from unwanted phonons[36]. Similarly, devices have been modified to include quasiparticle traps. The traps can be realized using non-superconducting regions such as vortices or normal metal or smaller bandgap superconducting traps. In resonators, the introduction of normal metal [32], [39], and vortices[38] as quasiparticle traps has been reported to improve device performance. In this chapter, I discuss the model to calculate the optimized design for a quasiparticle trapping layer for resonators.

## *4.1 Basic principle of Quasiparticle trap*

Quasiparticle traps can be formed from regions that host sub-bandgap states where quasiparticles can remain trapped. When in contact with the superconducting layer, the quasiparticles in the superconductor can diffuse into the trap layer. Ideally, the quasiparticles lose energy in the trap layer via phonon emission or electron-electron scattering and settle to lower energy states. Loss of energy reduces quasiparticles diffusion back into the primary superconductor, making the overlayer a quasiparticle trap.

Fig. 4.1 shows the schematic of the process. The energy diagram is plotted with the Fermi level as a reference. The band edge of the superconductor is at $\Delta_s$ above the Fermi level, while $\Delta_o$ is the base energy of the trap layer. $\Delta_o$ is zero for normal metals and positive for a superconducting trap layer. Similar to quasiparticles, Cooper pairs

from the adjacent superconductors also leak into the trap layer. Diffusion of Cooper pairs from a superconductor with a higher bandgap increases the trap layer bandgap and suppresses the superconductor bandgap at the interface. This phenomenon is called the proximity effect[106]. A device with trap layers needs to be designed accordingly to reduce any adverse effects of the proximity effect on the superconductor bandgap.

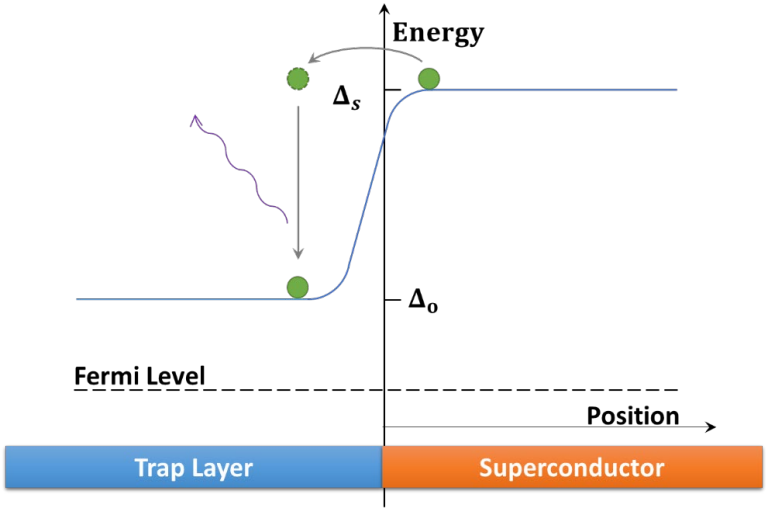


*Fig. 4.1: Schematic of quasiparticle trapping from primary superconductor to low gap superconductor*

## *4.2 CPW resonator design with traps*

In some of my resonators, I introduced a trapping layer on the top of a shorted quarter wavelength coplanar waveguide-based resonators, as shown in the cross-sectional schematic in Fig. 4.2. The trap overlayer has a setback distance, $s_b$, away from the edge of the ground plane of the coplanar waveguide. Also, the overlayer was absent from the central conductor of the resonator to avoid the high field interaction present on the central conductor. The absence of a trapping overlayer on the central conductor also ensures no bandgap modification of the primary superconductor in this region. The choice of this design means that the trapping only occurs in the ground plane and not

in the central conductor. A key parameter is the presence of an insulator layer between the trap layer and superconductor. This determines the interface transparency and affects the flow of quasiparticles between the superconductor and trap layer.

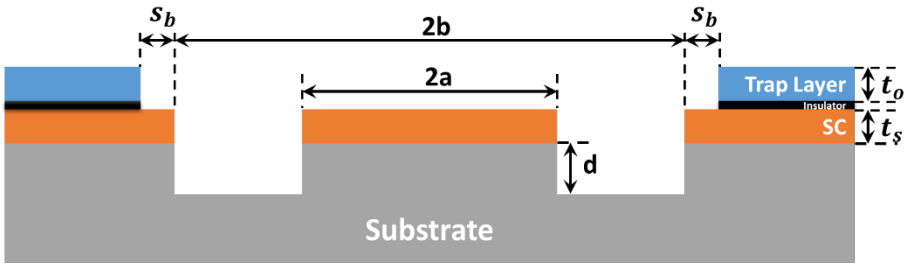


*Fig. 4.2: Schematic of the resonator design using small bandgap superconductors as a trapping layer*

## *4.3 Model*

In this section, I describe a model that expands a previous work on modeling a large area NIS electron refrigerator with a normal metal as a quasiparticle trap[107]. My model solves for excess quasiparticle number density, $n_{ex}$, in the superconductor, the effective electron temperature, $T_o$, in the trap layer and effective phonon temperature, $T_p$, of a combined system of phonons of superconductor and trap layer. My model solves for the above-mentioned device design to examine normal metal and low gap superconductor as overlayers. In the following section, I first describe individual components of the model and then present the complete model.

### 4.3.1 Quasiparticle trapping power

Power can flow between the superconductor layer and the overlayer. It can be calculated similarly to the tunneling current relation with zero bias[107]. In this model, I use an effective temperature $T_s$ to describe the quasiparticle population in the

superconductor while $T_o$ describes that of the overlayer. The power flow from superconductor to overlayer [108], [109] can be described by Eq. (4.1).

$$P_{\text{trap}} = A|T_{ST}|^2\big(2N_o(0)\big)\big(2N_s(0)\big) \times \int_{-\infty}^{\infty} E\rho_s(E)\rho_o(E)[f_s(E)(1-f_o(E)) - f_o(E)(1-f_s(E))]dE \tag{4.1}$$

$T_{ST}$ is the tunneling matrix element between superconductor to trapping layer determined by the insulating layer, and A is a proportionality constant. $N_o(0)$ and $N_s(0)$ are the single spin density of states of the respective metal layers. $\rho_o$ and $\rho_s$ are the normalized density of states. Modifying the integration limits and defining the normal state interface resistance $R_{trap} = \frac{1}{q_e^2 A|T_{ST}|^2(2N_o(0))(2N_s(0))}$ and simplifying Eq. (4.1) gives

$$P_{\text{trap}} = \frac{2}{q_e^2 R_{trap}} \int_{\Delta_s}^{\infty} E\rho_s(E)\rho_o(E)[f_S(E) - f_o(E)]dE \tag{4.2}$$

The above equation can be further simplified. In the primary superconductor, due to the high density of states at the band edge, the average quasiparticle energy can be approximated as $\Delta_s + k_B T_s$ . In a normal metal overlayer, I can take $\rho_o(E) = 1$ while for a superconducting overlayer $\rho_o(E) = \frac{E}{\sqrt{E^2 - \Delta_o^2}}$. For $E > \Delta_s$ and $\Delta_S \gg \Delta_o$, one finds that $\rho_o(E) \rightarrow 1$, e.g., for $\frac{\Delta_S}{\Delta_{S'}} = 4$, $\rho_o(\Delta_S) \sim 1.03$. Hence in both cases $\rho_o(E) \sim 1$. With the simplifying approximations, Eq. (4.2) becomes

$$P_{\text{trap}} \approx \frac{\Delta_s}{q_e^2 R_{trap}(2N_s(0))}\big(n(T_S) - n(T_o)\big) \tag{4.3}$$

Here $n(T_*)$ is the quasiparticle number density of the primary superconductor calculated at a temperature $T_*$. Notice that for $T_s > T_o$, quasiparticle power flows from the superconductor and trap layer and $P_{trap} > 0$.

### 4.3.2 Quasiparticle relaxation in trapping layer

If a quasiparticle with an average energy $\Delta_s$ tunnels into the overlayer, it carries average excess energy of $\mathrm{E}_t = \Delta_s - \Delta_o$. Quasiparticle that enters into overlayer may do one of three things: (a) tunnel back into the superconductor on a timescale $\tau_{tun}$, (b) relax to the energy $\Delta_o$ by scattering via another quasiparticle with an average lifetime $\tau_{e-e}(E_t)$, or (c) relax to the energy $\Delta_o$ by emitting a phonon with an average lifetime $\tau_{e-p}(E_t)$. The following equations give the probability of each event:

$$\Pi_{\mathrm{p}} = \frac{\tau_{e-p}^{-1}(E_t)}{\tau_{tun}^{-1} + \tau_{e-e}^{-1}(E_t) + \tau_{e-p}^{-1}(E_t)} \tag{4.4}$$

$$\Pi_{tun} = \frac{\tau_{tun}^{-1}}{\tau_{tun}^{-1} + \tau_{e-e}^{-1}(E_t) + \tau_{e-p}^{-1}(E_t)} \tag{4.5}$$

$$\Pi_{e} = \frac{\tau_{e-e}^{-1}(E_t)}{\tau_{tun}^{-1} + \tau_{e-e}^{-1}(E_t) + \tau_{e-p}^{-1}(E_t)} \tag{4.6}$$

The lifetimes governing individual processes are described below.

#### 4.3.2.1 Tunneling time

The tunneling lifetime is calculated from the tunneling current, and for a NIS junction, it is given as[108]

$$\tau_{tun} = 2N_s(0)q_e^2 t_s \mathcal{R}_{trap} \tag{4.7}$$

Here $\mathcal{R}_{trap}$ (script R) is a device-independent term that is a product of the area of the junction with the extrinsic trap resistance $R_{trap}$ (non-script R) of the interfacial tunnel barrier. Substituting $\mathcal{R}_{trap}$ into the Eq. (4.7) shows that $\tau_{tun}$ is inversely proportional to the density of states of overlayer, $N_o(0)$ and tunneling matrix element.

#### 4.3.2.2 Power flow between electrons and phonons

Quasiparticles in the overlayer can relax via electron-phonon interactions. In the presence of external energy and at low temperatures, there is a weak coupling between phonons and electrons, and this can cause them to be at different temperatures. In a normal metal, the power flow per unit volume from a thermal phonon system to a thermalized electron gas is given by [110], [111]

$$\mathcal{P}_{p-e,n} = \Sigma(\mathrm{T_p^n} - \mathrm{T_e^n}) \tag{4.8}$$

Where $T_e$ is the electron temperature, $T_p$ is the phonon temperature, Σ is the electron-phonon coupling constant, and n = 5 [107], [110].

#### 4.3.2.3 Electron-phonon interaction

In a normal metal overlayer, an electron with an energy $E_i$ can scatter (relax) to a lower energy state $E_f$ with an emission of a phonon (Ω). For a normal metal, at 0K, the electron-phonon scattering time of an electron with energy E can be written as [111]

$$\tau_{e-p}(E) \approx \frac{150(k_B)^5 N(0)}{\Sigma E^3} \tag{4.9}$$

Here $N(0)$ is the single spin density of states. Eq. (4.9) was calculated assuming a spherical Fermi surface and only longitudinal phonons contributing towards scattering. Actual metals have more complicated Fermi surfaces, but the assumption of a spherical Fermi surface simplifies the analysis of the electron-phonon interactions. At T= 0 K,

taking an average over all possible allowed phonons, an electron with energy $E_i$ would on average relax to energy $E_f = \frac{E_i}{4}$ with the emission of phonon with energy $\Omega = \frac{3}{4}E_i$[108], [111]. These results are valid at only for electron energy $E_i \gg k_B T$ [111].

For a superconducting overlayer, as shown in section 4.3.1, for quasiparticles with energy $E_i \gg \Delta_o$, I assume $\rho(E) \sim 1$ similar to that of a normal metal. I also assume that the electron-phonon scattering can be treated the same as in the normal state ($\tau_{e-p} \propto E_i^{-3}$) for high energy quasiparticles ($E_i \gg \Delta_o$). For quasiparticles near the band edge, I assume the electron-phonon scattering times are long[107], [111] and that diffusion dominates over scattering.

An emitted phonon with energy $\Omega = \frac{3}{4}E_i$ can interact with the overlayer and impact the electron temperature. In my model $E_i = E_t$. I discuss the absorption of the athermal phonons later. If the energy $E_f$ of a relaxed (quasiparticle) falls sufficiently below $\Delta_s$, it will not be able to tunnel back to the primary superconductor. Instead, it will further relax by transfer energy to overlayer electrons and phonons.

#### 4.3.2.4 Phonon-electron interaction:

In a normal metal overlayer, an electron with an energy $E_i$ can absorb a phonon with energy $\Omega$ and be excited to a higher energy state $E_f$. The phonon-electron scattering lifetime can be calculated from the ratio of phonon heat capacity and thermal conductance [107]:

$$\tau_{p-e} = \frac{234 \mathrm{N}_{ion} k_B^2}{5 \Sigma \Theta_D^3 E_i} \tag{4.10}$$

where $N_{ion}$ is the number density of atoms and $\Theta$ is the Debye temperature of the metal. At 0 K, taking an average of all possible states, the absorption of a phonon with energy $\Omega$ leads to the formation of two quasiparticles with energies equal to $\frac{\Omega}{2}$ [111].

In a superconductor (for both superconductor overlayer and primary superconductor), high energy phonons $\Omega > 2\Delta$ can break the Cooper pairs creating quasiparticles which I have discussed in section 2.2.2. I have assumed that low energy phonons with energy $\Omega < 2\Delta$ in the overlayer can excite the quasiparticles to higher energy states with a timescale $\tau_{p-e}$ described in Eq. (4.10) . On the other hand, repeated excitation of a quasiparticle can excite it to energy levels greater than $2\Delta$ and when they can relax back by generating phonons with energy $\Omega > 2\Delta$ which can again break cooper pairs or escape out of a film with the escape rate described in section 2.2.3. I have not included the repeated excitation of a single quasiparticle in my model.

The absorption of the athermal phonons depends on the $\tau_{p-e}$ and is described in section 4.3.3.2. In the model, for the overlayer, I have included athermal phonon $\Omega = \frac{3}{4}E_t$ due to relaxation of quasiparticle and phonon $\Omega = 2\Delta_s$ due to recombination from the primary superconductor. For the primary superconductor, only the absorption of phonon $\Omega = 2\Delta_s$ is included.

#### 4.3.2.5 The electron-electron scattering

In a normal metal, the electron-electron interaction depends on the dimensionality of the material(2D/3D) and disorder limits[107]. For my CPW resonators, the overlayer is in an effective 2D limit, i.e., the film is much thinner than

the e-e scattering mean free path. The electron-electron scattering time in a normal metal overlayer is

$$\tau_{e-e}(E) \cong \frac{2\pi\hbar^2 t}{q^2 \rho E \ln\left(\frac{T_1 k_b}{E_1}\right)}. \tag{4.11}$$

Here the Fermi temperature $T_1 \approx 10^{12}$ K, $t$ is the thickness of the film, and $\rho$ is the resistivity of the metal. Electron-electron scattering of an electron with energy $E \gg k_b T$, leads to a redistribution of energy to another electron, with the incident electron falling to an average final energy of $\frac{E}{3}$ and two new excitations (electron and a hole) of the same energy [107].

For a superconducting overlayer, I assume that the electron-phonon scattering rate for high energy quasiparticles, $E \gg \Delta_o$ to be the same as that of its normal metal counterpart. In my model, I took $\rho$ as the resistivity of the normal state at $T \geq T_c$ just above the superconducting transition. The recombination rate due to electron-electron interaction is a three-quasiparticle process and decreases exponentially with temperature as temperature decreases as $e^{-\frac{2\Delta(T)}{kT}}$ [48] and so it should be very rare at $T \ll T_c$.

### 4.3.3 Relaxation of phonon

#### 4.3.3.1 Acoustic mismatch of thermal phonons

The phonon flow between any two bulk materials that are in good contact is governed by the Kapitza resistance[112], which occurs due to differences in material properties. A first-order approximation that should work well for very thin layers is to assume no resistance between the overlayer and superconductor and that the phonons

can be represented by a single phonon temperature, $T_p$. In contrast, the substrate is assumed to be at bath temperature, $T_b$ and the thermal resistance between the superconductor and substrate phonons is included. For smooth interfaces, the Kapitza resistance can be determined by the acoustic mismatch between the materials [113]. For thermal phonons with $T \ll \theta_D$, the power flow per unit volume can be written as

$$\mathcal{P}_{\text{amm}} = \xi(T_p^4 - T_B^4) \tag{4.12}$$

where $\xi$ represents the thermal conductance of the thin film and substrate.

#### 4.3.3.2 Athermal Phonons

In my model, athermal phonons created during recombination and quasiparticle relaxation are assumed to undergo straight-line propagation, and the fraction of phonons absorbed by each layer is calculated. Phonons propagate with the speed of sound, $s$, of the material. The time to transit is assumed to be $t_{transit} = \frac{d_{layer}}{s\cos\varphi}$, where $d_{layer}$ is the thickness of the film, and $\varphi$ is the angle of incidence. The probability, $p_{scater}$, of the phonon scattering, an electron in a given layer is

$$p_{scater}(d_{layer}, E) = 1 - e^{\frac{-d_{layer}}{s\cos\varphi \times \tau_{p-e}(E)}} \tag{4.13}$$

On the other hand, the probability, $p_{abs}$, for the phonon generated by a trapped quasiparticle to go into the substrate is

$$p_{abs}(d_{layer}, E) = \eta\, e^{\frac{-d_{layer}}{s\cos\varphi \times \tau_{p-e}(E)}} \tag{4.14}$$

where $\eta$ is the phonon escape probability from the superconductor into the substrate. In my model, I assumed that the phonons also undergo specular reflections at the interface, and the process repeats until the phonon escapes. The total probability of

absorption is calculated by summing the probability the phonon travels through different layers for all possible initial position $z_i$ and angle of incidence $\varphi$. Summing all the possible probabilities for a phonon with energy $E$ of getting absorbed in a layer $L$ is tracked by the term $A_{E-L}$ .

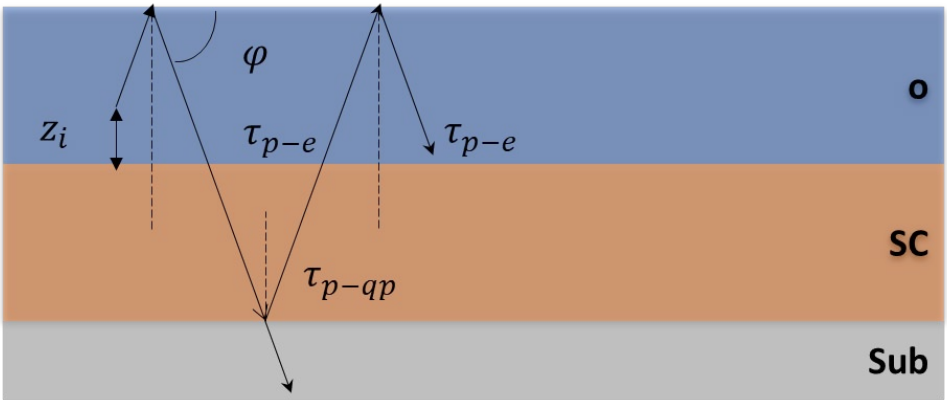


*Fig. 4.3: Reflection, absorption, and escape of high energy phonons*

### 4.3.4 Quasiparticle diffusion

The diffusion constant of electrons in a normal metal can be written as

$$D_N = \frac{1}{2q^2 N(0)\rho} = \frac{l v_f}{3}. \tag{4.15}$$

where $\rho$ is the resistivity, $l$ is the mean free path and $v_f$ is the Fermi velocity. For superconductors, the elastic mean free path of quasiparticles remains the same as that of electrons in the normal state, but the group velocity changes and becomes energy-dependent. This causes the diffusion constant to change. The energy-dependent group velocity is given as[111]

$$\mathrm{v_S}(E) \cong v_F \sqrt{1 - \left(\frac{\Delta}{E}\right)^2}. \tag{4.16}$$

The average quasiparticle velocity calculated over a thermal distribution including all energies is [107], [111]

$$\langle v_s(T_S)\rangle = \frac{2\mathrm{N}(0)}{\mathrm{n}(\mathrm{T_s})}\int_0^{\infty} \mathrm{v_S}(E)\, f_s(E)\rho(E)dE \approx\ v_F\sqrt{\frac{2k_BT_s}{\pi\Delta}}. \tag{4.17}$$

For thermal distributions, the diffusion constant of quasiparticles is then

$$\mathrm{D_S} = D_N\sqrt{\frac{2k_BT_s}{\pi\Delta}} \tag{4.18}$$

From the discussion, it is clear that $D_s$ will, in general, depend on the quasiparticle distribution.

### 4.3.5 Thermal conductivity of electrons

The thermal conductivity, $\kappa_{\mathrm{x}}$ of a clean normal metal at low temperatures is dominated by the electrons. The Wiedemann-Franz law provides a relation between $\kappa_x$ and the electrical resistivity $\rho_X$,

$$\kappa_{\mathrm{x}} = \frac{LT_X}{\rho_X} \tag{4.19}$$

where the Lorentz number, $L = 2.45 \times 10^{-8}\ W\Omega/K^2$. Although the Wiedemann-Franz relation fails at mid-range temperatures, it still is a good approximation for low temperatures[114]. For superconductors, the electronic specific heat capacity of decreases as $e - \frac{\Delta}{k_Bt}$ for the temperature at $T \ll T_C$ because Cooper pairs do not contribute to thermal conductivity, and only quasiparticles contribute to the conductivity.

### 4.3.6 Thermal conductivity of phonons

The specific heat capacity of a thermal distributed phonons at temperature $T \ll \Theta_D$ is given by[114]

$$\mathrm{C_p} = 234\left(\frac{T}{\Theta_D}\right)^3 N_{ion} \tag{4.20}$$

where $\Theta_D$ is the Debye temperature, and $N_{ion}$ is the atomic number density. The thermal conductivity can be written due to phonons is described as $\kappa_p = \frac{C_p l \langle s \rangle}{3}$. For my devices, I have assumed that the mean free path, $l$ , of the phonons is determined by the thickness of the films and therefore $l = (t_o + t_s)$ while $\langle s \rangle$ is the average speed of longitudinal phonons and is equal to the speed of sound in the film. The thermal conductivity can be rewritten as

$$\kappa_p = (t_o + t_s)\frac{\langle s \rangle}{3}\ 234\left(\frac{T}{\Theta_D}\right)^3 N_{ion} \tag{4.21}$$

Since the phonon density doesn't change in a superconductor transition, the thermal conductivity of the phonons is similar to that in the normal state.

## *4.4 The complete model*

A complete model of trapping in a CPW resonator model involves various processes occurring in the superconductor, trap layer, and phonon system and are as follows.

1. Pair-breaking photons/phonons or sub-gap microwave signals can generate the excess quasiparticles.
2. The excess quasiparticles density, $n_{ex}$, from superconductor with average energy $\Delta_S$ diffuse into the overlayer or recombine with each other.

3. A quasiparticle in the overlayer can either tunnel back or relax to the overlayer base state with a bandgap $\Delta_o$ through electron-electron or electro-phonon scattering.
4. The electrons in the normal metal overlayer transfer some of the excess energy to phonons via electron-phonon coupling.
5. Athermal phonons are generated by electron-phonon scattering $\frac{3E_t}{4}$ and quasiparticle recombination with energy $2\Delta_s$. The superconductor or overlayers absorb phonons via phonon scattering with some probability before they leave the films. Absorption depends on the band gap of the superconductor and overlayer.
6. Phonons in the overlayer and superconductor layers can exit to the substrate, where they transfer energy to the bath, which is at a temperature $T_b$.
7. Electrons, quasiparticles, and phonons diffuse within the films.

The overall particle flow in the coupled system is summarized in a block diagram in Fig. 4.4.

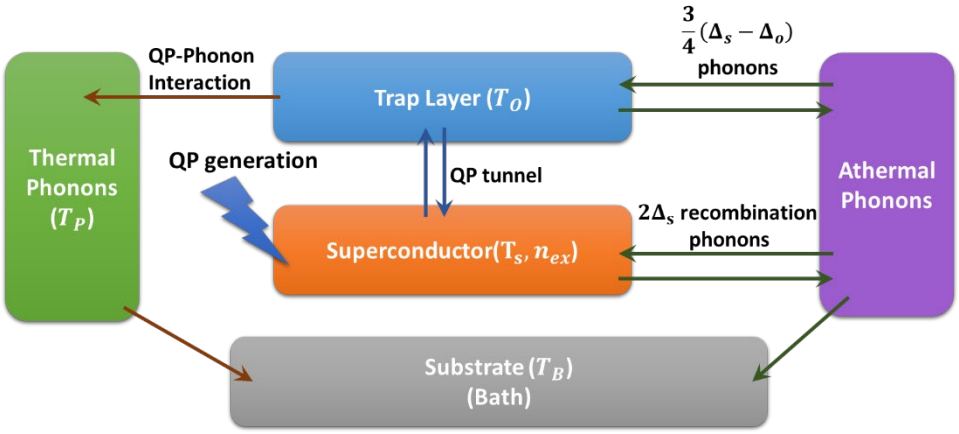


*Fig. 4.4: Block diagram representation of different systems interacting with each other*

I solved the model numerically to study the impact of a trap layer on the excess quasiparticle density in the superconductor and the impact of the trap setback, $s_b$ as shown in Fig. 4.5. To measure the impact of the setback, I assumed the quasiparticle injection from the edge of the ground plane with a profile similar to the power decay profile of CPW given as $P \propto |E|^2$ with an electric field defined in Eq. (2.26). This assumption helps to understand the impact of overlayer setback distance on the quasiparticle density near the ground plane edge but doesn't include the uniform generation of quasiparticles across superconductor. The electron in the overlayer is tracked by the electron temperature, $T_o$. The quasiparticles in the superconductor are tracked by the excess quasiparticle density, $n_{ex}$, which is set by the effective quasiparticle temperature, $T_S$. The thermal phonons are tracked by the phonon temperature, $T_p$. The temperature and the quasiparticle number density were assumed to be constant across the film thickness of the superconducting layers. This is a very good approximation because the thickness of my resonators was 1-2 orders of magnitude smaller than recombination or trapping distance.

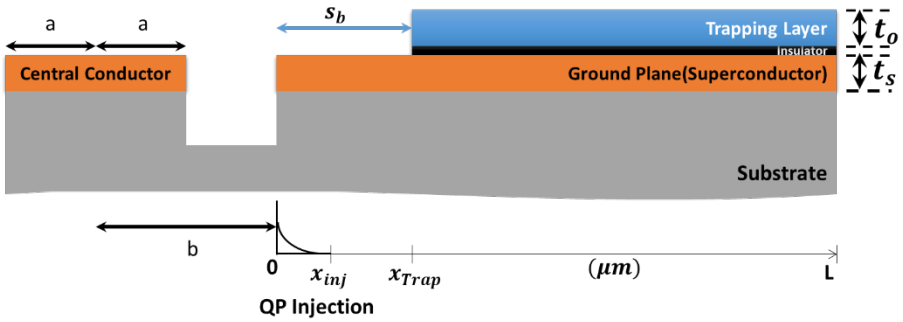


*Fig. 4.5: Schematic of a cross-section of CPW. 's' is the setback distance of small gap superconductor from the edge of the ground plane edge. The injection of the quasiparticle is assumed to be from the edge of the ground plane.*

The behavior of the normal metal trap electron temperature, $T_o$ was found by solving the following diffusion equation [107]:

$$\{t_o \kappa_o \frac{d^2 T_o}{dx^2} + \left(\Pi_e + \frac{\Pi_p}{4} + \frac{3\Pi_p}{4} A_{\frac{3E_t}{4}-O}\right)\mathcal{P}_{trap} - t_o \mathcal{P}_{p-e} \quad (4.22)$$

$$+ A_{2\Delta_s - O} t_s R_{qp} (n_{ex}^2 + 2 n_{ex} n_{th}) \Delta_s \} \left(\Theta\left(x - x_{Trap}\right)\right) = 0.$$

The first term accounts for the diffusion of the electron temperature along $x$. The second term accounts for the heating of the overlayer electrons due to power transferred from quasiparticles from the superconductor. The third term describes the emission of phonons by electrons, and the last term describes the absorption of the athermal phonons from the recombination of excess quasiparticles. Here, $t_o$ is the thicknesses of the overlayer $\kappa_o$ is thermal conductivity. The terms $\Pi_i$ factors are the ratios of the electron relaxation of various modes (electron-electron, electron-phonon, tunneling). The probability of absorption of athermal phonons with energy 'E' in layer 'L' is described by the term $A_{E-L}$. $\mathcal{P}_{trap}$ is the quasiparticle trapping power per unit area which was defined in Eq. (4.3) . $\mathcal{P}_{p-e}$ is the power flow per unit volume between phonon and electron which is defined in Eq. (4.8). Also, $t_s$ is the thickness of the superconducting layer, $R_{qp}$ is the recombination rate, $n_{th}$ is the thermal quasiparticle density and $\Delta_s$ is the gap of the superconductor. The Heaviside step function $\Theta$ sets the location of the overlayer to $x > x_{trap}$ as a function of distance, $x$ from the inner edge of the CPW ground plane (see Fig. 4.5).

The quasiparticle number density, $n_{ex}$ in the superconducting layer was assumed to obey the following equation

$$t_s D_{qp} \frac{d^2 n_{ex}}{dx^2} + g_{inj}(x)\Gamma_{inj} - \left(\Theta\left(x - x_{Trap}\right)\right)\frac{(1 - \Pi_{tun})}{\Delta_s}\mathcal{P}_{trap} - \left(1 - A_{2\Delta_s - s}\right)t_s R_{qp}(n_{ex}^2 + 2n_{ex}n_{th}) = 0. \quad (4.23)$$

The first term describes the diffusion of quasiparticles. The second term describes the quasiparticle injection, which creates excess quasiparticles in the superconductor film. The third term describes the trapping of quasiparticles due to overlayer, and the last term describes the loss of quasiparticles due to recombination. Here $D_{qp}$ is the diffusion constant of the quasiparticles in the primary superconductor. $g_{inj}(x)$ describes the injection profile for quasiparticles while $\Gamma_{inj}$ is the injection rate of quasiparticles.

The phonon temperature $T_p$ was obtained by solving the following diffusion equation.

$$(t_s + t_o)\kappa_P \frac{d^2 T_p}{dx^2} + \Theta\left(x - x_{Trap}\right)\mathrm{t_o}\mathcal{P}_{p-e} - \mathcal{P}_{amm} = 0. \quad (4.24)$$

The first term describes the diffusion of phonons, and the second term describes the exchange of energy with the overlayer, and the third term describes the phonon escape to the substrate. Here $\kappa_p$ is the phonon thermal conductivity and $\mathcal{P}_{amm}$ is the power flow per unit area from phonon system to substrate phonons and is defined in Eq. (4.12).

## *4.5 Numerical Solution*

I solved the equations (4.22), (4.23), and (4.24) numerically for boundary conditions $\frac{dT_p}{dx} = 0, \frac{dT_p}{dx} = 0$ and $\frac{dn_{ex}}{dx} = 0$ at $x = 0$ and $x = L$. The total length L was discretized into N-1 steps with step size of 500 nm. The Eq. (4.23) and (4.24) were discretized into N equations and Eq. (4.22) into $N'$ steps in the region that defined the

trap layer. The equations were solved using a multivariate Newton-Raphson method. The variables are given by

$$\begin{aligned} \mathbf{z_{T_o}} &= \left[\mathrm{T_{O_1}},\ \ldots.\ ,\ \mathrm{T_{O_N}},\right]^{\mathrm{T}} \\ \mathbf{z_{n_{ex}}} &= \left[\mathrm{n_{ex_1}},\ \ldots.\ ,\ \mathrm{n_{ex_N}}\right]^{\mathrm{T}} \\ \mathbf{z_{T_p}} &= \left[\mathrm{T_{p_1}},\ \ldots.\ ,\ \mathrm{T_{p_N}}\right]^{\mathrm{T}} \\ \mathbf{z} &= \left[\mathbf{z_{T_o}}; \mathbf{z_{n_{ex}}}; \mathbf{z_{T_p}}\right] \end{aligned} \tag{4.25}$$

The Eq. (4.23) describing the electron temperature in the overlayer was discretized and rearranged, and described by the function $f_{T_{o_i}}$

$$\begin{aligned} & f_{T_{o_i}}\left(T_{o_{i-1}}, T_{o_i}, T_{o_{i+1}}, T_{p_i}, T_{S_i}, n_{ex_i},\ x_i\right) = \\ & \Theta\left(x_i - x_{trap}\right) \times \left(T_{O_{i+1}} - 2T_{O_i} + T_{O_{i-1}}\right) \\ & +\Theta\left(x_i - x_{trap}\right)\left(\frac{\Delta x^2}{\kappa_o t_o}\right) \times \left(\Pi_e + \frac{\Pi_p}{4} + \frac{3\Pi_p}{4} A_{\frac{3\Delta}{4}-O}\right) \\ & \qquad \times \frac{\Delta}{q_e^2 \mathcal{R}_{trap} N(0)}\ \left(n_{ex_i} - n\left(T_{o_i}\right)\right) \\ & -\Theta\left(x_i - x_{trap}\right)\left(\frac{\Delta x^2}{\kappa_o t_o}\right) \times\ t_o \Sigma\left(T_{p_i}^5\ - T_{o_i}^5\right) \\ & +\Theta\left(x_i - x_{trap}\right)\left(\frac{\Delta x^2}{\kappa_o t_o}\right) \times A_{2\Delta-O} t_s \Gamma_R \left(n_{ex_i}^2 + 2 n_{ex_i} n_{th}\right)\Delta \end{aligned} \tag{4.26}$$

Similarly, Eq. (4.24) describing the excess quasiparticle distribution in the superconductor was discretized and given as follows:

$$
\begin{aligned}
&f_{n_{ex_i}}\left(n_{ex_{i-1}}, n_{ex_i}, n_{ex_{i+1}}, T_{S_i}, T_{o_i},\ x_i\right) = \left(n_{ex_{i+1}}\ - 2n_{ex_i} + n_{ex_{i-1}}\right) \\
&+\left(\frac{\Delta x^2}{t_s D_{QP}}\right) g_{inj}(x_i)\ \Gamma_{inj} \\
&-\left(\frac{\Delta x^2}{t_s D_{QP}}\right) \Theta\left(x_i - x_{trap}\right) \frac{(1-\Pi_{tun})}{\Delta_s} \frac{\Delta_s}{q_e^2 \mathcal{R}_{trap} N(0)}\ \left[n_{ex_i} - n\left(T_{o_i}\right)\right] \\
&-\left(\frac{\Delta x^2}{t_s D_{QP}}\right) \left(1 - A_{2\Delta_s - s}\right) t_s \Gamma_R \left(n_{ex_i}^2 + 2n_{ex_i} n_{th}\right)
\end{aligned}
\tag{4.27}
$$

The Eq. (4.25) describing the phonon interaction was discretized and given as follows:

$$
\begin{aligned}
&f_{T_{p_i}}\left(T_{P_{i-1}},\ T_{P_i},\ T_{P_{i+1}},\ T_{S_i}, T_{o_i},\ n_{ex_i}\ , x_i\right) = \left(T_{p_{i+1}} - 2T_{p_i} + T_{p_{i-1}}\right) \\
&+\left(\frac{\Delta x^2}{(t_s + t_o)\kappa_p}\right) \Theta\left(x_i - x_{trap}\right)\ t_o \Sigma\ \left(T_{p_i}^5\ - T_{o_i}^5\right) \\
&-\left(\frac{\Delta x^2}{(t_s + t_o)\kappa_p}\right) \xi\left(T_{P_i}^4 - T_B^4\right)
\end{aligned}
\tag{4.28}
$$

This gave $2N + N'$ equations which I grouped together in a single vector $\mathbf{f}(\mathbf{z}) = \begin{bmatrix} f_{T_{o_i}}(\mathrm{z_{T_o}}) \\ f_{n_{ex_i}}(\mathbf{z_{n_{ex}}}) \\ f_{T_{p_i}}(\mathbf{z_{T_{p_i}}}) \end{bmatrix}$ and recursively solved to find the solution $\mathbf{f}(\mathbf{z}) = 0$. Starting with a from startpoint $\boldsymbol{z_o}$, the next guess for the iteration was obtained by solving $\mathbf{f}(\boldsymbol{z} + \delta \boldsymbol{z}) = \mathbf{f}(\boldsymbol{z}) + \mathcal{J}_f(\boldsymbol{z})\boldsymbol{\delta z} = \mathbf{0}$, which gives

$$
\boldsymbol{\delta z} = \ -\mathbf{f}(\boldsymbol{z})\mathcal{J}_f^{-1}(\boldsymbol{z}) \tag{4.29}
$$

Here $\boldsymbol{\delta z} = \begin{bmatrix} \mathbf{\delta z_{T_o}} \\ \mathbf{\delta z_{n_{ex}}} \\ \mathbf{\delta z_{T_p}} \end{bmatrix}$ and the Jacobian $\mathcal{J}_f(\boldsymbol{z}) = \begin{bmatrix} \mathbf{J_{11}} & \mathbf{J_{12}} & \mathbf{J_{13}} \\ \mathbf{J_{21}} & \mathbf{J_{22}} & \mathbf{J_{23}} \\ \mathbf{J_{31}} & \mathbf{J_{32}} & \mathbf{J_{33}} \end{bmatrix}$.

$$
\mathrm{J_{11}} = \left[\frac{\partial \mathrm{f_{T_{o_i}}}}{\partial \mathrm{T_{o_i}}}\right]_{\mathrm{N' \times N'}} \quad \mathrm{J_{12}} = \left[\frac{\partial \mathrm{f_{T_{o_i}}}}{\partial \mathrm{n_{ex_i}}}\right]_{\mathrm{N' \times N}} \quad \mathrm{J_{13}} = \left[\frac{\partial \mathrm{f_{T_{o_i}}}}{\partial \mathrm{T_{p_i}}}\right]_{\mathrm{N' \times N}} \tag{4.30}
$$

$$J_{21} = \left[\frac{\partial f_{n_{ex_i}}}{\partial T_{o_i}}\right]_{N\times N'} \quad J_{22} = \left[\frac{\partial f_{n_{ex_i}}}{\partial n_{ex_i}}\right]_{N\times N} \quad J_{23} = \left[\frac{\partial f_{n_{ex_i}}}{\partial T_{p_i}}\right]_{N\times N}$$
$$J_{31} = \left[\frac{\partial f_{T_{p_i}}}{\partial T_{o_i}}\right]_{N\times N'} \quad J_{32} = \left[\frac{\partial f_{T_{p_i}}}{\partial n_{ex_i}}\right]_{N\times N} \quad J_{13} = \left[\frac{\partial f_{T_{p_i}}}{\partial T_{p_i}}\right]_{N\times N}$$

The process was repeated until output converged to a solution.

## *4.6 Simulation results*

I solved the model equations for titanium nitride as a superconductor and aluminum as the overlayer. The thickness and resistance values determined from measured quantities and other constants are calculated from the above-mentioned standard relations. For calculations, aluminum is treated as normal metal, and some of the values which are difficult to calculate are taken from the ref [107], especially the junction parameters. I have chosen an arbitrary injection rate at x=0 which is proportional to the ratio of average photon energy in the resonator by the bandgap of the superconductor. All the rest of the values used for the calculations are summarized in the tables below.

*Table 4-1: Input values for the TiN resonator with Al overlayer*

| **Parameter** | **Input Value** | **Description** |
|---|---|---|
| Primary SC | TiN | |
| Overlayer | Al | |
| $\mathcal{R}_{trap}$ | 60 Ω/μm$^2$ | Resistance Area product of overlayer traps[107] |
| $t_o$ | 100 nm | Thickness of Overlayer film |
| $t_s$ | 100 nm | Thickness of Overlayer superconductor |
| $T_b$ | 100 mK | Bath Temperature |
| $E_t$ | 622 $\mu eV$ | Excess QP energy from TiN to Al |

*Table 4-2: Input parameter values for aluminum*

| Parameter | Input Value | Description |
|---|---|---|
| $T_C$ | 1.2 K | Measured $T_C$ |
| $N(0)$ | $1.16\times10^{10}$ eV$^{-1}$ µm$^{-3}$ | Single spin density of states[107] |
| $\rho_{s-Normal}$ | $3.63\times10^{-7}$ Ω-cm | Measured resistivity near $T_C$ |
| $\Theta_D$ | 433 K | Debye Temperature |
| $\Sigma$ | 2.3 nW/(µm$^3$K$^3$) | Electron Phonon coupling[107] |
| $\langle s \rangle$ | $4.4\times10^9$ µm/s | Average phonon speed in Al[107] |
| $\xi$ | 483 pW/(K$^4$-µm$^2$) | Acoustic Mismatch coefficient [115], [116] |
| $A_{\frac{3}{4}E_t-o}$ | 0.86 | Phonon Absorption Probability [107] |
| $A_{2\Delta_S-o}$ | 0.33 | Phonon Absorption Probability [107] |
| $A_{2\Delta_S-s}$ | 0.38 | Phonon Absorption Probability [107] |
| | | |
| **Parameter** | **Calculated Value** | |
| $\Delta_o$ | 182 µeV | Eq. (2.2) |
| $D_{s-normal}$ | 742 cm$^2$/s | Eq. (4.15) @ $T_c$ |
| $D_{s-qp}$ | 128 cm$^2$/s | Eq. (4.18) @ $T_s$ = 0.1 K |
| $\kappa_p$ | $7.02\times10^{-13}$ W/(K-µm) | Eq. (4.21) |
| | | |
| $\kappa_o$ | $6.74\times10^{-7}$ W/(K-µm) | Eq. (4.19) |
| $\tau_{p-e}(2\Delta_s)$ | 13.8 ps | Eq. (4.10) |
| $\tau_{p-e}\left(\frac{3}{4}E_t\right)$ | 36 ps | Eq. (4.10) |
| $\tau_{e-p}(E_t)$ | 2.28 ns | Eq. (4.9) |
| $\tau_{e-e}(E_t)$ | 29.4 ns | Eq. (4.11) |
| $\tau_{tun}$ | 56.8 ns | Eq. (4.7) |
| $\Pi_p$ | 0.895 | Eq. (4.4) |
| $\Pi_{tun}$ | 0.035 | Eq. (4.5) |
| $\Pi_e$ | 0.070 | Eq. (4.6) |

*Table 4-3: Input parameter values for Titanium nitride*

| Parameter | Input Value | Description |
|---|---|---|
| $T_C$ | 5.3 K | Measured $T_C$ |
| $R_{qp}$ | 100 µm$^3$/s | Recombination Constant[117] |
| $\tau_{qp}$ | 15 µs | Quasiparticle lifetime[118] |
| $N(0)$ | 2.96×10$^{10}$ eV$^{-1}$ µm$^{-3}$ | Single spin density of states[119] |
| $\rho_{s-Normal}$ | 1.65×10$^{-5}$ Ω-cm | Measured resistivity near $T_C$ |
| $\Theta_D$ | 579 K | Debye Temperature |
| $D_{s-normal}$ | 1.1 cm$^2$/s | Normal state diffusion constant |
| | | |
| **Parameter** | **Calculated Value** | |
| $D_{s-qp}$ | 0.09 cm$^2$/s | Eq. (4.18) @ $T_s$ = 0.1K |
| $\Delta_s$ | 804 µeV | Eq. (2.2) |

### 4.6.1 Impact of setback distance $s_b$

I performed a simulation to measure the variation in the quasiparticle density as a function of the setback distance for a given quasiparticle injection. Fig. 4.6 shows the result of the simulated quasiparticle density from the CPW ground plane.

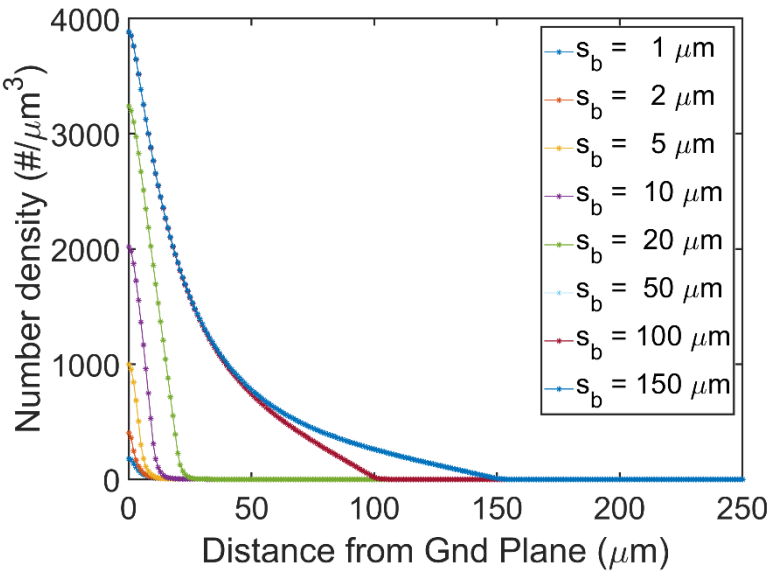


*Fig. 4.6: Simulation results of the quasiparticle number density vs. distance from the ground plane for quasiparticle trap resonators with different setback values.*

The simulation results in Fig. 4.6 show, lowering of quasiparticles near the ground plane edge ($x$~0). As the setback distance $s_b$ of the normal metal overlayer increased, the density saturated at $x = 0$ saturated for $s_b$ = 100 µm. Note however, there was a decrease in the integrated density (area under the curves) for all setbacks less than $s_b = 150\ \mu m$. Thus smaller setbacks were preferred.

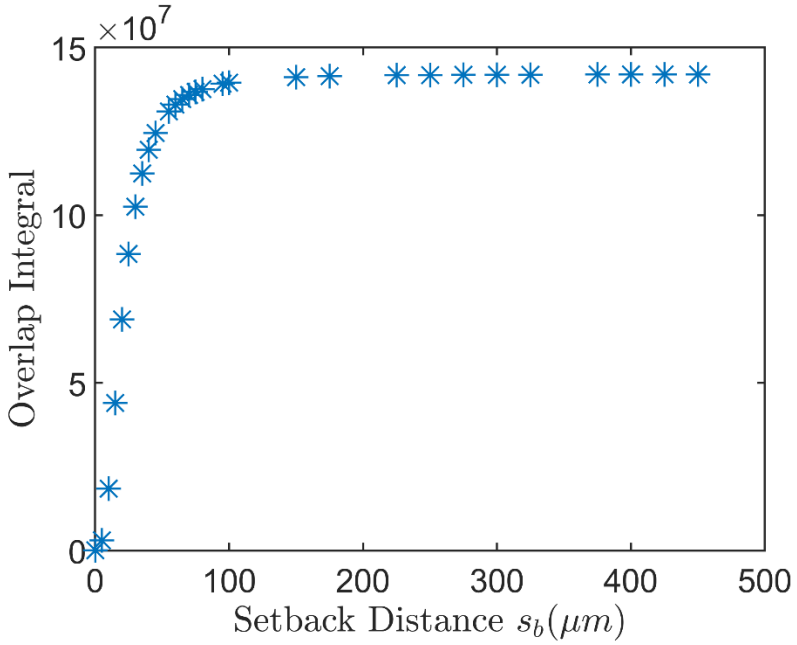


*Fig. 4.7: Overlap Integral of the electric field and quasiparticle number density in the superconductor versus setback distances $s_b$ calculated at $T_b$ = 0.1K and $\mathcal{R}_{trap}$ = 60 Ω µm².*

I used an overlap integral of the electric field in the superconductor and the quasiparticle number density to estimate the relative effectiveness of the trapping layer for various setback distances:

$$\mathrm{I}_{\mathrm{overlap}} = \frac{\left|\int E \times n_{qp} dx\right|^2}{\int |E|^2 dx} \tag{4.31}$$

For a simple calculation, I used the electric field present in the resonator ground plane without any overlayer, as described by Eq. (2.26). Fig. 4.7 shows the result of variation

in overlap integral with setback distances. There is a decrease in the overlap value for setback distances $s_b < 100$ μm suggesting that the quasiparticle number density in the superconducting film decreases with setback distance. However, I note that this calculation does not include the loss from accumulating electrons or quasiparticles in the trapping layer, so the actual Q vs. setback may have a different dependence on $s_b$.

### 4.6.2 Impact of interface

The quality of the interface between the overlayer and superconducting layer affects the flow of quasiparticles and impacts the trapping effectiveness. The key parameter is the interface resistance $\mathcal{R}_{trap}$ reflects the change in the interface quality.

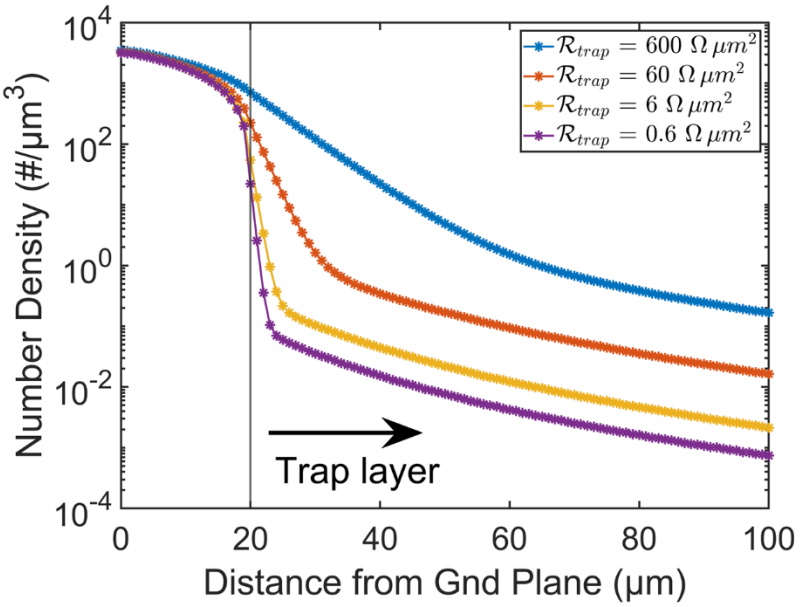


*Fig. 4.8: Variation of quasiparticle number density with variation in $\mathcal{R}_{trap}$ for $x_{trap} = 20\mu m$.*

Fig. 4.8 shows a plot of the quasiparticle density for different interface resistance. Examining the plot, we see that for $\mathcal{R}_{trap}$ between 0.6 Ωμm$^2$ and 600 Ωμm$^2$, there is no change in the quasiparticle at the ground edge, but quasiparticle density decreases

significantly underneath the trap layer. This graph suggests that the contact resistance of the overlayer with a small or non-existing tunneling layer may result in better trapping effectiveness.

## *4.7 The transition from normal metal overlayer to superconductor*

A theoretical study by Riwar et al. [42] of small gap superconductors as traps claimed an improved trapping efficiency over normal metal counterparts. For a superconductor with a normal metal trap, a high density of states in the primary superconductor led to a high backflow into the normal metal traps. While for a superconductor trap, the presence of a similar high density of states eliminates the backflow. Another significant difference is the suppression of thermal conductivity in the superconducting overlayer, as discussed in section 4.3.5. Additionally, superconductor traps should contribute low ohmic loss in the high electric field region compared to the normal metal layer, but accumulated quasiparticles will still contribute loss.

## *4.8 Impact on resonator quality factor*

The relationship between quasiparticle number density and resonator quality factor is complicated. In my quality factor calculation, I assume that the ground plane and the central conductor have the same effective quasiparticle temperature. However, the resonators with trap layers on the ground plane modify the quasiparticle distribution only in the ground plane, giving two different temperatures for the ground plane and central conductor. The contribution to the loss from the ground plane and the central conductor depends on the device geometry. In principle, it can be estimated using

conformal mapping techniques. Using these geometric factors $g_{ctr}$ and $g_{gnd}$ for a coplanar waveguide similar to Eq. (2.36), the net quality factor can be approximated as $\frac{1}{Q_{QP}} \propto g_{ctr} \times n_{cc} + g_{gnd} \times n_{gnd}$.

# Chapter 5 : Experimental methods

I fabricated CPW resonators with quasiparticle traps from the MBE-grown titanium nitride and aluminum bilayers. I also fabricated aluminum resonators and titanium nitride resonators for comparison. In this chapter, I provide details on the resonator design and fabrication as well as the measurement processes.

## *5.1 Thin-film growth*

All of the films I used were grown and characterized by Dr. Richardson. All the films were grown on a 3-inch highly resistive (sheet resistance > 5kΩ-cm) float zone refined silicon (111) wafer in a plasma-assisted molecular beam epitaxy (MBE) system with a base pressure less than $10^{-10}$ mbar at LPS. High resistive wafers ensured a high-impedance path for the microwave signals through the substrate and had a low oxygen impurity concentration which is necessary to achieve low-loss superconducting circuits.

The silicon wafer was first ex-situ degreased by a solvent series of acetone, methanol, and isopropyl alcohol to remove organic surface contaminants. Next, the wafer was sequentially etched with 5% HF and 40% $NH_4F$ to remove the native surface oxide and obtain step edges on Si(111) plane. Then the wafer was in-situ thermally treated in the UHV MBE chamber sequentially at 200℃ and 800℃ to remove moisture, hydrogen, fluorine, and residual oxide from the silicon surface.

For the aluminum-titanium nitride bilayer, the 100-nm thick titanium nitride film was grown using the near-simultaneous introduction of titanium and nitrogen flux with a growth temperature of 750℃. The substrate was cooled to 100℃, and a 100-nm-thick

aluminum layer was grown on top [120], [121]. Sequential growth of titanium nitride and aluminum without exposure to the atmosphere helped to ensure a good metal to metal junction ($S_1S_2$) without an insulating layer between them.

After deposition, I characterized the material and electrical properties of the films. The film's surface was investigated using atomic force microscopy (AFM). The AFM showed a smooth surface with peak-to-peak roughness less than 20 nm with an overall RMS roughness of 3.5 nm, as shown in Fig. 5.1.

I also measured the thickness of the films using the cross-sectional SEM. The corresponding SEM image is shown in Fig. 5.2. The layers of aluminum, titanium nitride and silicon are clear and indicate no obvious intermixing of layers. Aluminum with the highest conductivity is the brightest of the three. The thickness measurement gave a 96 nm thickness for titanium nitride and 101 nm for the aluminum films.

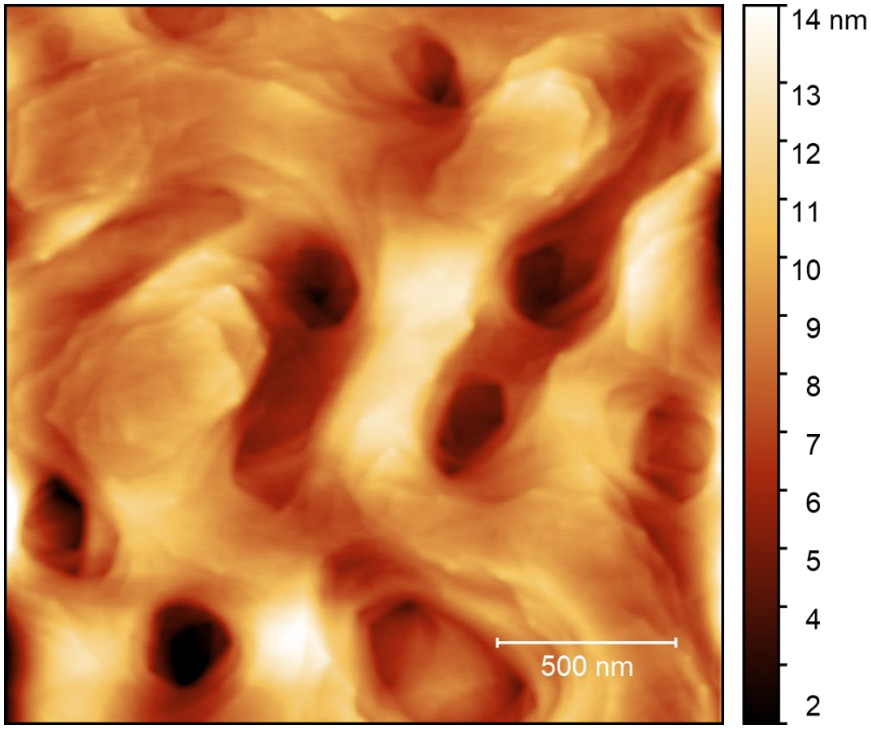


*Fig. 5.1: AFM image of Al on TiN*

The cross-sectional SEM and measured peak-to-peak roughness by AFM show the continuity of the films. The lateral correlation length of the surface roughness of the films is lower than the coherence lengths of both TiN[122] and Al[123], which suggests the supercurrent will not be affected. There is a possibility that variations in the microstructure and local composition variations may create nanometer scale variations in $T_C$[124], which may create energetically favorable sites for quasiparticle trapping. Additionally, the growth of both layers of this heterostructure in a single MBE system helps prevent interface defects that may contribute to TLS loss. Neither of these local affects are included in the model explicitly.

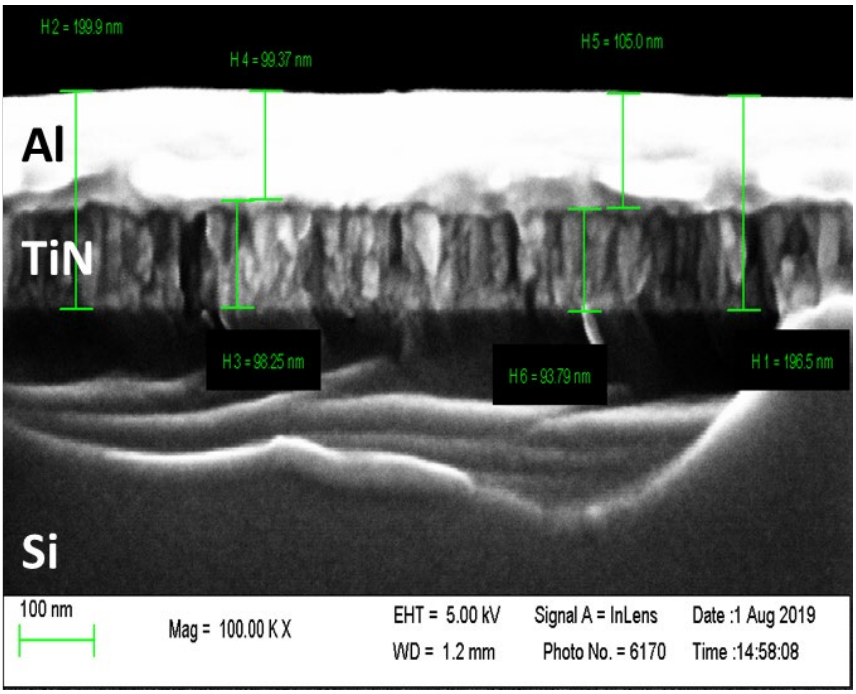


*Fig. 5.2: Cross-sectional SEM of Al-TiN layers*

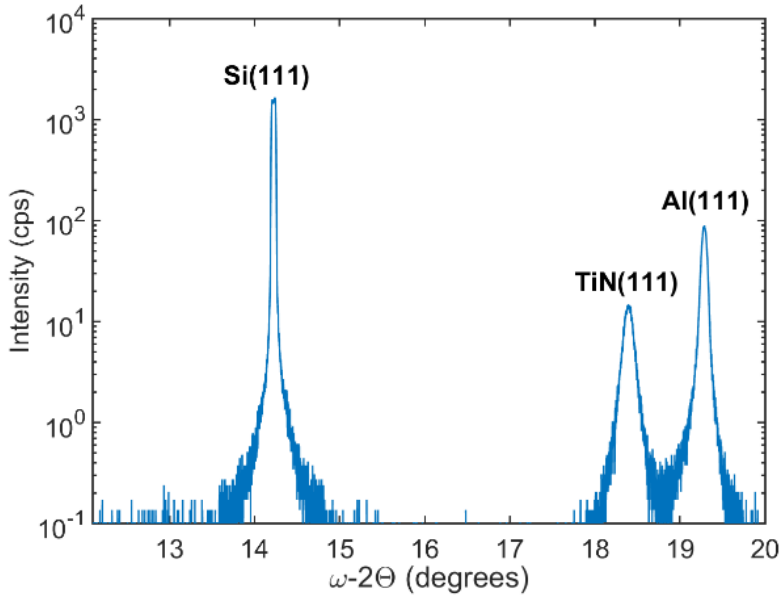


*Fig. 5.3* Symmetric X-ray diffraction of a bilayer of TiN-Al. Data indicates relaxed Al and TiN layers

Next, symmetric x-ray diffraction was performed to investigate the crystallographic structure. The diffraction pattern shows distinct peaks corresponding to Si (111) at 14.2°, TiN (111) at 18.4°, and Al (111) at 19.3°, as shown in Fig. 5.3. The Al and TiN peaks correspond to the expected crystal peak, implying relaxed aluminum and titanium nitride layers without any thin interfacial reaction of the elements or alloy formation.

To build the reference titanium nitride resonators, I selected a die from the Al-TiN bilayer wafer and etched off the aluminum using an aluminum etchant. The aluminum etchant does not etch the titanium nitride film. This ensures the use of the same crystal quality titanium nitride for comparison.

Additionally, 100-nm-thick aluminum films were grown on a separate 3-inch float zone refined silicon (111) wafer by Dr. Richardson. First, the silicon wafer was treated with standard ex-situ and in-situ processes. The silicon surface was exposed to a nitrogen flux for 15 min before aluminum deposition at the substrate temperature of

100℃. Symmetric x-ray diffraction showed the presence of a relaxed aluminum film on silicon.

All three films were measured for their respective critical temperatures. The measurements were made on 5 mm × 10 mm chips from each set with Kelvin probes mounted in a delta mode measurement system in an adiabatic demagnetization refrigerator (ADR). The temperature variation of resistance is shown in Fig. 5.4.

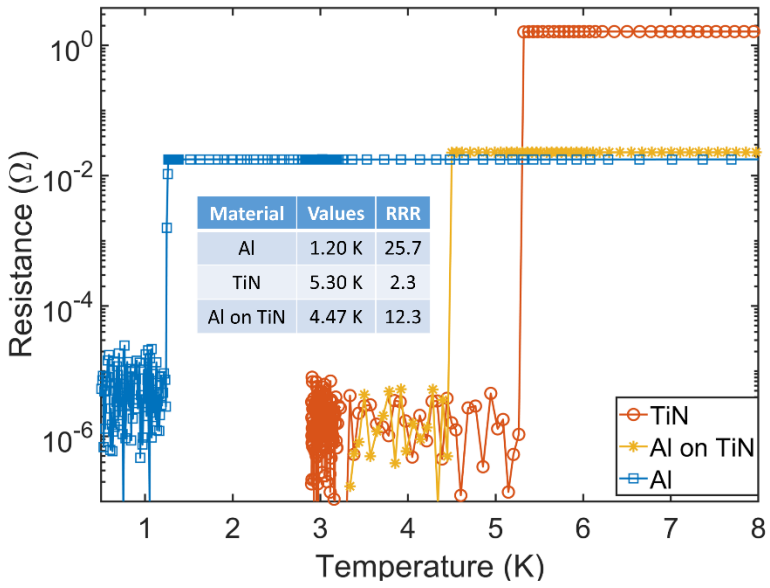


*Fig. 5.4:* DC measurements of resistance of Al-TiN bilayer, TiN layer, and Al layer vs. temperature. The $T_c$ and RRR of the films are shown in the inset.

The critical temperature ($T_C$) for the titanium nitride was 5.3 K, aluminum-titanium nitride bilayer at 4.47 K, and bare aluminum at 1.2 K. Since the $T_C$ of Al-TiN bilayer (4.47 K) is higher than bare aluminum film (1.2 K) and lower than the single layer of TiN, it suggests the aluminum layer may be proximitized by the titanium nitride beneath it, consistent with relatively good contact between the layers. [125], [126]. The corresponding residual resistance ratio, RRR for Al, was 25.7, TiN was 2.3, and Al-TiN bilayer was 12.3.

## *5.2 Mask Design*

The resonators with quasiparticle traps require a two-step optical lithography process, as shown in Fig. 5.9. The first mask was used to define the feature with the size of the resonator (w+2g) plus twice of setback ($s_b$) for the eventual resonator features defined by the second mask. The first mask was named 'Overlayer mask,' and the second was named 'Resonator mask.' Both masks were divided into four quadrants, with each quadrant having a unique set of setback combinations which gives the option of obtaining 4 dies in a single fabrication process. Each quadrant corresponds to a 6 mm × 6 mm chip. The primary features of the 'Resonator masks' were:

- Resonators have one end shorted quarter-wavelength CPW waveguide with a frequency ranging from 4-6 GHz.
- Each quadrant had frequency multiplexed resonators that are capacitively coupled with a single feed line. Multiplexing allows multiple resonator measurements from a single chip in a single measurement cycle.
- Each resonator had a central conductor width of w=16 μm and g = 8 μm while the feed line had a central conductor width of 31 μm and a gap of 14 μm.
- To avoid crosstalk, the minimum spectral spacing between the resonator frequencies is $f_o/Q$[127]. For a resonator with a resonance frequency of 5 GHz and a quality factor of $10^5$-$10^6$, the minimum required spacing was 50 kHz. In the mask design, a frequency spacing of 180 MHz was chosen to minimize the crosstalks.
- The resonators were designed for substrates with a dielectric constant $\epsilon$ = 10, similar to silicon and sapphire. The resonator length ranges from 7.1 mm to 4.2

mm for the given frequency range and dielectric constant. The resonators were designed in a serpentine manner to optimize the chip area better. Each resonator is designed with 3 straight sections and two 180-degree turns with radius vary depending on the setback.

- Each straight section of a resonator was spatially separated by a distance of seven times greater than the width (w+2g) of the resonator to reduce parasitic coupling between the arms.
- The ground plane was perforated with holes to provide locations for vortices to be trapped far from the resonator.

The primary features of the 'Overlayer masks' were:

- The overlayer mask had slots tracking the resonator features with variable setback distances. The setback distances varied between 1 μm and 150 μm to capture the impact of the overlayer on resonator performance.
- A square wave pattern was added at the ground plane edge to ensure wire bonding from package ground to both layers.
- A set of alignment marks were included to align with the resonator mask.

Fig. 5.5 shows a zoomed-in image of the two masks superimposed over each other near the feedline. The red region shows the resonator mask, while the green shows the overlayer mask. The distances $s_c$ and $l_c$ determine the coupling of the resonator and the feedline. The values were chosen such that the coupling quality factor $Q_C$ ~200k. Resonator 1 and resonator 2 had different setbacks $s_{b_1}$ and $s_{b_2}$ on both sides of the

resonator. Overlayer was kept at a distance $s_c + 2g + w$ far from the feedline to ensure minimal impact from the overlayer.

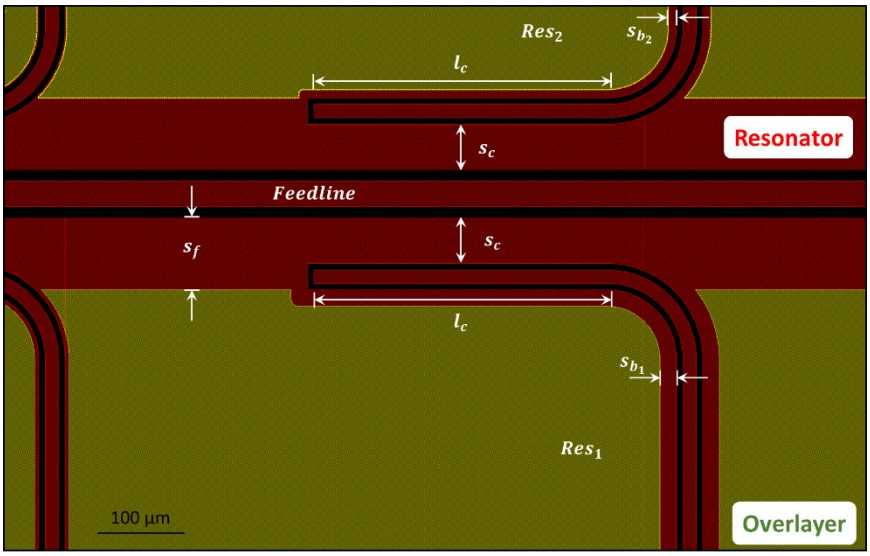


*Fig. 5.5: Zoomed in view if the superimposed resonator with overlayer masks*

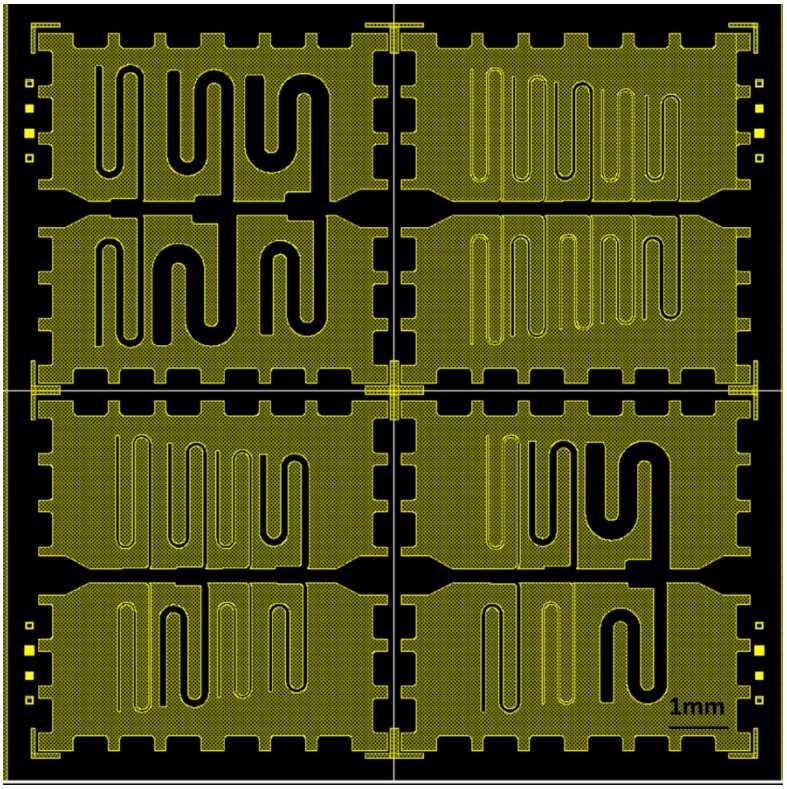


*Fig. 5.6: Overlayer mask design.*

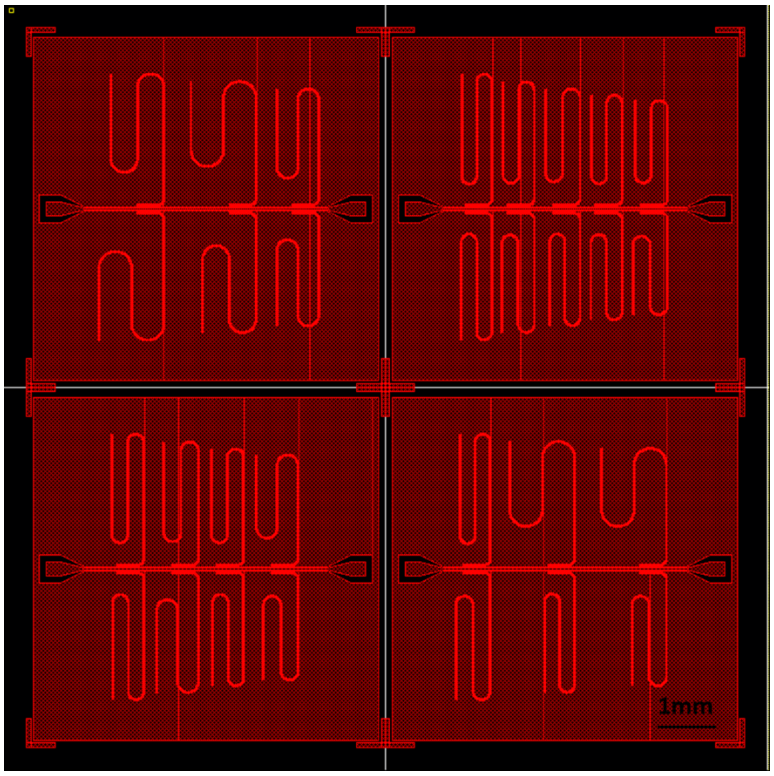


*Fig. 5.7 Resonator mask design.*

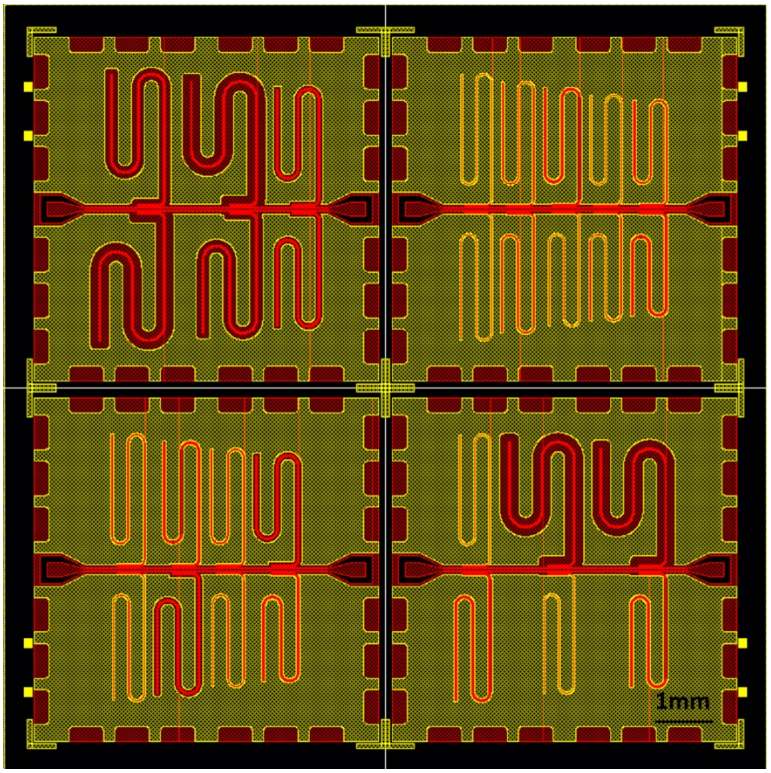


*Fig. 5.8 Overlayer mask overlayed on the resonator mask.*

Fig. 5.6 and Fig. 5.7 show the final overlayer and resonator designs. Fig. 5.8 shows the superimposed masks corresponding to the final device design. Finally, I note that I used Cadence Virtuoso Layout editor design masks.

## *5.3 Device Processing and Packaging*

I fabricated resonators in the class-10 device processing cleanroom at LPS. The above-grown 3-inch wafer is diced into 16mm × 16 mm chips, and each chip was processed separately to make devices. The chip went through the two-step lithography process, as shown in Fig. 5.9 for the quasiparticle trap devices. The aluminum and titanium nitride resonators were fabricated with a one-step lithographic process using the resonator mask. The aluminum resonator used a different mask with resonators with central conductor width of 6 μm and a gap of 3 μm. TiN resonators were patterned using the RIE etch while aluminum was wet etched. The processing steps are described below.

### 5.3.1 Lithography steps

1. First, the chip was thoroughly cleaned by ultrasonication in acetone, methanol, and iso-propyl alcohol (IPA) solvents to remove any organic contaminants. The wafer was optically observed under a microscope for any particulates.
2. The overlayer pattern was transferred using an i-line (365 nm) negative photoresist (PR) AZ® nLOF 2020. The GCA ALS stepper transferred the photomask image to the substrate with a 5x reduction. The exposed photoresist

was baked and developed using a matching Tetramethylammonium hydroxide (TMAH) based developer AZ® 300 MIF Developer.

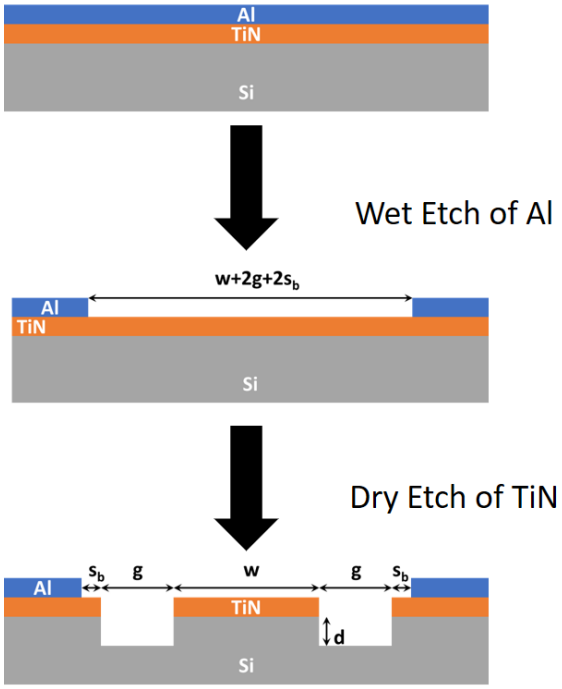


*Fig. 5.9: Processing steps*

3. The chip was wet etched with Transene Type A aluminum etchant for ~120 s to remove the aluminum layer. The etchant selectively etches the aluminum without harming the TiN underneath.
4. The PR was then stripped with a series of N-Methyl-2-pyrrolidone (NMP) based Microposit 1165 solvent baths.
5. The solvent clean was repeated before the following lithographic process.
6. The resonator pattern was transferred using a negative photoresist. Extreme care was taken to match the existing overlayer pattern using alignment marks.
7. It was then dry etched in a PlasmaTherm inductive coupled reactive ion system using a gas mixture of 12.5 sccm $BCl_3$ and 2.5 sccm $Cl_2$ and RF power of 500

W for 5 min. Sufficient etching time allowed for etching the silicon to about 300 nm.

8. The PR was stripped with a series of Microposit 1165 solvent baths and a final clean with deionized water and IPA.
9. The device was optically inspected to record any defects.
10. The chip was PR coated and diced into 6 mm ×6 mm samples in a Disco DAD 4230 dicing saw using disco's blade ZH05-SD2000-N1-50 at a feed rate of 5mm/s.
11. The 6 mm ×6 mm chips were again cleaned using 1165 and solvent baths to strip the protective PR.

Fig. 5.10 shows a dark field image of the aluminum etched overlayer, while Fig. 5.11 shows a final device for one of the quadrants. Fig. 5.10 also shows the alignment marks essential for aligning the overlayer pattern with the resonator pattern. Close examination of the photo shows I achieved an alignment error of around 130±65 nm.

### 5.3.2 Packaging steps

Diced 6 mm × 6 mm samples were packaged in a copper mount and electrically connected to a PCB. The packaging was done outside the cleanroom. Chris Weddle from the Richardson group helped me with packaging. First, the copper package was sandpapered and solvent cleaned to remove the oxide layer to improve thermalization. The PC board was attached to the copper block with an indium foil interface for better thermal conductance. Next, the non-magnetic SMA connectors were soldered to the PCB to connect with the adiabatic demagnetization refrigerator (ADR). Care was taken

to ensure that components used in packaging are non-magnetic. The chip was directly attached to the copper block using GE varnish, which aided it to thermalize efficiently, initially with the package and eventually with the fridge. The chip was then wire-bonded with the PCB. Both TiN and Al layers were separately and sufficiently wire bonded, as shown in Fig. 5.12(a). Additionally, the wirebonds were made across the transmission line to reduce unwanted parasitic mode due to the differential ground plane potential. Fig. 5.12(b) shows the wirebonds across the feedline. Before the final loading into the ADR, the package underwent another solvent clean using acetone, methanol, and IPA to remove any contaminants accumulated during the mounting and wire bonding steps. A sample final packaged resonator is shown in Fig. 5.13.

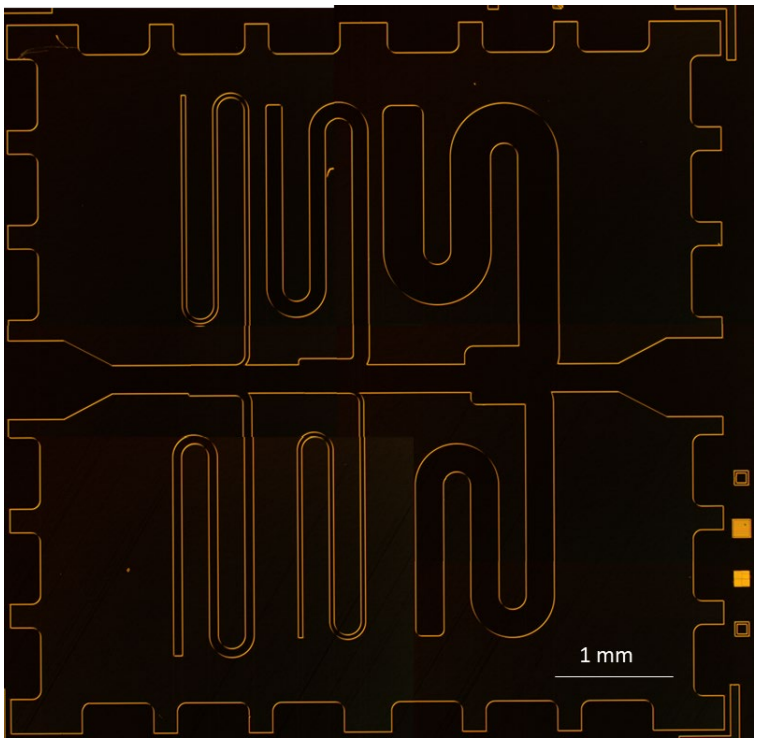


*Fig. 5.10: The optical image of the chip after patterning the aluminum layer. The image also shows the alignment marks used to align for the next mask*

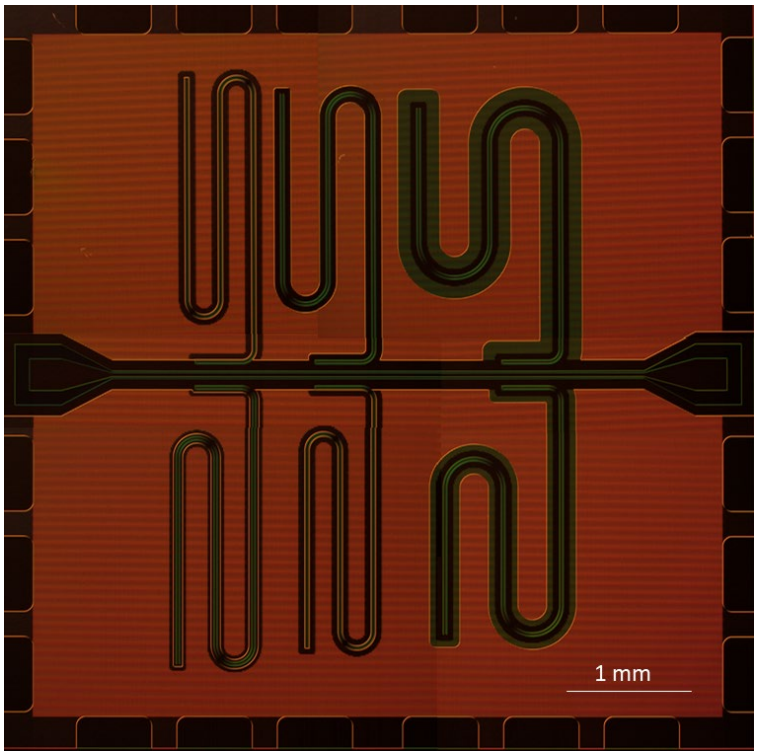


*Fig. 5.11: Final processed die after patterning the resonator features*

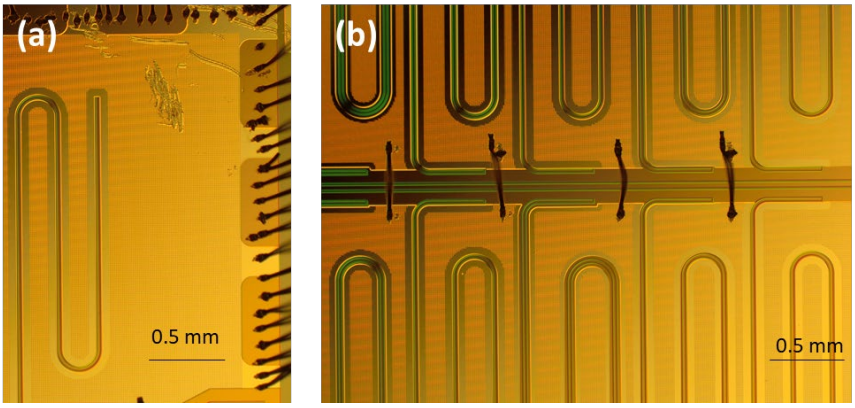


*Fig. 5.12: (a) Optical photograph showing ground plane wirebonds for both Al and TiN layers (b) Wirebonds across the feedline to reduce parasitic modes due to unequal potential of ground planes*

## *5.4 Resonator Measurement Setup*

I measured the resonators in a High Precision Devices (HPD) adiabatic demagnetization refrigerator (ADR). Fig. 5.14 shows a schematic of the ADR

connections. The input signal of 0dBm from the Agilent E5072A vector analyzer fed into a variable attenuator for a dynamic range of testing power applied to the DUT. The input path contained a series of attenuators that attenuate the input signal by 70 dB to reduce the room temperature thermal noise from the electronics entering devices at the colder stage. DC blocks were on the input and output lines to prevent unwanted DC signals from traveling to the resonator. On the return line, a Low Noise HEMT amplifier CITCRYO 4-8A amplified the output signal improving its signal-to-noise ratio. Isolators blocked any reflection from the amplifier to the device without impeding the signal from traveling up the output lines. All the components were anchored to the respective stages to obtain maximum thermalization to reduce any black body radiation present in cables. The device under test (DUT) was attached to the 50 mK stage, where the base temperature reaches around 40-50 mK.

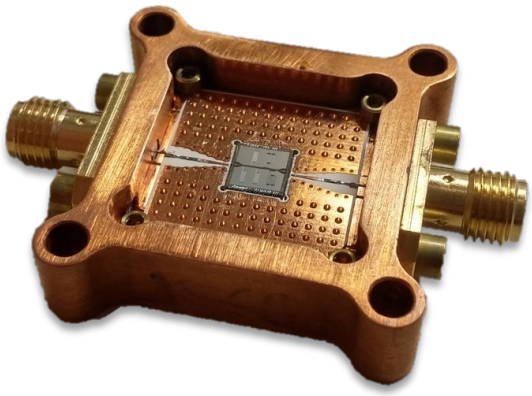

*Fig. 5.13: Sample cooper package with resonator chip ready for ADR characterization*

A light-tight copper enclosure surrounded the DUT to isolate the device from any stray external electric field. An Amuneal Mu-metal shield at the 3k stage protected the device from stray magnetic fields.

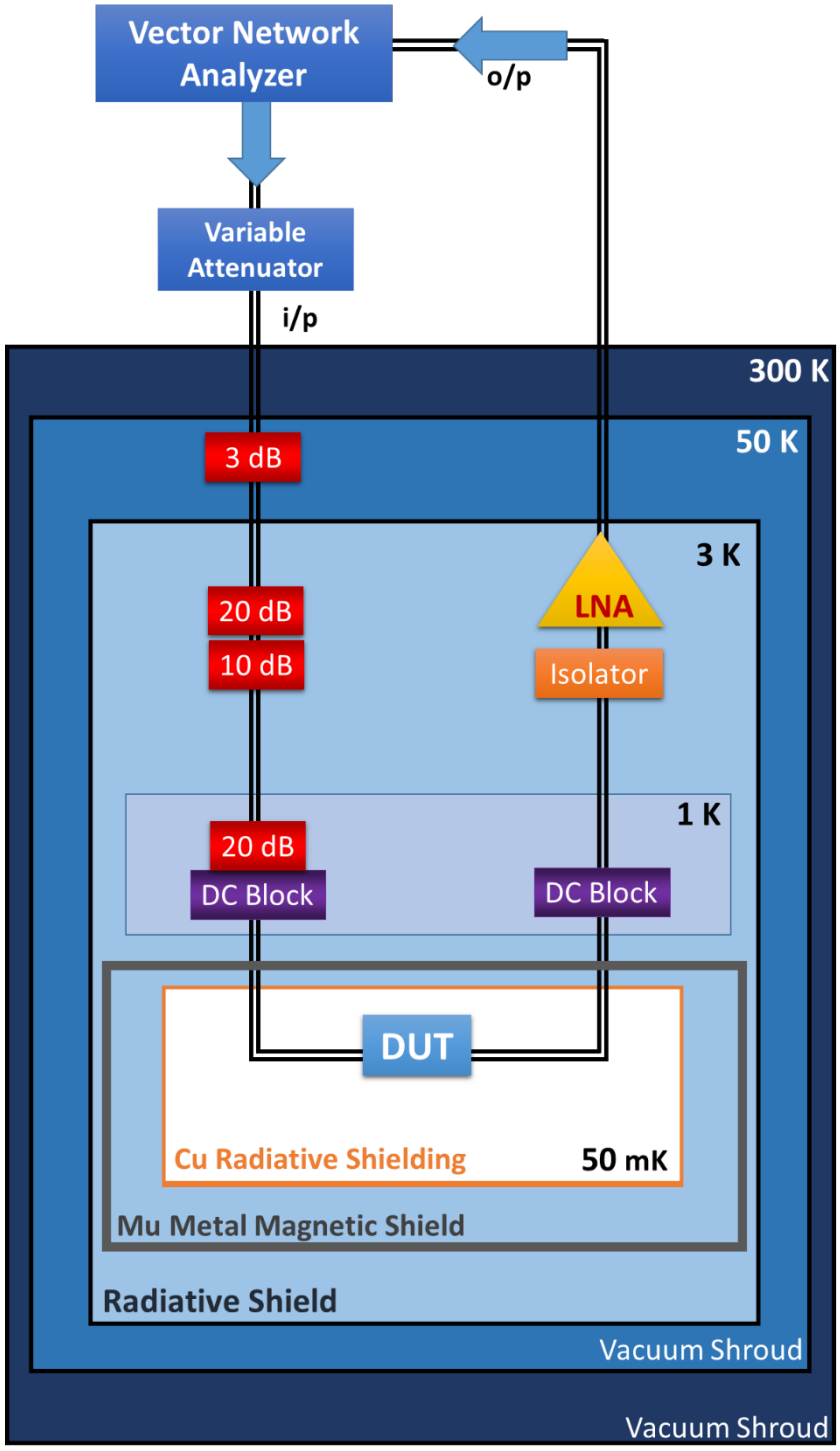


*Fig. 5.14: Schematic of setup in the Adiabatic Dilution Refrigerator (ADR).*

It was further enclosed in a radiation shield containing a black coating with high absorptivity at the 3K stage to prevent any black body radiation or stray light from

higher stages [35]. These boxes were finally enclosed with two more radiation shields attached to the 50 K and 300K stages to prevent heat absorption from higher temperature stages. The entire system was pumped to a high vacuum to eliminate heating via thermal conduction through gas molecules. The components between various stages were connected via low thermal conductive semi-rigid stainless steel (SS-085 and SS-47) cables or NbTi superconducting cables. These also provided additional attenuation to the input line signals. On the other hand, the same stage components were connected via copper lines to reduce RF loss.

## *5.5 Measurement and analysis of the resonator quality factor*

The loaded quality factor of the resonator was determined from the measurement of the complex transmission coefficient, $S_{21}(f)$, which is the ratio of the voltage amplitude $V_2$ at the output port divided by voltage amplitude $V_1$ at the input port. The loaded quality factor, $Q_T$, includes the energy loss from all sources, including internal losses and from a coupling between the feedline and resonator. $Q_T$ is given by

$$\frac{1}{Q_T} = \frac{1}{Q_I} + \frac{1}{Q_C} \tag{5.1}$$

where $Q_C$ is the coupling quality factor, which depends on the coupling capacitance and $Q_I$ is the internal quality factor. To first order for $\omega_o C_C Z_l \ll 1$ and a matched transmission line, the coupling quality factor is given by [127]

$$\frac{1}{Q_C} = \frac{\pi}{4 Z_o Z_l (\omega_o C_c)^2} \tag{5.2}$$

where $Z_o$ and $Z_l$ are the characteristic impedance of the feedline and transmission line of the resonator, $\omega_0$ is the resonant frequency and $C_c$ is the coupling capacitance. For a matched input and output impedance, the transmission response has a symmetric dip near resonance. Mismatch in the transmission line port impedance and the parasitic series impedance of the feedline leads to asymmetry in the transmission response, as seen in Fig. 5.15(a). The asymmetry manifests itself as a complex coupling quality factor[128]. The transmission coefficient of the resonator, including all the non-idealities, can be written as [70]

$$\tilde{S}_{21}(f) = e^{i(\theta+\kappa L)}\left[1 - \frac{\left(Q_T/Q_C\right)e^{i\phi}}{1 + 2iQ_T\left(\frac{f-f_0}{f_0}\right)}\right] \tag{5.3}$$

The angle $\theta$ accounts for the phase shift due to the measurement system and components in the output and input lines, $\kappa L$ represents the phase shift introduced due to the input and output cable path length. $\phi$ represents the coupling phase. The exact source of these artifacts is not relevant to understanding the resonator behavior. In all, seven parameters need to be extracted from fitting the data with the fit function: $\theta, \kappa L, \phi, Q_T, Q_C, Q_I$ and $f_0$. These parameters are extracted by plotting the transmitted data in both parametric and complex spectral domains. In the complex plane, the $\tilde{S}_{21}(f)$ data forms a circle, as shown in Fig. 5.16(a). Each blue point represents the measured value at different frequencies. The red star represents the resonant frequency. The points at the edge of the circle correspond to the start and end data points. The diameter of the circle gives an initial estimate for $Q_T/Q_C$. For a symmetric resonance, the circle is symmetric about the real axis with the circle's center and point

corresponding to resonance lying on the real axis. The non-zero coupling phase $\phi$ and the term $e^{i(\theta+\kappa L)}$ leads to the rotation and translation of the circle. For certain conditions, even a spiral nature can be introduced in the data. A geometric circular fit of the circle gives values for $\theta, \phi$ and $\kappa L$. [128], [129].

$Q_I$ is not directly determined by the fitting function described by Eq. (5.3) as it fits for $Q_T$ and $Q_C$ which need to be solved for $Q_I$ using Eq. (5.1) . Instead inverse $\tilde{S}_{21}(f)$ gives $Q_I$ directly as a fitting parameter. The $\tilde{S}_{21}^{-1}(f)$ is given as

$$\tilde{S}_{21}^{-1}(f) = e^{-i(\theta+\kappa L)}\left[1 + \frac{Q_I}{Q_C}e^{i\phi}\ \frac{1}{1 + 2iQ_I\left(\frac{f-f_0}{f_0}\right)}\right] \tag{5.4}$$

Similarly, $\tilde{S}_{21}^{-1}(f)$ also generates a circle in the complex plane, as shown in Fig. 5.16(b) with the corresponding resonant frequency marked with a star. Fig. 5.15(c) and (d) show the corresponding magnitude and phase data. The magnitude of $\tilde{S}_{21}^{-1}(f)$ generates a peak at the resonance. The diameter of the circle in the complex $\tilde{S}_{21}^{-1}(f)$ plane gives $\frac{Q_I}{|Q_C|}$. A significant difference between the $\tilde{S}_{21}^{-1}(f)$ and $\tilde{S}_{21}(f)$ data in complex plane is that off-resonance data gets to cover a relatively small region in the $\tilde{S}_{21}^{-1}(f)$ data circle compared to the $\tilde{S}_{21}(f)$ which can also be noted in Fig. 5.16. Hence it is required to collect a significant number of data points near resonance.

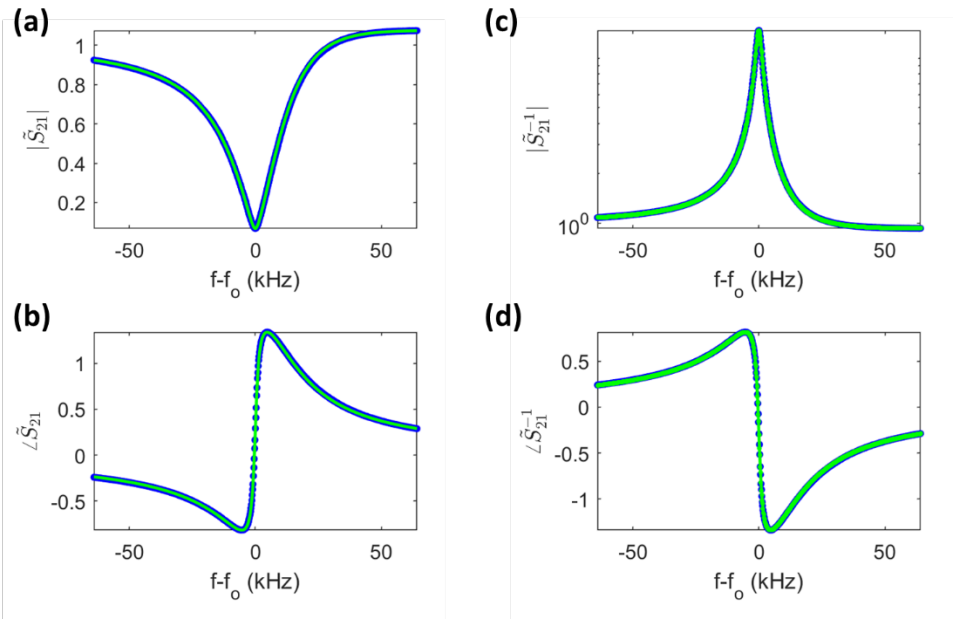


*Fig. 5.15: (a)&(b) The magnitude and phase data of $S_{21}(f)$ and (c)&(d) corresponds to $S_{21}^{-1}(f)$ for aluminum resonator Al-R04 at T=45 mK and $n_p = 1.1 \times 10^5$*

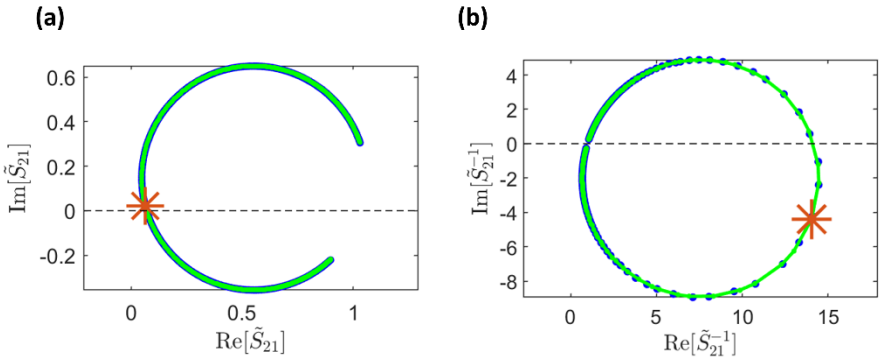


*Fig. 5.16: Circle fits for(a) $S_{21}$ and (b) $S_{21}^{-1}$. '*' shows the position of resonant frequency in both the plots for aluminum resonator Al-R04 at T=45 mK and $n_p = 1.1 \times 10^5$*

The calculation of $Q_I$ from the real and imaginary values of $S_{21}$ suffers from the additive noise present in the measurement system and error propagation of calculating $Q_I$ from extracted values of $Q_C$ and $Q_T$. Even though using $S_{21}^{-1}(f)$ leads to a complex relationship between noise and data, error propagation is by far the largest concern of extracting resonance parameters from data fitting routines.

### 5.5.1 Data Measurement Procedure

Here I present a brief description of the overall data collection procedure, fitting, and analysis procedure that I used for characterizing the resonators.

1. First, a broad frequency sweep is performed to identify the resonant frequencies of the various resonators in the package. Spikes in the derivative phase, $\partial\theta/d\omega$ Were used to identify the resonator frequencies.
2. Next, each resonator was measured on a timescale near each resonance to be further refined using an automated protocol.
3. Around the refined frequency location, complex $S_{21}(f)$ data was collected using a segmented frequency sweep with sparse data points for the off-resonance region and denser points near the resonance.
4. The data were averaged if required to obtain SNR ~ 5 for the complex plane's geometric fit.
5. The data was repeatedly collected at different RF power to obtain the power dependence of the resonator quality factor by adjusting the variable attenuator. The highest measured power level for the resonator was below the power, which could induce nonlinear effects in the resonance like resonance bifurcation, compression of output due to amplifier saturation [130], [131]. The Al and TiN resonators were measured for total input powers lower than -95 dBm and -90 dBm, respectively, for the designed coupling of the resonators with the feedline.
6. After collecting the power dependent data at a specific temperature, the refrigerator temperature was increased at 1 mK per 20 s using the temperature regulation module of ADR control software. After reaching the final

temperature, the fridge was allowed to thermalize for 30 min before taking the data.

7. The temperature was adjusted from a base temperature of 50 mK in steps of 30-40 mK to a maximum temperature of $T_c/4$. For aluminum, the maximum temperature is 320 mK, while for TiN is 1.1-1.2 K.
8. After the thermalization, the power dependent measurement was repeated.

### 5.5.2 Fitting procedure

1. The data was treated to remove any amplitude and phase artifacts. An initial estimate for $f_o$ and quality factors were made.
2. Using the initial estimates, the linear least-squares fit was performed on the real and imaginary parts of $\tilde{S}_{21}^{-1}(f)$ to find the best fit values of $f_0$, $Q_C$, and $Q_I$. The output of the fits on the complex $\tilde{S}_{21}^{-1}$ for one of the sample data for the Al resonator Al-R04 is shown in Fig. 5.16(b). The corresponding fit on $\tilde{S}_{21}(f)$ is shown in Fig. 5.16(a). Both the fits track the data well, which can be seen in the corresponding magnitude and phase fits in Fig. 5.15 for both $\tilde{S}_{21}(f)$ and $\tilde{S}_{21}^{-1}(f)$. Fig. 5.17 shows the extracted $Q_I$ at varying photon numbers for an aluminum resonator Al-R04 at 45 mK.
3. As $Q_C$ of resonators primarily depends on the device's geometry, it should be temperature and power independent. But the measured data still contain power and temperature dependency due to the uncertainty in data which leads to parameter variation. Fig. 5.18 shows a sample power dependence of coupling

quality factor $Q_C$ for the aluminum resonator Al-R04, which does not have a proper trend. To eliminate any dependency, a median of all extracted $Q_C$ for power ($n > 10^3$) and temperatures below $\frac{T_c}{10}$ was taken. The data was then refitted to extract parameters $f_0$ and $Q_I$ with the fixed $Q_c$.

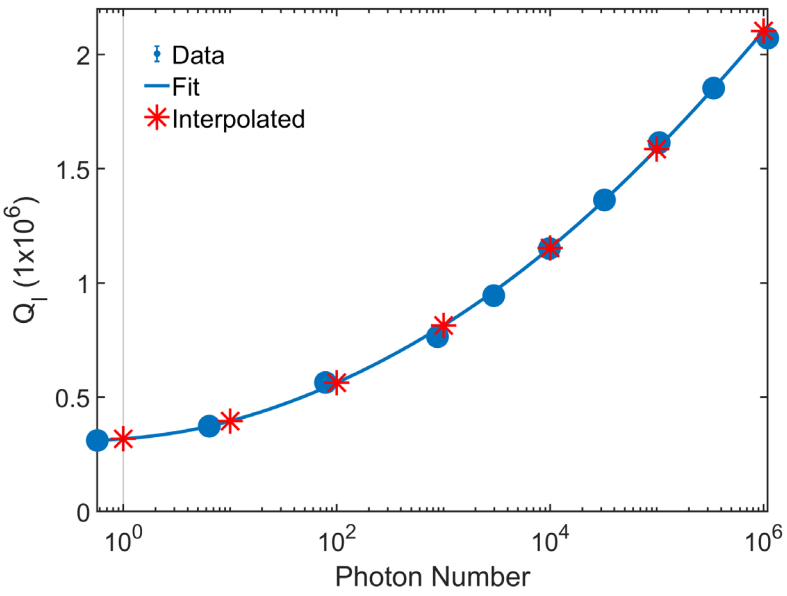


*Fig. 5.17: Sample power dependent of $Q_I$ versus photon number for aluminum resonator Al-R04 at T = 45 mK.*

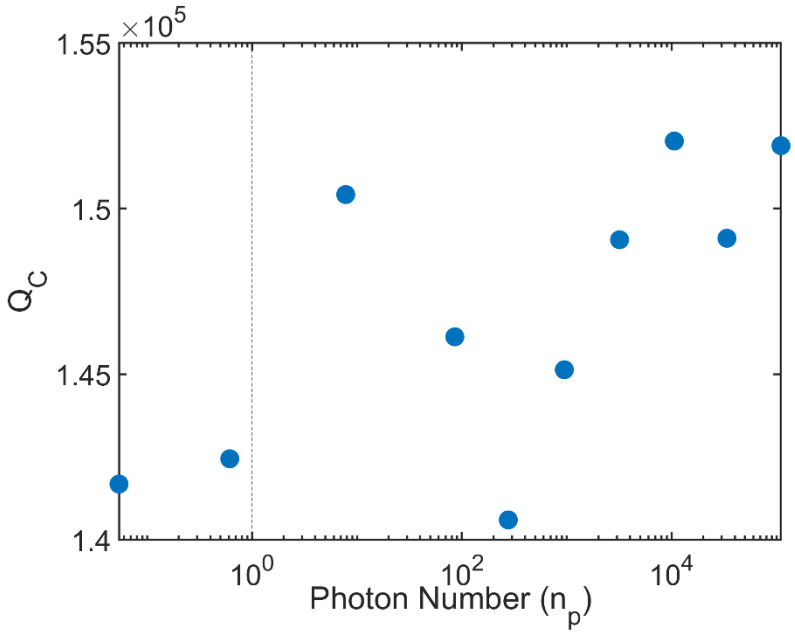


*Fig. 5.18: Sample power dependence of $Q_c$ versus photon power for aluminum resonator Al-R04 at T = 45 mK*

### 5.5.3 Analysis procedure

1. For each $\tilde{S}_{21}(f)$ measurement, the input power applied to the resonator $P_{in}$ can be related to an average photon number present in the resonator by the standard relation when driven at its resonance frequency[80]

$$\langle n_p \rangle = \frac{2}{\hbar \omega_r} \frac{Q_T^2}{Q_C} P_{in} \tag{5.5}$$

Here $\omega_r = 2\pi f_o$ is the angular resonance frequency in rad/s. The attenuation in the input line of the ADR was measured to be -71.7 dB at 5GHz.

2. A power dependent quality factor fit based on the TLS model that assumes a standard distribution of TLS as given in Eq. (5.6) was performed[70], [121].

$$\frac{1}{Q_I} = \frac{1}{Q_A} + \frac{1}{Q_{TLS}^{T_b}} \frac{1}{\sqrt{1 + \left(\frac{n_p}{n_c}\right)^{\alpha}}} \tag{5.6}$$

Here I have treated $Q_A$, $Q_{TLS}^{T_b}$, $n_c$ and $\alpha$ as free parameters. As discussed previously, if TLSs are responsible for the observed power dependence of $Q_I$, we should obtain $\alpha$ = 1. Significant deviation from this value is the evidence for non-TLS mechanisms.

3. Using the fit values, $Q_I$ was interpolated for the photon numbers $10^0$, $10^1$, $10^2$, $10^3$, $10^4$, $10^5$, $10^6$. A sample power dependent data of an aluminum resonator measured at T = 45 mK is shown in Fig. 5.17. The blue circles represent the data measured at different input power. The power has been translated to the corresponding photon number as described above. The blue curve shows the best fit on the data using Eq. (5.6). The interpolated values of $Q_I$ at its desired photon numbers shown here by red stars.
4. For each photon number, $Q_I$ from different temperatures were grouped for the temperature dependent fits to Eqs. (3.18)-(3.20). A sample temperature dependent fit of the aluminum resonator for the photon number $\langle n_p \rangle$ =100 is shown in Fig. 5.19. The DC measured critical temperature of the aluminum was 1.20 K, and temperature data were collected until $T < \sim \frac{T_c}{4} \sim$ 0.32 K. I discuss a detailed analysis of this data in the next chapter.

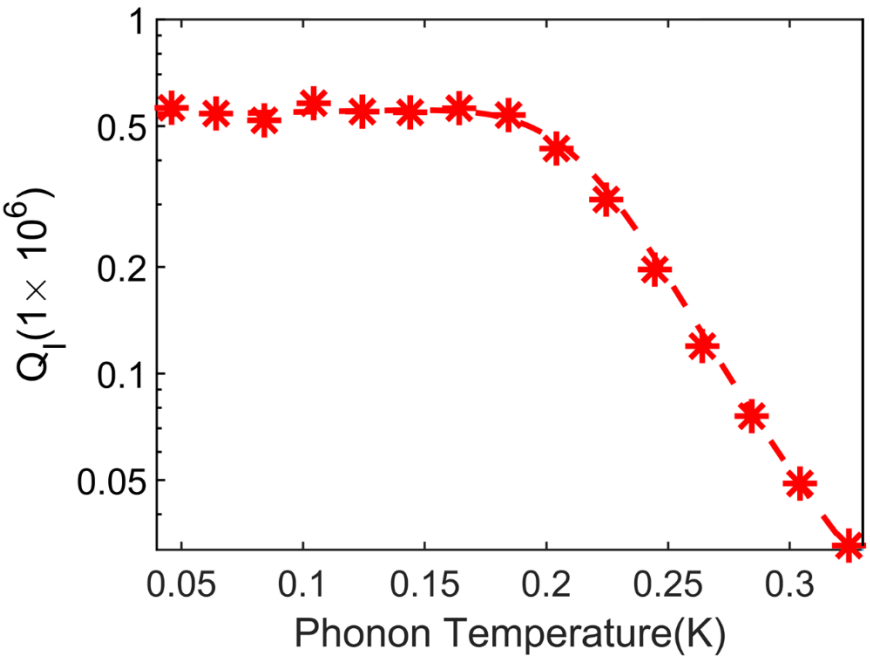


*Fig. 5.19: Internal quality factor $Q_I$ versus temperature fit on aluminum resonator Al-R04 for $n_p$= 100*

# Chapter 6 : Resonator measurements

In this chapter, I describe my measurements of resonators at different applied microwave power at different temperatures to obtain the power and temperature dependence of their quality factors. The titanium nitride and aluminum resonators are measured, and the proposed TLS-quasiparticle power-temperature model is applied to extract the loss parameters and explore the model assumptions. Additionally, the quasiparticle trap devices are measured, and their performances are compared with a bare TiN resonator to determine the role of setbacks on quasiparticle trapping efficiency and other model parameters.

## *6.1 TiN resonators*

The two titanium nitride resonators TiN-R02 and TiN-R06, were measured at microwave powers corresponding to average photon numbers ranging from $10^0$ -$10^6$ at temperatures from 40 mK to 1.18 K with 30-50 mK intervals. These resonators had a critical temperature, $T_C$ of 5.3 K.

Both resonators had a loss with similar power and temperature dependence, only the data for TiN-R02 is presented here. First, comparing the individual $S_{21}(f)$ fits for all temperature and power. The extracted $Q_C$ from individual $S_{21}(f)$ at different powers and different temperatures is presented in Fig. 6.1. The variation in the $Q_C$ does not have a clear trend. As discussed in section 5.5.2, to reduce the variability in $Q_c$, I chose a constant value of 149,000 for all power and temperature spectra and refit the whole dataset to extract other resonance parameters, primarily $Q_I$ and $f_o$.

Fig. 6.2 shows the temperature and power variation of extracted $f_o$ with fixed $Q_C$. There is a temperature dependence of resonant frequency with temperature due to the increased participation of thermal quasiparticles. The relative variation of resonant frequency for the whole data is 1.2e-5. The impact of this variation is small for my model, hence I have used a constant frequency, $f_0$, of 4.46956 GHz.

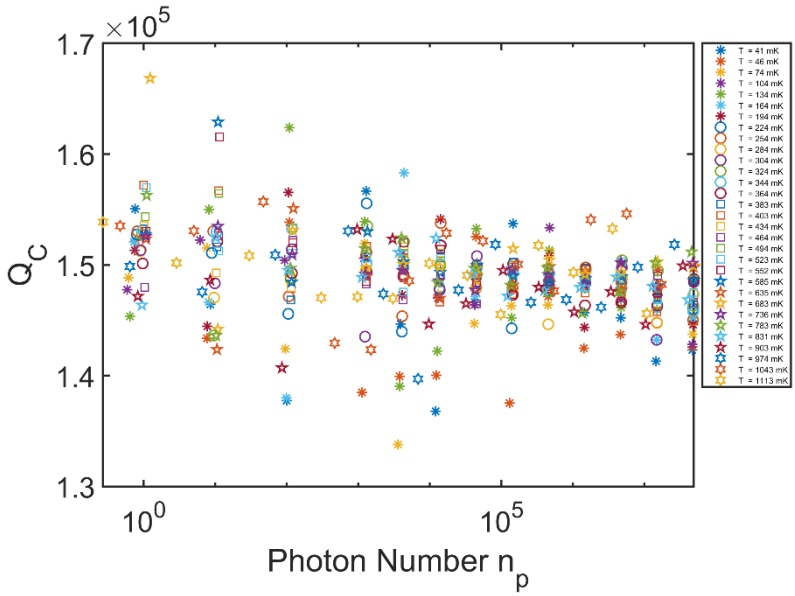


*Fig. 6.1: Coupling quality factor $Q_C$ the resonator TiN-R02 versus photon number at different measured temperatures from individual S21 fits for non-fixed $Q_C$*

For TiN-R02, the single-photon quality factor, $Q_I$, of 400,000 at the lowest measured temperature of 40 mK. These power and temperature dependence of $Q_I$ was further analyzed with the model governed by Eqs. (3.18)-(3.20), using the analysis protocol described in the last chapter. Additional considerations were made to limit the variability of the model parameters for the data series. The equations (3.18)-(3.20) have seven fitting parameters, three each for TLS: $Q_{TLS}^0$, $n_c$, and $\alpha$; and quasiparticle loss: $I_{ext}$, $\kappa$, and $s$; while $Q_A$ represents the non-power and temperature loss. Ideally, the governing equations wholly capture the temperature dependence of TLS and

quasiparticles. Hence, I have considered all the parameters in this model to be temperature independent. The exact nature of the trapping rate s, external quasiparticle generation rate $I_{ext}$ and excess quasiparticle loss parameter $\kappa$ are not known, so I have treated them as power dependent parameters. In the device design, I had incorporated various constraints to reduce non-TLS and non-quasiparticles losses. Therefore, I had set $Q_A$ (inverse of the non-power, non-temperature loss) to a sufficiently high constant value of $2\times10^7$.

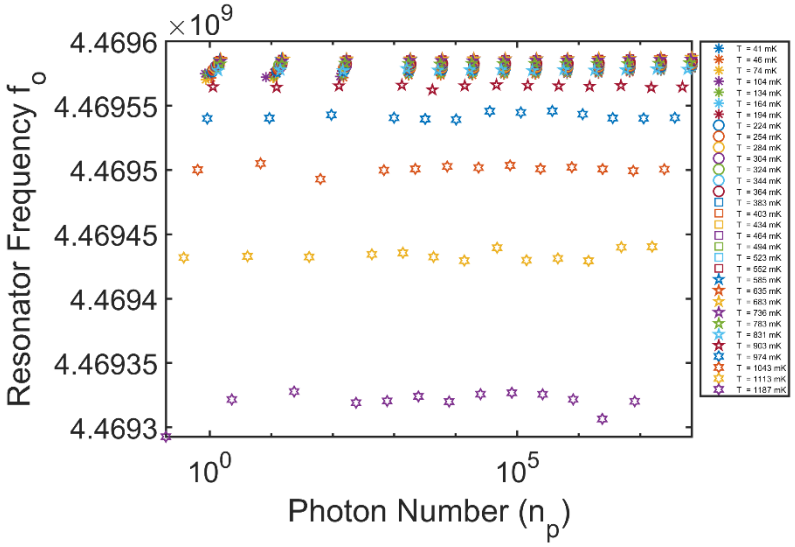


*Fig. 6.2: Resonant frequency of the resonator TiN-R02 versus photon number at the different measured temperature*

The independent temperature fits using Eqs. (3.18)-(3.20) for each photon power treats $Q_{TLS}^0, n_c$, and $\alpha$ as independent parameters. I performed initial fit for all powers by keeping two of the three parameters constant across all powers and allowed the third parameter to vary. In this case, I kept $n_c$ and $\alpha$ constant and varied $Q_{TLS}^0$. After the first round of fits for all powers, I obtained different values of $Q_{TLS}^0$ at different powers.

Using the relation $\frac{1}{Q_{TLS}^{*}} = \frac{1}{Q_{TLS}^{o}}\left(\frac{1}{\sqrt{1+\left(\frac{n}{n_c}\right)^{\alpha}}}\right)$, I calculate the effective temperature independent component of $Q_{TLS}^{*}$ for each power. I then refitted the $Q_{TLS}^{*}$ using the above relation and extracted a single value of $Q_{TLS}^{0}, n_c$, and $\alpha$. I repeated the temperature fits for all powers using extracted $Q_{TLS}^{0}, n_c$, and $\alpha$ values as the starting point for the next iteration of fits. The process is repeated to improve the fit and to converge for power-independent values of $Q_{TLS}^{0}, n_c$, and $\alpha$. Since I simultaneously performed temperature fits for different powers to extract a unique value of $Q_{TLS}^{0}, n_c$, and $\alpha$ , the overall fit routine is a power and temperature fit of the whole data set.

As I described earlier in section 3.3, the interdependence of $I_{ext}$ and $s$ makes it challenging to capture the power dependence of both parameters simultaneously. To reduce the complexity of fit, I chose to keep one constant and the other one as a variable. According to Eq. (3.21), $x_{qp,T_{low}}$ increases with increasing $I_{ext}$ or decreasing $s$. As we would later see in the analysis, $Q_{QP}$ which is inversely proportional to $x_{qp}$, increases with power. For a constant $s$, it means $I_{ext}$ decrease with power or for given $I_{ext}$, $s$ increases with power. Since decreasing $I_{ext}$ with power is less intuitive, I have held $I_{ext}$ constant and allowed $s$ to vary in the fit. Holding $I_{ext}$ constant leads to the exclusion of direct calculation of microwave power dependence on quasiparticle generation rate. Constant $I_{ext}$ represents only external Cooper pair-breaking quasiparticle sources. Additionally, as the different combinations of $I_{ext}$ and $s$ gives the same quasiparticle density as described in Eq. (3.21), I chose a low value of $I_{ext}$, and report its corresponding trapping rates.

Fig. 6.3 shows the $Q_I$ vs temperature and the corresponding fit for photon numbers 10 and $10^5$. The stars are the interpolated data for a photon number 10, Fig. 6.1(a) and $10^5$, Fig. 6.1(b) at each temperature as discussed in section 5.5.3. For both the low and high powers, the quality factor increases with temperature and peaks near 600 mK (~$T_C/9$) before sharply decreasing due to the loss contribution from thermal quasiparticles. In my model, at lower temperatures, the increasing $Q_I$ with increasing temperatures indicate the presence of TLS loss which gets saturated at high temperature leading to $Q_I$ peak at intermediate temperature. $Q_I$ also increases with increasing microwave power for all temperatures. At low temperatures, the increase in $Q_I$ with power can be associated with saturation of TLS losses. An anomalous increase in $Q_I$ with decreasing temperature at low temperature and low photon number in Fig. 6.3(a) cannot be described by conventional TLS or QP model. Hence it is not captured by this model and not included in the fitting procedure. The exact nature of the increase in the quality factor is unknown, and an experimental artifact cannot be definitively ruled out. A similar increase in the quality factor at low temperatures was reported for aluminum resonators[132].

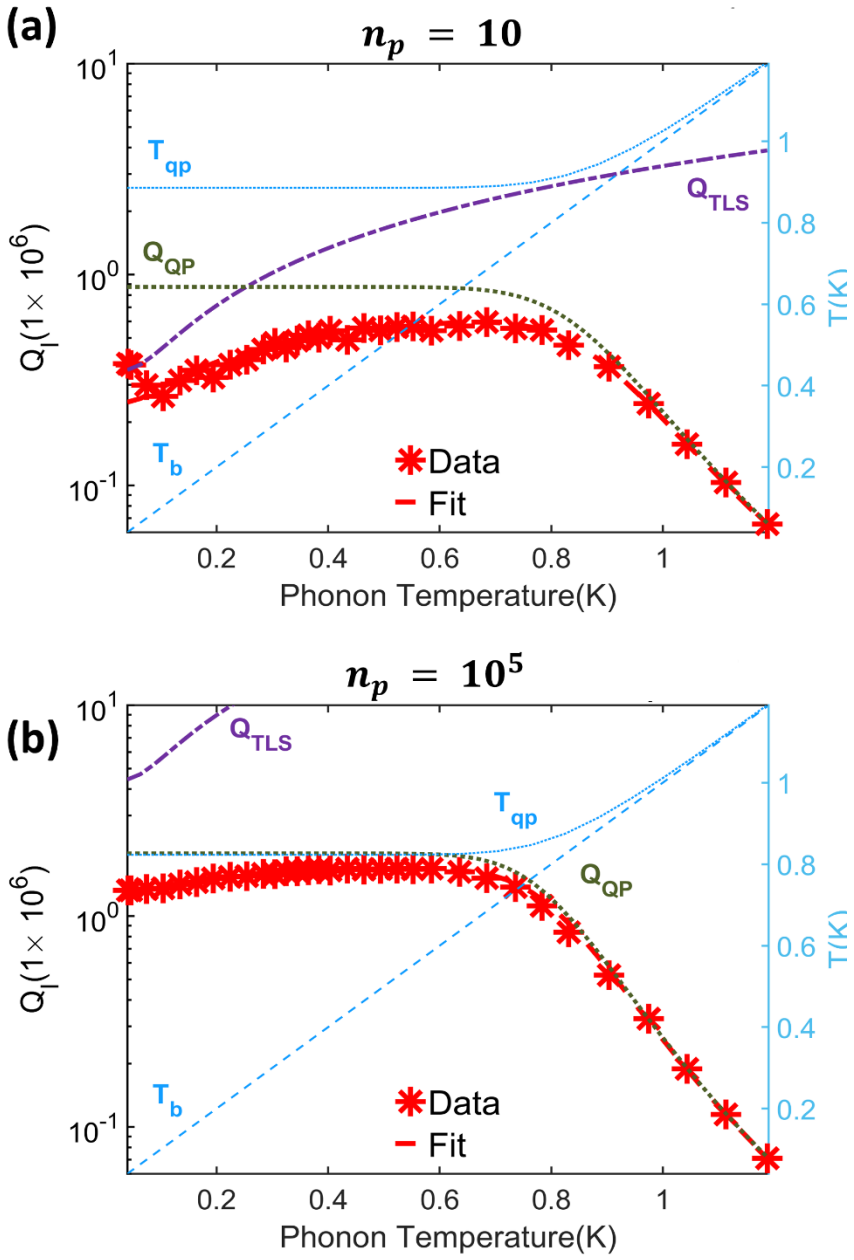


*Fig. 6.3: The fit results of the power-temperature fit on TiN with individual components for data collected at low (a) and high (b) powers*

In Fig. 6.3, the red line shows the fit. The TLS-QP model tracks the data even at the knee region for both low and high power. The loss contribution from TLS (purple dash curve) and quasiparticle losses (green dotted curve) is plotted for all temperatures. Using the DC measured $T_C$, an effective temperature, $T_{qp}$, is calculated using Eq. (3.12).

On the right axis, the effective quasiparticle temperature, $T_{qp}$, is compared with the bath temperature, $T_b$.

There are three primary temperature regimes of the data shown in Fig. 6.3(a) for low power $n_p = 10$ measurements. At low temperatures, both TLS and non-equilibrium quasiparticle extracted losses contribute, indicating significant quasiparticle loss impacting even at low power and low temperature. It is in this regime that most resonators are measured and close to the qubit operating regime. The model results suggest that data in the literature (or at least data collected with this instrumentation at LPS) may be reporting TLS & quasiparticle loss for the TiN resonator performance. In the high-temperature region, thermal quasiparticles predominately dominate, and the quality factor degrades. The intermediate temperature region is a transition from TLS-non-equilibrium quasiparticles loss towards thermal quasiparticle loss. It is the "knee" section of the internal quality factor temperature dependence. When the effective quasiparticle temperature equals bath temperature, the loss is wholly described by the thermal quasiparticle picture. The saturating $Q_{QP}$ at low bath temperatures are caused by the saturation of the non-equilibrium quasiparticle temperature. The model estimates the quasiparticle number and the quasiparticle temperature, which can be extracted using Eq. (3.12) that depends on the critical temperature of the film resulting in an effective quasiparticle temperature around 800 mK. For higher microwave power $n_p = 10^5$, the TLS loss decreases and the total quasiparticle loss dominates the overall loss for all bath temperatures.

Fig. 6.4 describes the complete dataset for the resonator. Fig. 6.4(b) presents the power dependent data measured at different bath temperatures. Different markers

present the raw data. The power dependent data shows increasing $Q_I$ with power for all temperatures. The interpolated $Q_I$ from this raw data with its corresponding temperature fit for various power levels are presented in Fig. 6.4(a). The extracted parameters from temperature fit for all seven power levels are presented in Fig. 6.5 and 6.6. Fits follow the data for all temperatures. The power dependent fit for each temperature is plotted using these extracted parameters to examine the goodness of fit on the data. Power fits track low and high-temperature data, but a slight mismatch in the intermediate knee region (0.730 -1K) for the thermal fit leads to the mismatch in power fits, as shown in Fig. 6.4(b).

The model accommodates the observed increase in $Q_I$ with increasing microwave power by traditional TLS loss (increasing $Q_{TLS}$) and quasiparticle loss (increasing $Q_{QP}$). Increasing $Q_{QP}$ corresponds to the decreasing quasiparticles loss resulting from decreased interaction resulting from increasing the trapping rate $(s)$. The power dependence of the trapping rate, $s$, is shown in Fig. 6.5. A possible explanation for the increase in trapping rate may result from the increased electric field increases the motion experienced by the quasiparticles that accelerate single-particle interactions captured by the trapping term in Eq. (3.7). The power dependence of the trapping rate can be expressed using a phenomenological relation $s(n_p) = 23.7\left(\log(n_p)\right)^2 - 19.9\log(n_p) + 380$. The corresponding temperature dependence of effective temperature and total quasiparticle density is shown in Fig. 6.7. It can be seen that quasiparticle temperature and density decreases with increasing power which is a result of increasing $Q_{QP}$ with increasing power due to enhanced trapping rate.

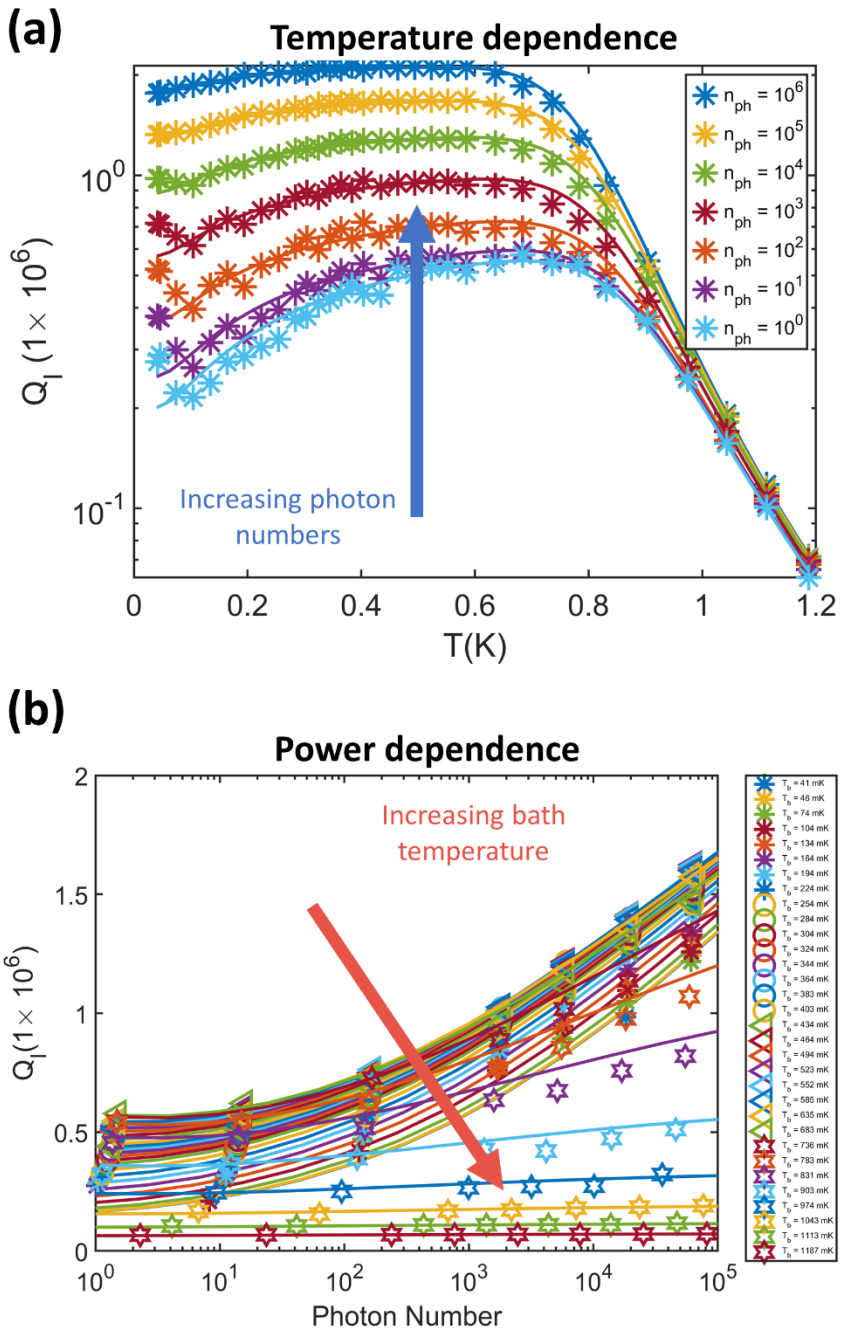


*Fig. 6.4: Data (symbols) and fits (curves) for (a) $Q_I$ versus temperature (b) $Q_I$ versus power for complete dataset for the TiN-R02 resonator*

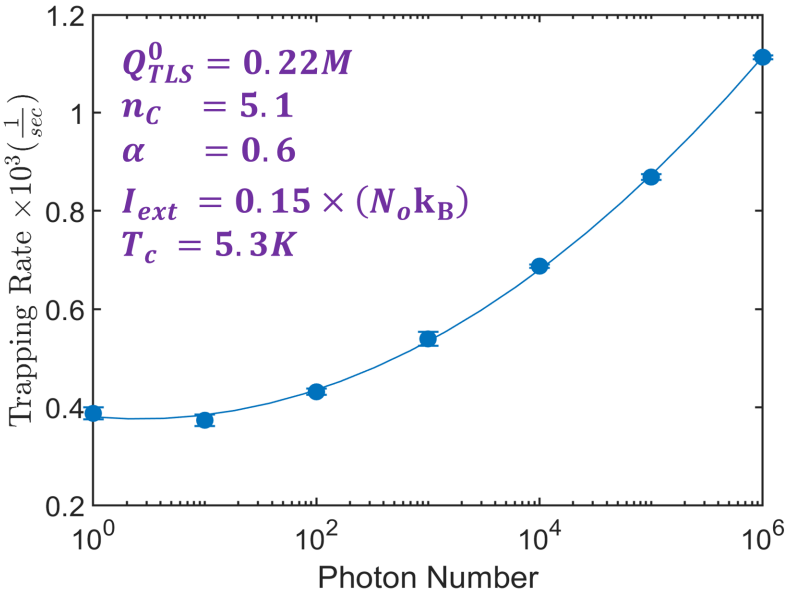


*Fig. 6.5: Extracted parameters from the temperature fit for all photon numbers and the trapping rate s*

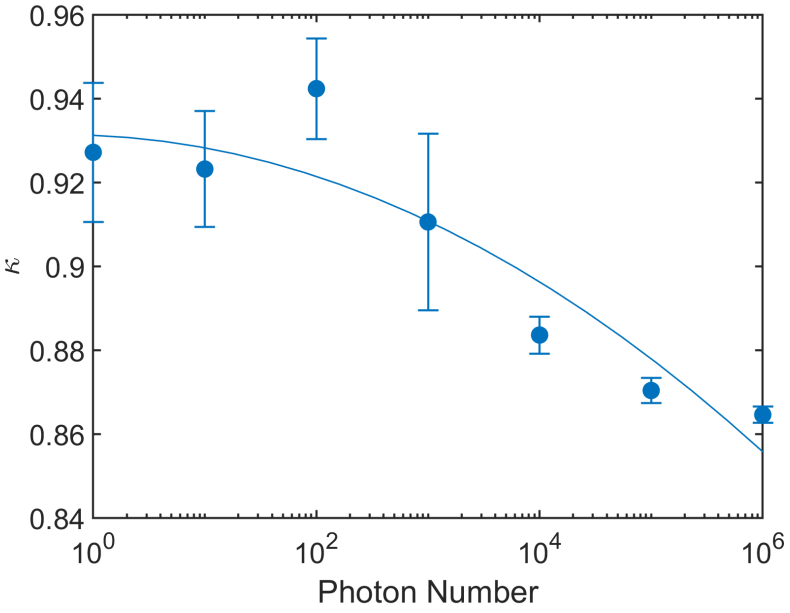


*Fig. 6.6: The excess quasiparticle loss κ versus photon number*

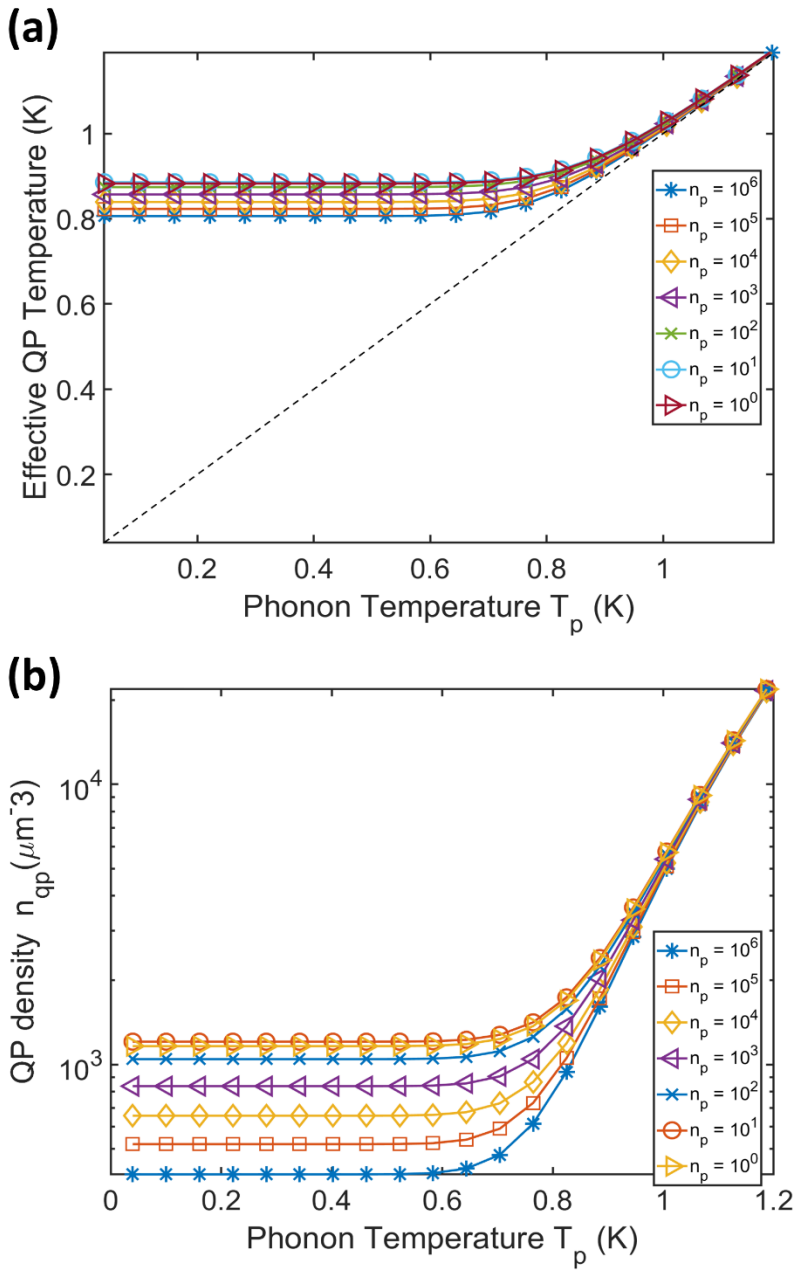


*Fig. 6.7: Plot of (a) quasiparticle temperature versus phonon temperature (b) quasiparticle density versus phonon temperature for Al-R04 resonator.*

The extracted TLS parameters ($Q_{TLS}^{0}, n_c, \alpha$) are reasonable compared to those reported in the literature [17], [77]. The results presented in Fig. 6.4 are determined using the parameter that describes the power dependence, $\alpha$, to be equal to 0.6. This value is different from the $\alpha = 1$ coming from the standard theory for single TLS[63]

and $\alpha = 0.8$ that corresponds to the value calculated from power dependence of simulated CPW with uniform dielectric all along the interfaces[73]. To explore the impact of different values of $\alpha$, I refit the data with $\alpha$ at 0.8 and 1. Fig. 6.8 presents the fit results comparing the fits for different values of $\alpha$. Fig. 6.8(a) shows the fit with extracted parameters of $\alpha = 0.6$. For the other fixed values of $\alpha$, $Q_{TLS}^{o}$ and $n_c$ are chosen to fit well for lower powers. The corresponding values of $Q_{TLS}^{0}$ and $n_c$ is presented in Table 6-1. The choice of $Q_{TLS}^{0}$ and $n_c$ helps to track the low power data well, but it fails to track the data at low temperatures at high powers (red circle). It also leads to a more significant misfit at intermediate temperatures (black circle). The discrepancy increases with higher $\alpha$.

*Table 6-1: Comparison of parameter with changing α*

| Parameter | $\alpha = 0.6$ | $\alpha = 0.8$ | $\alpha = 1$ |
|---|---|---|---|
| $Q_{TLS}^{o}$ | $2.2\times10^5$ | $2.6\times10^5$ | $3.9\times10^5$ |
| $n_c$ | 5.1 | 47 | 290 |

Additionally, the variation in $\kappa$ and $s$ is compared for different values of $\alpha$ is shown in Fig. 6.9. Both of these values adjust slightly to absorb the changes in the TLS parameters. As the changes in the value of $\alpha$ impact the goodness of fit, the extracted value is a reasonably accurate description of the power dependence of TLS. $\alpha$ not being close to 1 indicates the presence of different kinds of TLS at device interfaces with different individual critical power $n_c$, possible multiphoton effects activating an ensemble of TLS defects with different energies, or un-isolated contributions from the quasiparticle population.

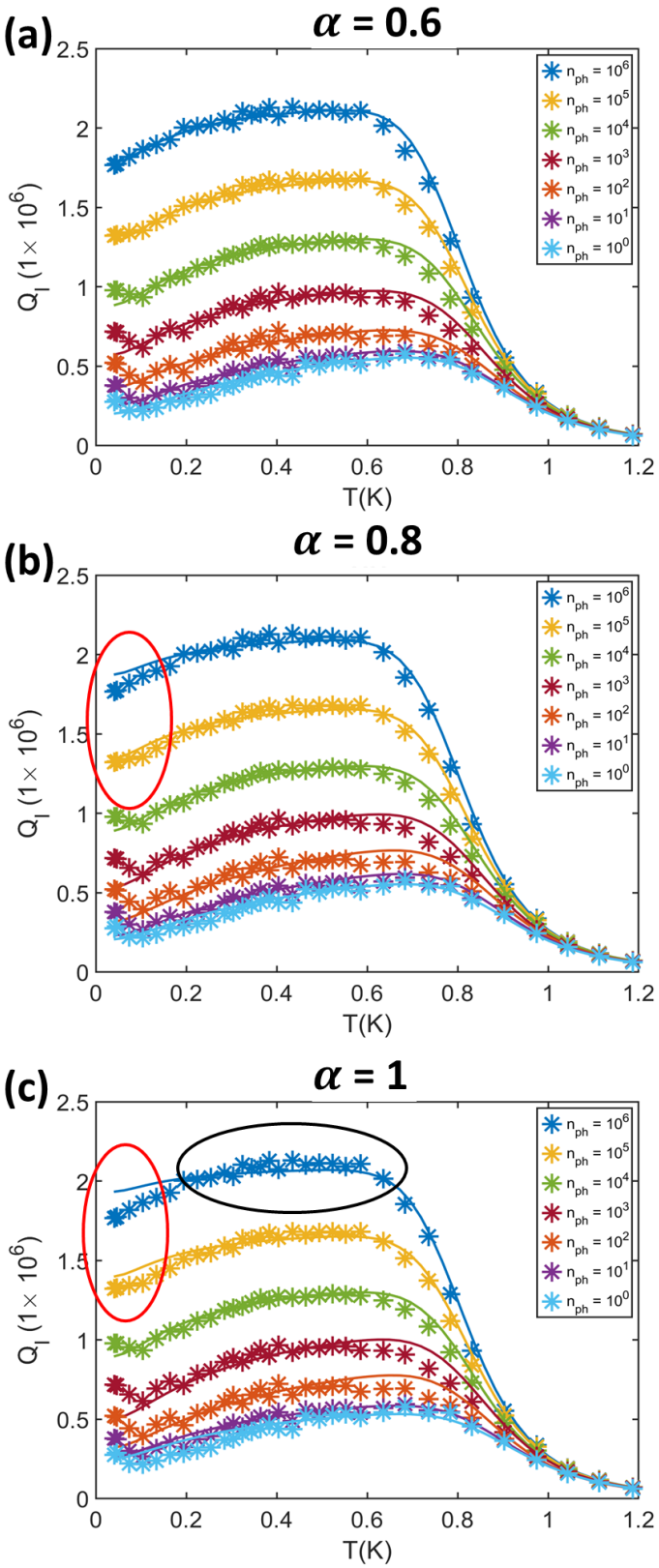


*Fig. 6.8: Impact of varying α on the fits. (a) is the reference fits with best-fit values for all parameters. (b) and (c) correspond to the fits with fixed $\alpha = 0.8$ and $\alpha = 1$ respectively.*

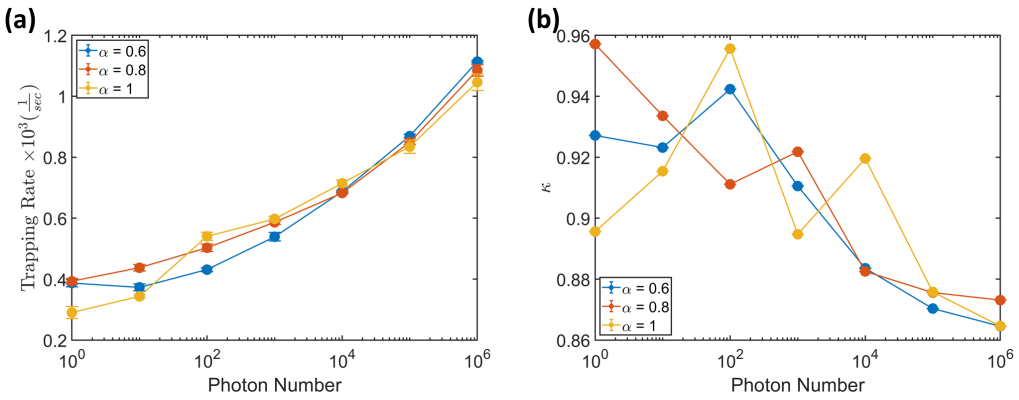


*Fig. 6.9: Extracted trapping rate and κ for different fits. The lines are guide for eye.*

Now, comparing these results with a TLS only model described in Eq. (5.6), the value of $\alpha$ extracted at low temperatures is lower than that of $\alpha$ extracted from the current model. A comparison of the extracted values from both the fits is presented in

Table 6-2. For these TiN resonators, a calculation of contribution from quasiparticle loss at a low temperature helped in better estimation of TLS parameters that are consistent with a complete data set of measurements of resonator behavior at different temperatures and powers.

*Table 6-2: Comparison of power dependent TLS only model and power-temperature dependent TLS-QP model*

| Parameter | Standard TLS power fit at lowest temp | Proposed TLS – QP power- temperature fit |
|---|---|---|
| $\alpha$ | 0.28 | 0.6 |
| $Q^o_{TLS}$ | $2.1\times10^5$ | $2.2\times10^5$ |
| $n_c$ | 0.01 | 5.1 |

## 6.2 *Aluminum resonators*

Next, I used the power-temperature model to analyze the aluminum resonators. These resonators were measured for microwave power corresponding to photon numbers ranging from $10^0$ -$10^6$ at temperatures 40 mK to 320 mK at steps ranging from 30-50 mK. The critical temperature of these resonators was 1.2 K.

I only present the data for one of the resonators, Al-R04. First, comparing the individual $S_{21}(f)$ fits for all temperature and power. The extracted $Q_C$ from individual $S_{21}(f)$ at different powers and different temperatures is presented in Fig. 6.10. The variation in the $Q_C$ does not have a clear trend similar to that of the TiN resonator, with greater variation at low photon numbers and higher temperatures. Similar to TiN, I chose a constant $Q_C$ of 151,000 and refit the whole data to extract other resonance parameters.

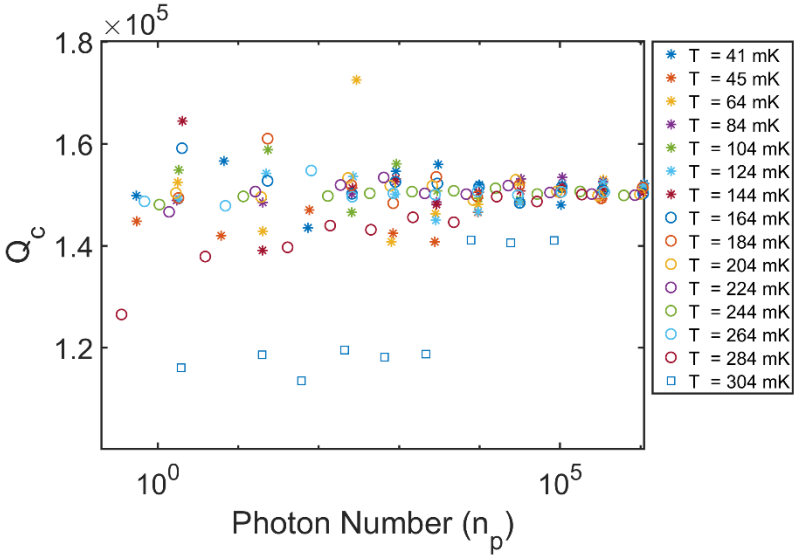


*Fig. 6.10: Coupling quality factor $Q_C$ the resonator Al-R04 versus photon number at different measured temperatures from individual S21 fits for non-fixed $Q_C$.*

Fig. 6.11 shows the temperature and power variation of extracted $f_o$. Similar to the TiN resonator, this resonator also shows a temperature dependence of resonant

frequency with temperature due to the increased participation of thermal quasiparticles. The relative variation of resonant frequency for the whole data is 8.3e-6. Similar to the case of the TiN resonator, I have used a constant frequency, $f_0$, 5.25086 GHz.

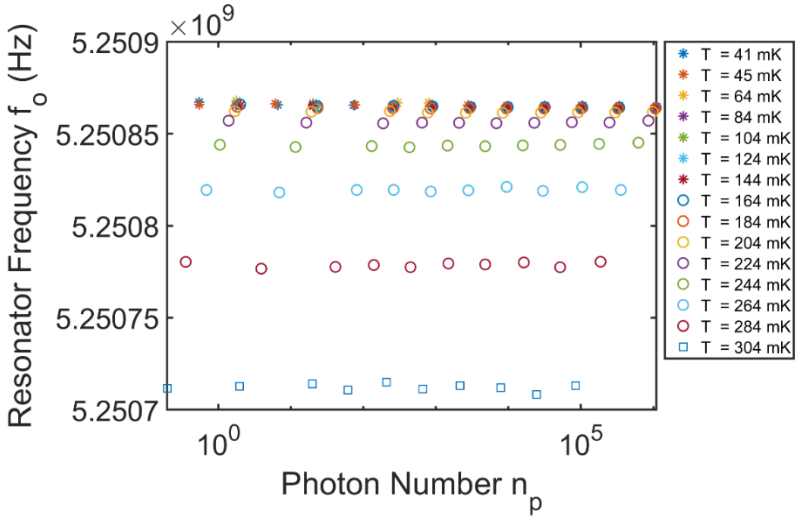


*Fig. 6.11: Resonant frequency of the resonator Al-R04 versus photon number at different measured temperatures.*

The measured single-photon quality factor at the lowest bath temperature of 40 mK is 412,000. The power and temperature dependence of $Q_I$ was further analyzed with my model. Fig. 6.12 presents the data and its corresponding fit for the photon numbers 10 and $10^5$. For this aluminum resonator, unlike TiN, $Q_I$ was relatively flat at low temperatures for both low and high photon numbers. As the critical temperature of Al is lower than TiN, thermal quasiparticles appear at lower temperatures than that of TiN, leaving a smaller transition region between thermal and non-equilibrium behavior compared to TiN. The fits for both powers track the data well, capturing the transition region better than TiN. The TLS loss contribution (purple dash curve) and quasiparticle losses (green dotted curve) show that the significant non-equilibrium QP is dominant

at low temperatures compared to TLS loss. Additionally, similar to the TiN resonator, both TLS and QP losses decrease with increasing power. Saturation of QP loss below 150 mK leads to the saturation of the effective quasiparticle temperature $T_{qp}$ around 225 mK. This value is close to some values reported in the literature, although a different method was used[89], [133].

The complete data and its corresponding fits are presented in Fig. 6.13. Fig. 6.13(b) presents the quality factor measured at different microwave powers at different temperatures. Similar to what I found in the TiN resonator, $Q_I$ increases with power for all temperatures. The data and the fits for all the photon numbers are presented in Fig. 6.13(a). The fits track the data for all powers. The extracted parameters from the fit are presented in Fig. 6.14. The quasiparticle trapping rate is calculated for the higher $I_{ext}$ compared to that of TiN. The trapping rate can be expressed in a phenomenological relation in $n_p$ as $s(n_p) = 10^4 \left(0.14 \left(\log(n_p)\right)^2 + 0.66 \log(n_p) + 1.089\right)$ and $\kappa$ can be expressed as $\kappa(n_p) = \left(0.0114\left(\log(n_p)\right)^2 + 0.0144 \log(n_p) + 1.968\right)$. I applied the calculated power fits to data at all temperatures from the extracted parameters, which are presented in Fig. 6.13(b). The improved temperature fit in intermediate temperatures for all powers is reflected in the improved power fits for intermediate temperatures above T>150 mK to T< 250 mK. Fig. 6.15 presents the calculated $T_{qp}$ and $n_{qp}$ for the whole temperature region at different powers.

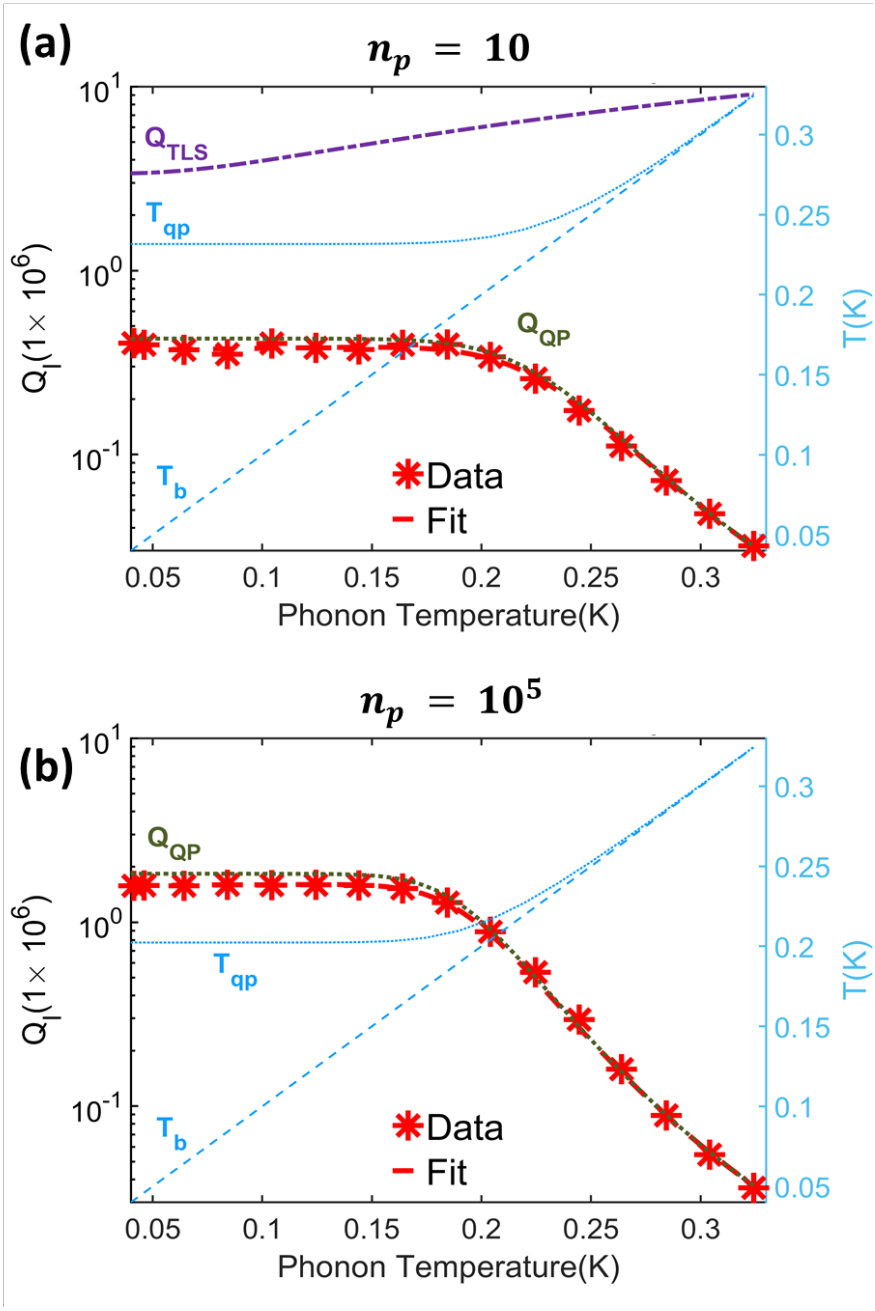


*Fig. 6.12: The fit results of the power-temperature fit on Al-R04 with individual components for data collected at low (a) and high (b) powers*

A significant difference between the TiN resonator and Al resonators can be seen by comparing the extracted $\kappa$ values. For the aluminum resonator, the extracted values of $\kappa$ is close to two. This signifies more quasiparticle loss than predicted by the thermal approximation, assuming that the $T_C$ is the measured value of 1.2K. For $\kappa >$

1, the quasiparticle distribution described by a thermal distribution underestimates the loss, and it requires an increased value of $\kappa$ to predict loss. An athermal effect is the power dependence of $Q_I$ at high temperatures. At temperatures T > 0.3 K, where thermal QPs dominate the loss, the quality factor increases with power. The redistribution of QPs from the bandgap edge in the presence of high microwave power explains this behavior[49]. This increase in $Q_I$ with power is also observed in the TiN resonators for T > 1.1 K.

It is important to note that adjusting $T_C$ of the film in the model impacts the extracted value of $\kappa$. Reducing $T_C$ from 1.20 K to 1.14K brings the value of $\kappa$ closer to 1 within 1-2 %. This change in $T_C$ is equivalent to a change in total bandgap ($2\Delta$) by 18 $\mu eV$(5%). The $T_C$ of 1.14 K is still a valid critical temperature for the aluminum film. One of the reasons for the difference between DC measured $T_C$ predicted by resonator measurement can be a measurement error as the stage thermometers are not colocated with the measured sample, causing a disagreement in measured and actual temperature. This significant variation in $\kappa$ is more prominent for low bandgap superconductors as for a given quasiparticle density gets more sensitive to the variation of $T_c$ as $T_c$ reduces. The deviation of $\kappa$ from 1 also impacts the calculated $T_{qp}$ and $n_{qp}$ values. The variation in $T_{qp}$ is of the order of 10-15 mK.

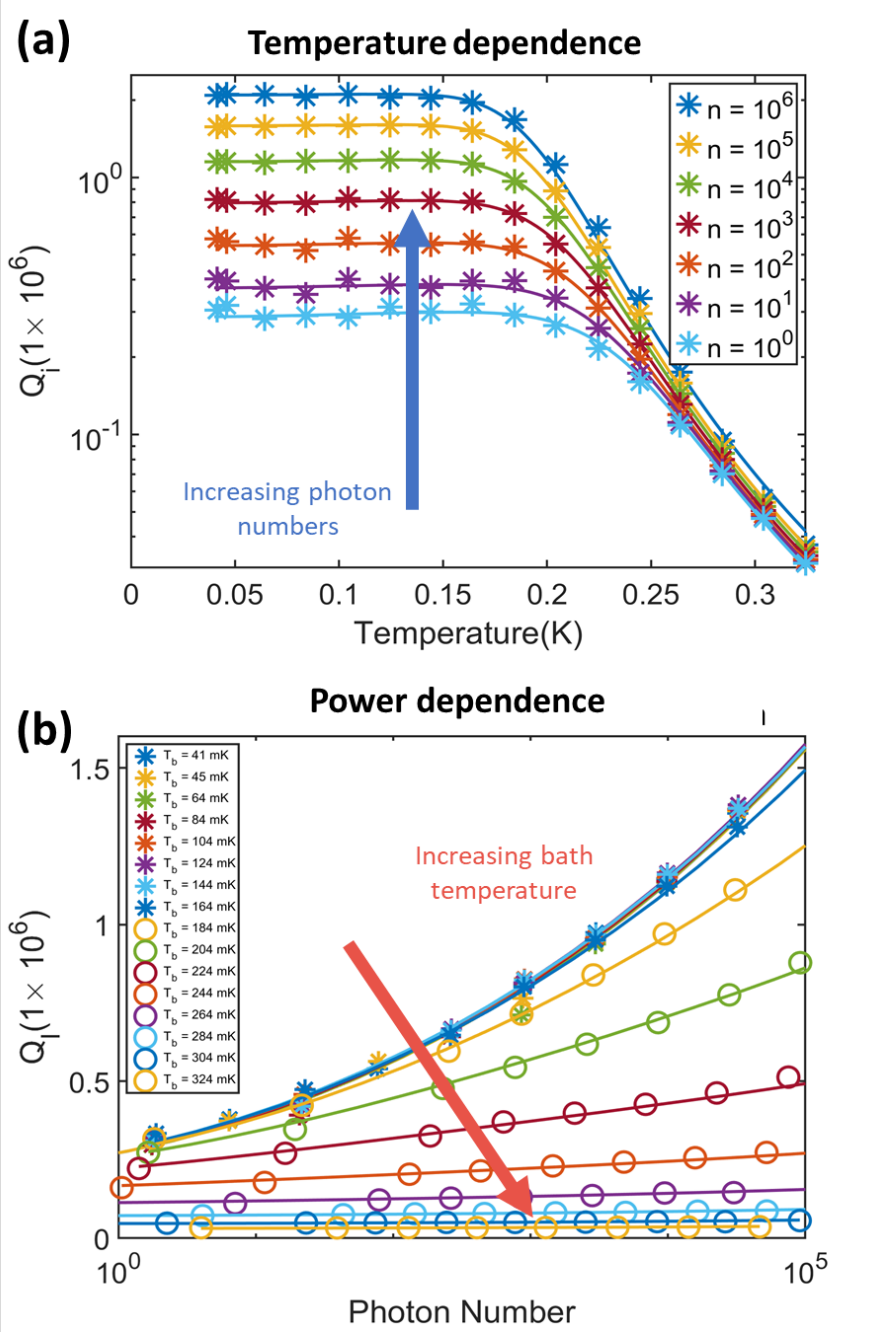


*Fig. 6.13: Data (symbols) and fits (curves) for (a) $Q_I$ versus temperature (b) $Q_I$ versus power for complete dataset for the Al-R04 resonator*

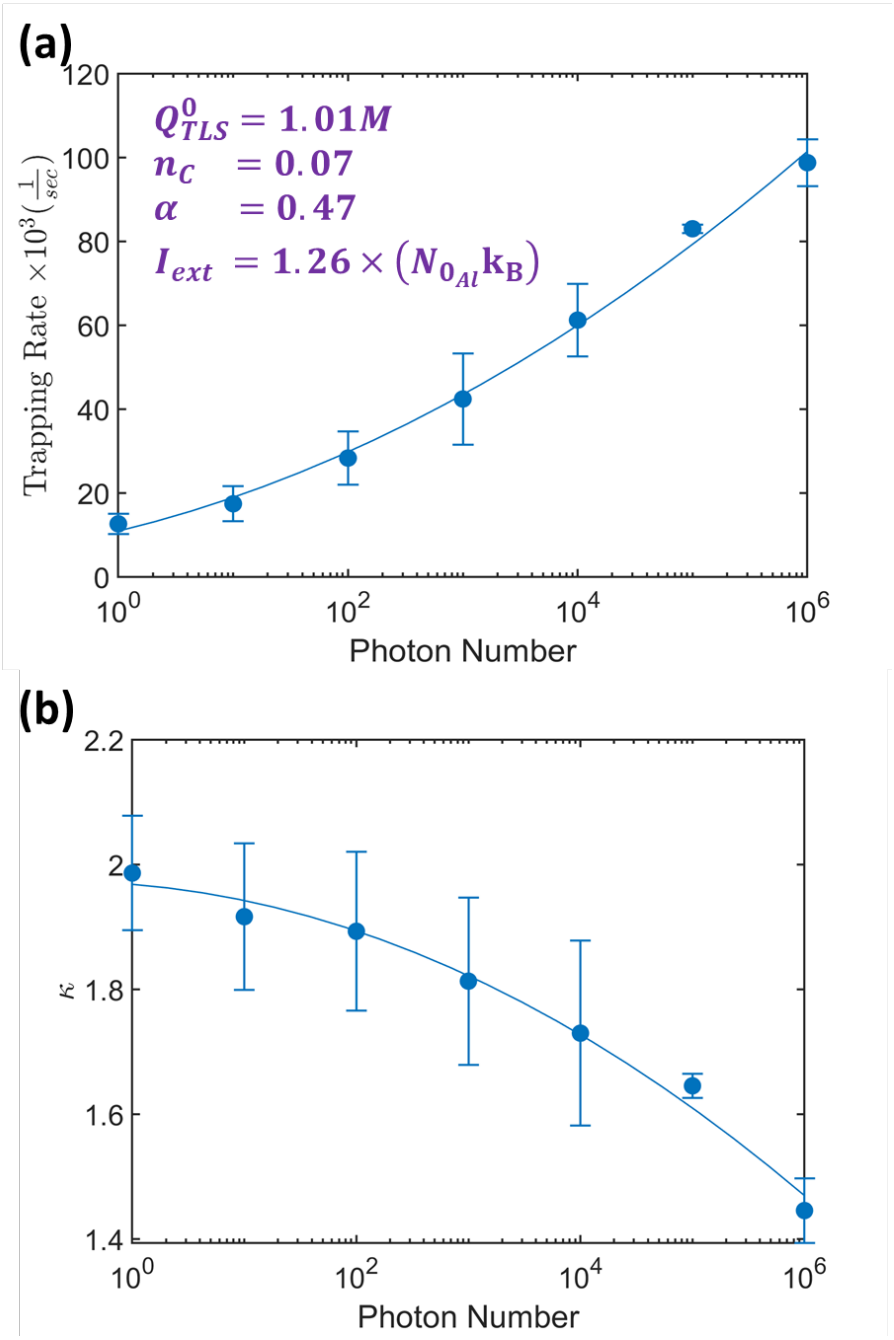


*Fig. 6.14: Extracted parameters for (a) trapping rate s vs. photon number (b) κ vs photon number Al-R04 resonator.*

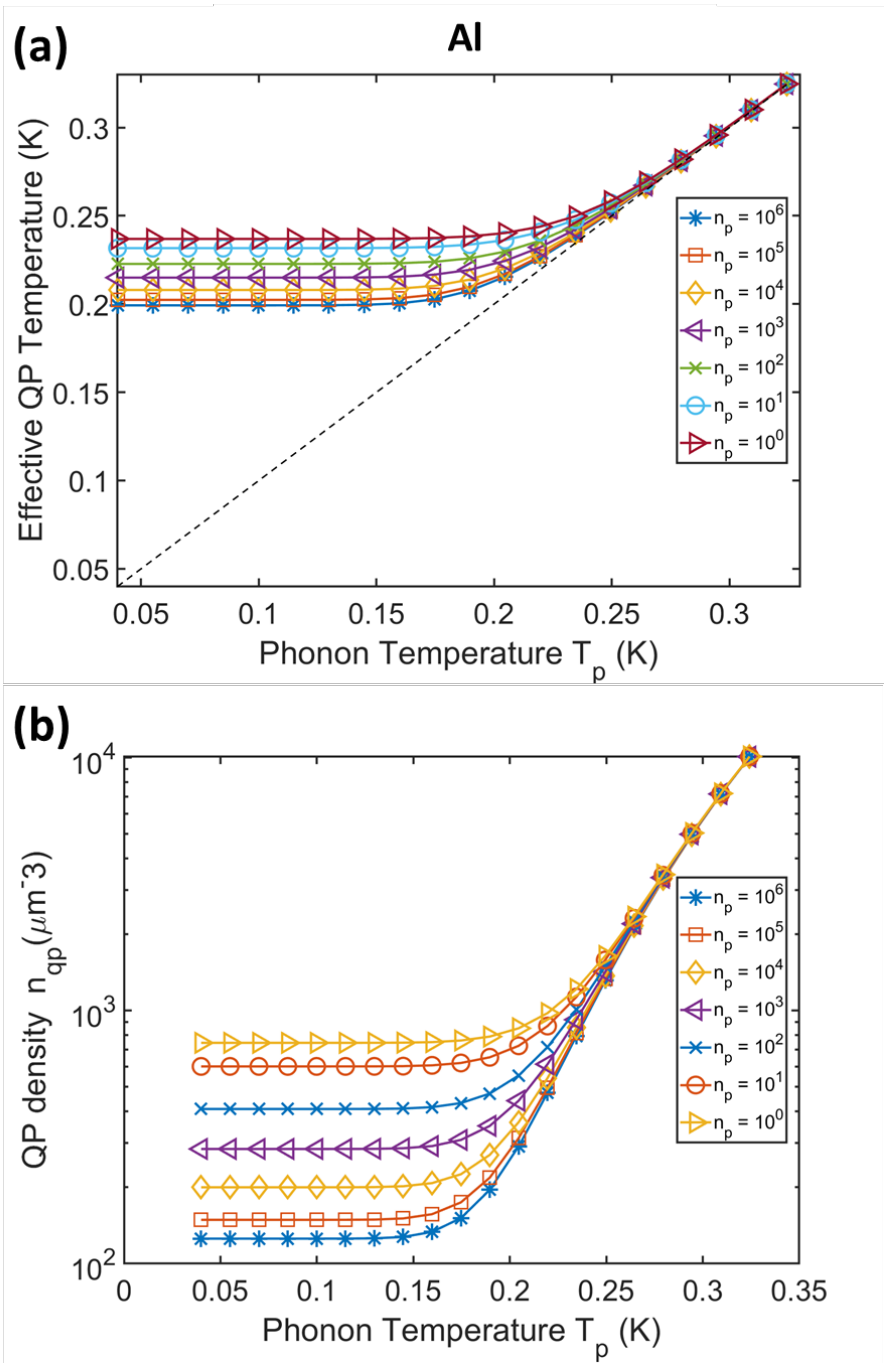


*Fig. 6.15: Plot of (a) quasiparticle temperature versus phonon temperature (b) quasiparticle density versus phonon temperature for Al-R04 resonator.*

The overall TLS contribution is low for this resonator, making it challenging to extract the TLS properties accurately. On the other hand, a complete quasiparticle loss can describe $Q_I$ trend of this resonator. Hence the data was refitted with pure QP loss, and

the comparison between the two scenarios is presented in Fig. 6.16. The comparison shows a negligible difference between the two fits. The impact of the change in $Q_{TLS}^{0}$ change in trapping rate, s, and $\kappa$ as shown in Fig. 6.17. Hence the loss, according to my model, the loss in this resonator can be described as dominated by the non-equilibrium quasiparticles.

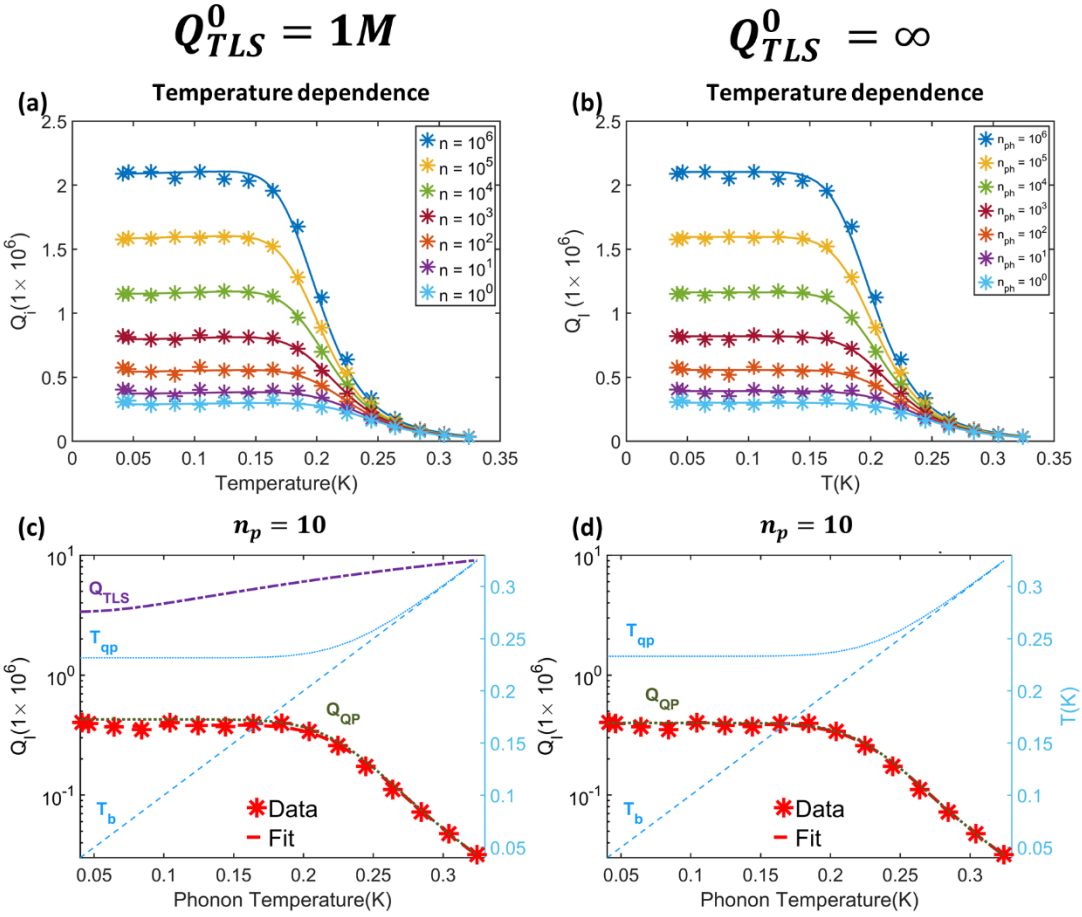


*Fig. 6.16: Comparison of change of $Q_{TLS}^{0}$*

The major takeaway of applying this power-temperature model is to isolate loss contributions between non-equilibrium quasiparticles and TLS at low temperatures with a simpler model. It provides a better estimate of primary loss mechanisms hampering the device at low temperatures. Here quasiparticle poisoning is the dominant

loss mechanism in aluminum resonators, whereas, in titanium nitride resonators, both TLS and quasiparticles significantly contributed towards loss. Since the non-equilibrium quasiparticles contribute towards loss, one of the ways to mitigate the loss by modifying the resonator design using quasiparticle traps was explored.

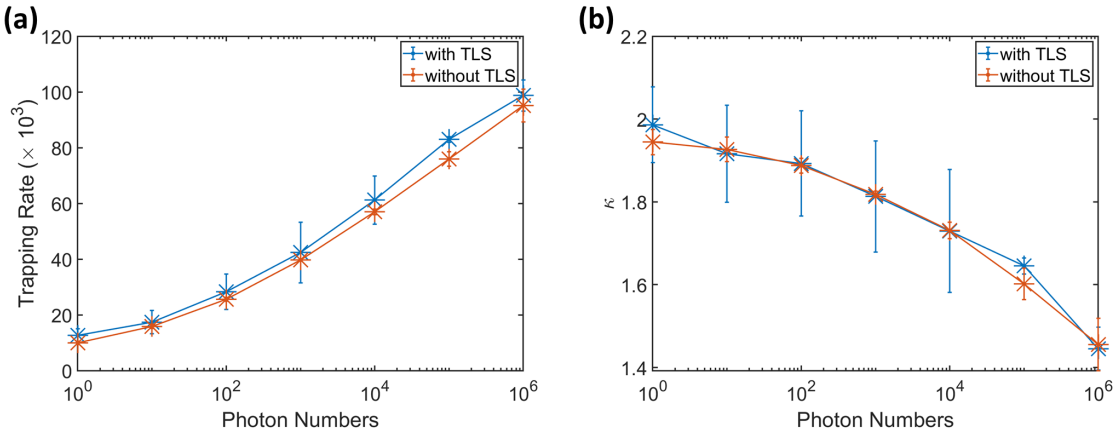


*Fig. 6.17: Comparison of trapping rate s and κ*

## *6.3 QP trap resonators*

In this section, I discuss my results on 16 resonators from two chips. These resonators had eight different setbacks. Each resonator was measured for photon numbers $10^0$-$10^6$ from temperature 40 mK to 1.25K. For this temperature range, the aluminum layer is superconducting as the critical temperature measured for the bilayer was 4.47K. The best performing resonators for each setback were selected from the lot. Unfortunately, the resonator with a setback of 50 µm suffered a tweezer scratch. The devices with setbacks, $s_b$ =2, 20, 100, and 150 µm, were from one chip D1, while the other three, $s_b$ =1, 5, and 10 µm, were from a second chip D2. Table 6-3 presents the device ID, coupling quality factor, and resonant frequency of each device. The complete dataset for all resonators for different trap devices is presented in Fig. 6.18 a-

e. The red datasets correspond to the setbacks less than 20 µm while blue corresponds to the other set. These resonator performances were compared with the reference TiN resonator, which is plotted in black circles.

*Table 6-3: Device ID, coupling quality factor $Q_C$ and resonant frequency $f_O$ of different trap devices*

| $s_b$(µm) | Device-ID | $Q_C$ | $f_o$(GHz) |
|---|---|---|---|
| 1 | D2-R01 | $1.532\times10^5$ | 4.4255 |
| 2 | D1-R01 | $2.793\times10^5$ | 4.4195 |
| 5 | D2-R03 | $1.057\times10^5$ | 4.6927 |
| 10 | D2-R04 | $1.592\times10^5$ | 4.8358 |
| 20 | D1-R02 | $1.677\times10^5$ | 4.5625 |
| 100 | D1-R06 | $1.083\times10^5$ | 5.2401 |
| 150 | D1-R05 | $1.978\times10^5$ | 5.1564 |

Resonators with setbacks, $s_b$=2, 20, 100, and 150 µm has shown greater quality factors than the reference TiN resonator for lower temperatures. The device with $s_b$=150 µm has almost 50% more than the quality factor than the reference TiN resonator for most photon numbers at low temperatures. These results suggest that the low bandgap superconductors reduce the quasiparticle number through trapping. The low number of averages completed during data collection at low photon numbers for resonators with trap led to noisier data. This issue was corrected for TiN resonators, with the increased averaging at low photon numbers to reduce the noise in the data.

To further analyze these devices, the power and temperature model was applied to each trap device. The first requirement of the temperature and power model was the critical temperature $T_C$ of the film. The presence of an aluminum layer as a trap in the ground plane of the resonator modified the $T_c$ for the resonator. This causes the difference in the rate of drop of $Q_I$ at high-temperature regions. The proximitized Al trap layer had a critical temperature of 4.47 K.

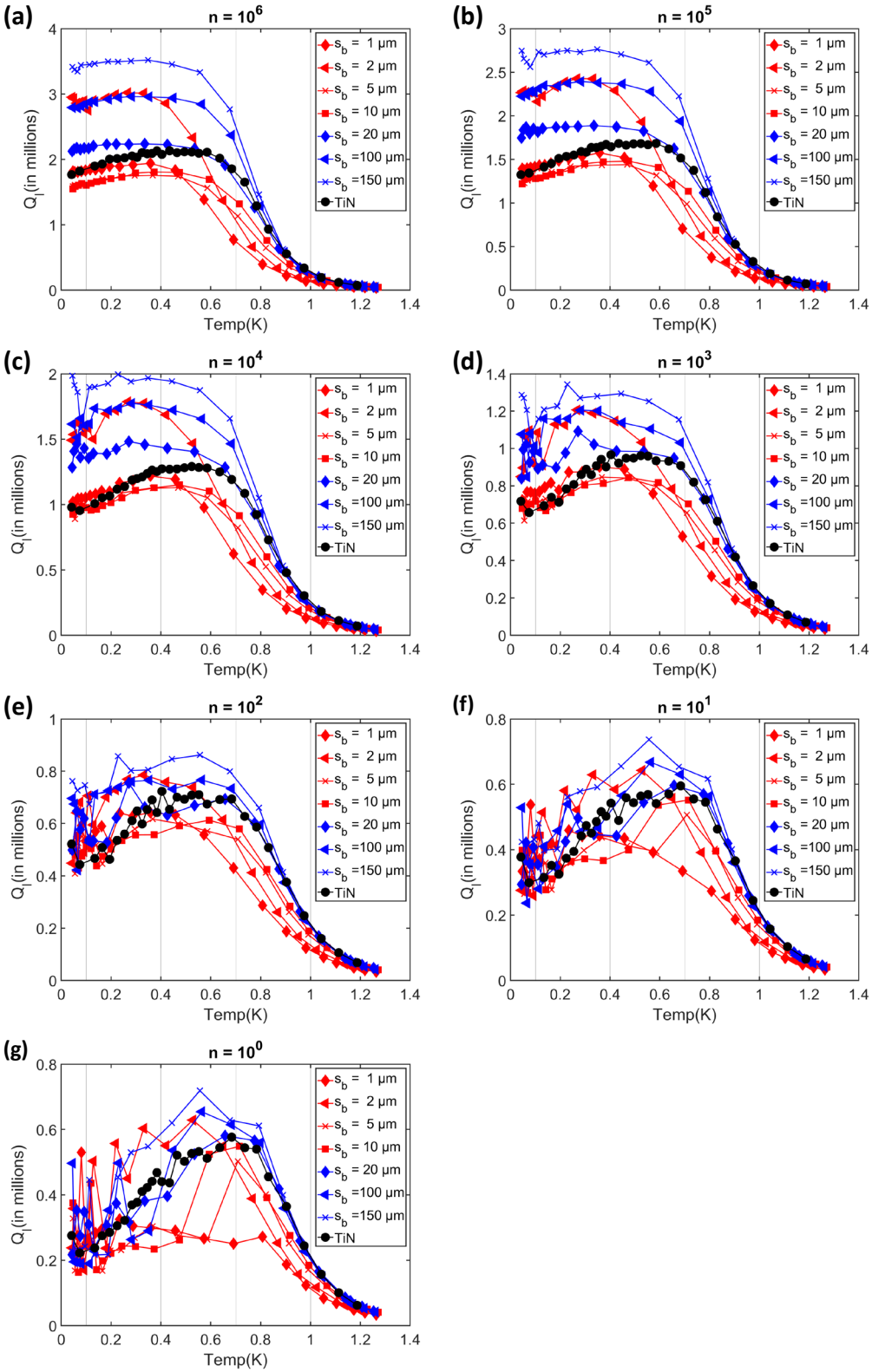


*Fig. 6.18: Temperature dependence of resonators measured at different power. The limits on the y-axis of each panel are different for ease in comparison for individual power values.*

But Al does not uniformly cover the TiN throughout for the resonators with a setback. The central conductor of the resonator and portion of the ground plane is free from any Al. Therefore, finding an exact critical temperature describing the resonator was challenging.

For my model, for a single film TiN resonator TiN-R02, $\kappa$ was found to be close to 1. In the model, $\kappa$ is a free parameter that tries to capture any athermal behavior. Assuming that the athermal contributions are low, setting $\kappa$ to 1 and treating $T_C$ as a fit parameter gives an estimate for how $T_c$ depends on different setbacks. To verify the impact of setting $\kappa$ to 1, first, I reanalyzed the reference TiN resonator with $\kappa = 1$. The TiN fits with DC measured $T_C = 5.3$ K has $\kappa$ varying about $0.9 \pm 0.05$ as shown in Fig. 6.6. With $\kappa = 1$, I refit the data using variable $T_c$. An average of $T_C$ predicted by different temperature fits, gives a $T_c$ of 5.36 K. Using this $T_c$, the new fits for all photon powers with $\kappa = 1$ were performed which are presented in Fig. 6.19(b). Comparing these results with the original fit (Fig. 6.19 (a)), the new fits are similar to the older fits. The extracted parameters are presented in Fig. 6.20. The change in $T_C$ has not impacted the extracted TLS parameters, although the trapping rate has increased to compensate for higher $\kappa$ for higher powers.

Since fixing $\kappa$ didn't adversely affect the fits, $T_c$ is extracted similarly for all trap devices by holding $\kappa$ to 1. The extracted $T_c$ is shown in Fig. 6.21. $T_c$ varied from 5.1 K for $s_b = 1$ μm to 5.38 K for $s_b = 150$ μm. The fits with extracted $T_c$ were applied to all the trap devices. Fig. 6.22 presents the fit results for all the setback devices, and Fig. 6.23 captures the extracted parameters. For TLS parameters, the reference TiN resonator values are expressed as a continuous line. For the equal comparison between

the devices, the external generation rate ($I_{ext}$) was kept same as that was used for TiN at $0.15\times N_{o,TiN} \times k_B$ where $N_{o,TiN}$ is the single electron spin density states of the TiN.

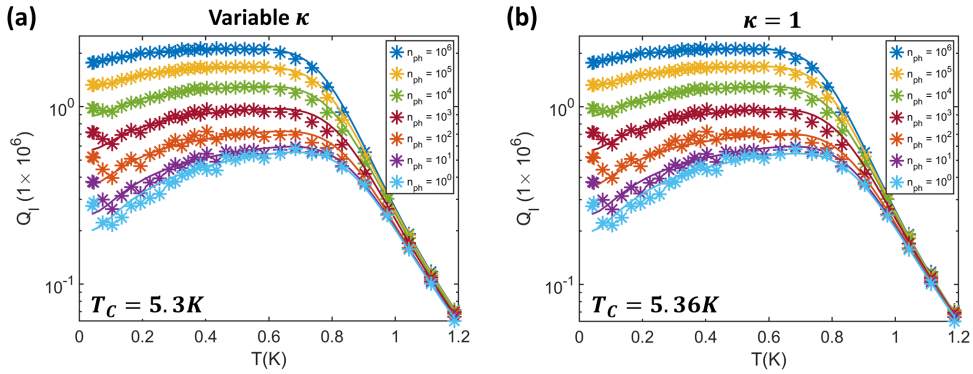


*Fig. 6.19: Comparison of fits for* $\kappa = 1$ *with variable* $\kappa$

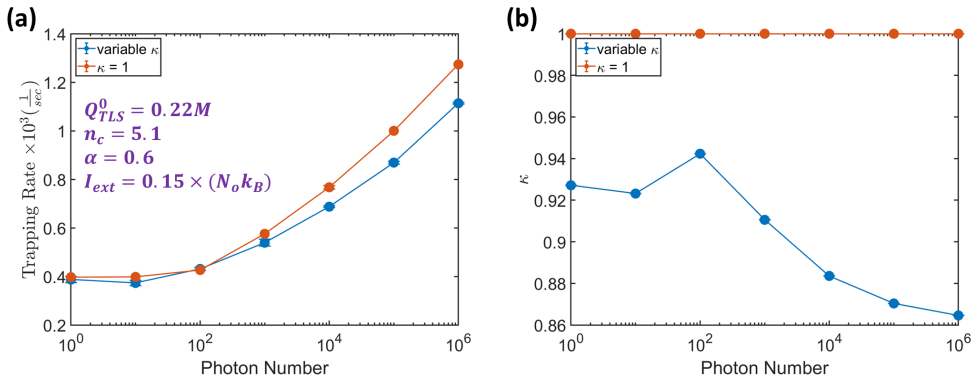


*Fig. 6.20: Temperature fits for TiN with the* $\kappa$ *held at and* $T_c$ *changed to 5.36K*

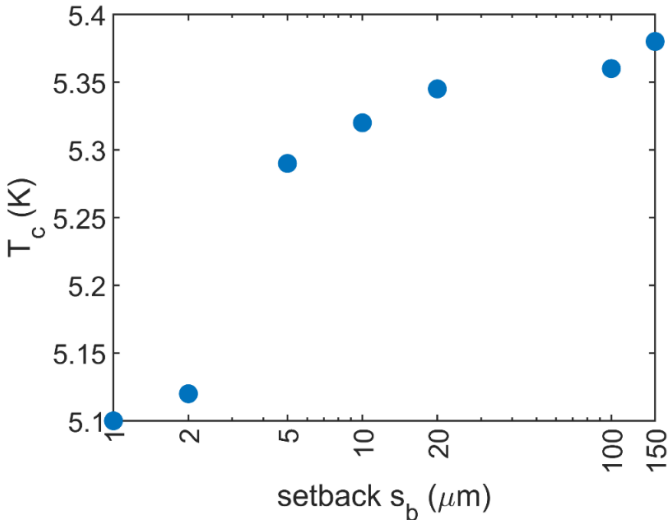


*Fig. 6.21: Extracted* $T_c$ *for different trap devices*

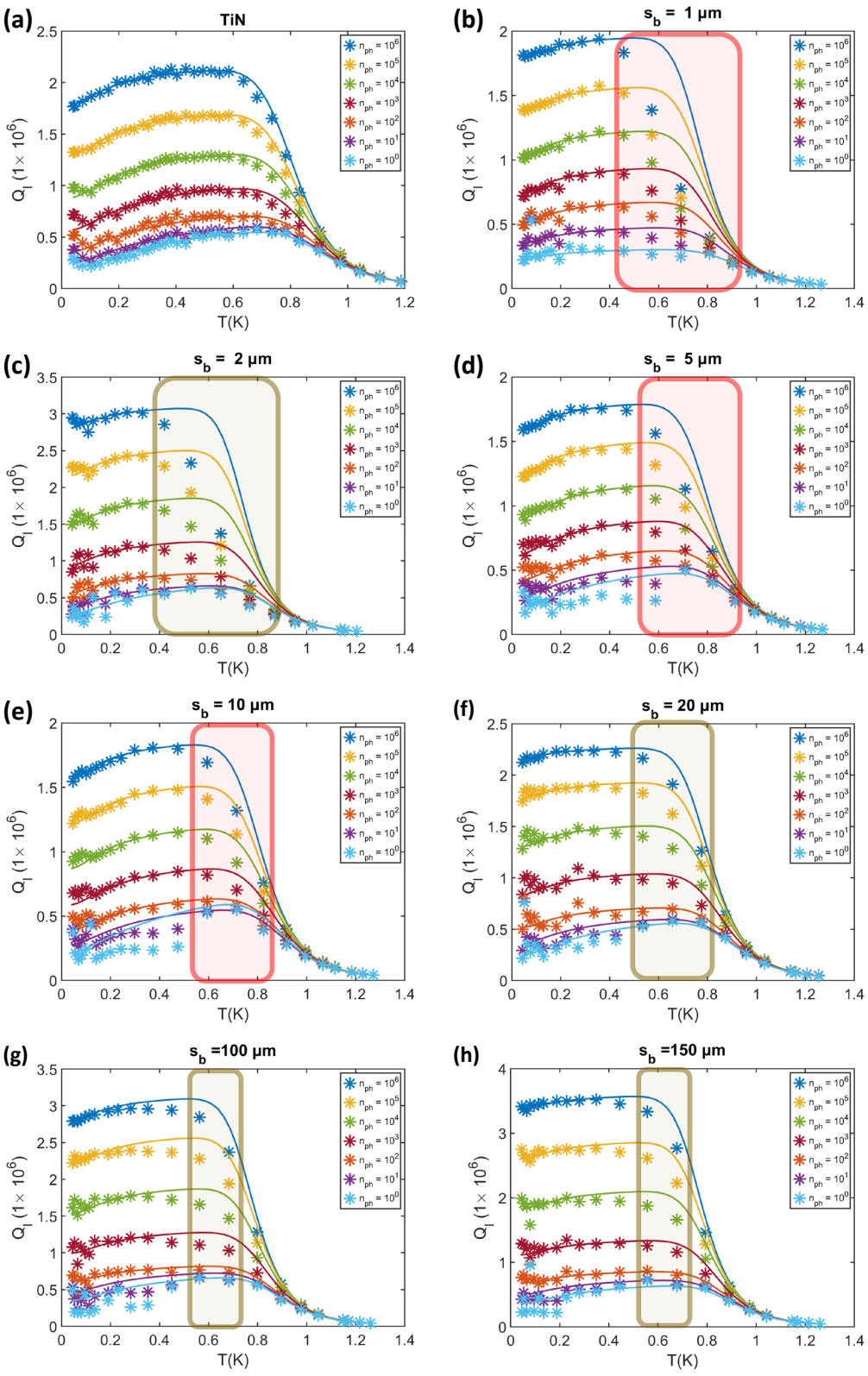


Is

*Fig. 6.22: Summary of the fits for all setbacks with the reference TiN data. The highlighted region shows the temperature region where fit doesn't track data well. The devices having red highlight are from one die, while yellow is from another die.*

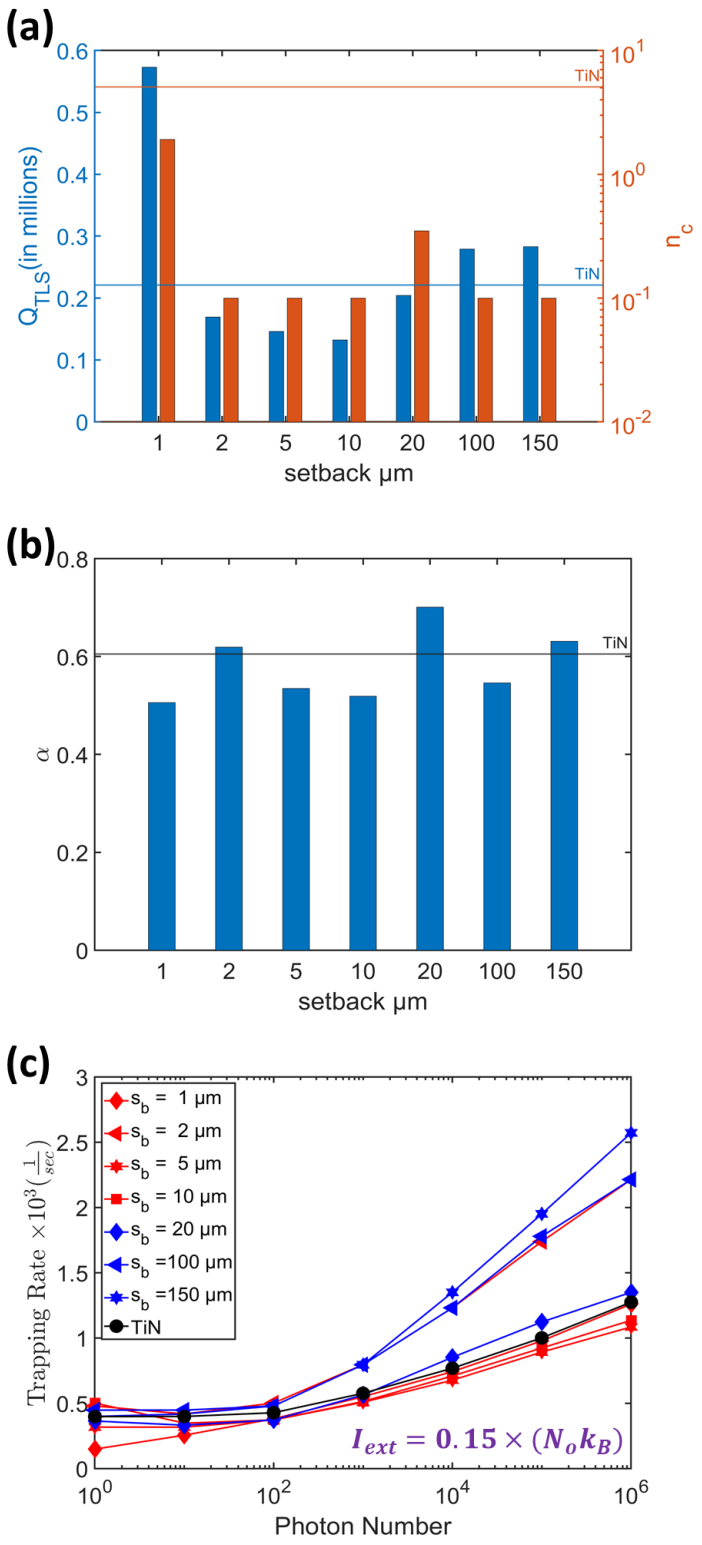


*Fig. 6.23: Comparison of extracted parameters (a) $Q^0_{TLS}$ (blue) and $n_c$(orange) versus setback (b) α versus setback . Black line is for reference TiN-R02 (c) trapping rate,s versus power for different setback. Black curve corresponds to TiN-R02.*

The fit curves in Fig. 6.22 perform reasonably well for the high setback devices with minor overestimation of $Q_I$ around the transition temperatures from TLS and non-equilibrium QP regime to the thermal QPs regime. For low setback devices, the fits grossly overestimate $Q_I$ at the transition temperatures. The overestimation of $Q_I$ gets worse as the power increases. The region of poor agreement is highlighted for each device. None of the trapping rate,$s$, and external generation rate,$I_{ext}$, combinations can track the data well, indicating a loss behavior that the present TLS-QP power-temperature model cannot capture.

The possible reason for this discrepancy could be an attempt to capture the net quasiparticles from both trap and superconductor with a single $T_C$ for the whole device. The quasiparticle number density has an exponential dependence on critical temperature $T_C$ given by Eq. (2.4). The trap region with a low bandgap ($T_c$ = 4.47 K) generates a significant number of thermal quasiparticles, which starts dominating the loss at a much lower temperature than the higher bandgap material ($T_c$ = 5.3 K). Hence the low setback devices, which have a significant percentage of ground plane area covered by the trapping layer than large setback devices, have considerable losses earlier in temperature. A possible two-temperature QP model is required to model this loss with their contributions defined according to the device geometry. This modification has not been attempted and is left for future work.

Even though the high-temperature region fits don't perform well, fits perform well for the low-temperature region, dictated by the TLS defects and the non-equilibrium QPs. At low temperatures (T < 0.15 K), the TLS thermal signature, which has increasing $Q_I$ with increasing temperature, can be observed for all devices. The

extracted trapping rate for different powers for the varying setback is presented in Fig. 6.23(c). The extracted values at photon number $n_p < 10^3$ may be affected by the noise in the measured spectrum that results in increase uncertainty of the extracted value of $Q_I$. But for higher photon powers, the trapping rate follows a similar trend as $Q_I$ for all devices. The devices with greater overall $Q_I$ have a larger trapping rate(s) for a fixed quasiparticle generation rate ($I_{ext}$). As the fits near intermediate region are not so good, the extracted trapping rates may not be an accurate measure of the actual trapping rate.

For ease in comparison, quality factors at constant power for specific temperatures are interpolated and plotted against the setback distances. It is presented in the first column of Fig. 6.24. A set of quality factors at constant temperatures (0.1, 0.4, 0.7, and 1K) is plotted for different powers ($10^3$-$10^6$) for all the devices. The reference TiN data is presented as a continuous line. Each color represents a specific temperature, and each symbol represents a specific power. The data is further refined by removing the TLS participation from each $Q_I$ and resultant $Q_{QP}$ at various temperature and power is displayed in the second column of Fig. 6.24. For high temperatures and higher power, TLS has a negligible contribution and hence $Q_{QP}$ is almost the same as $Q_I$.

At T = 100 mK, the devices with setback $s_b$ > 10 μm outperform TiN, while devices with $s_b \leq 10$ μm have lower $Q_{QP}$ except for the outlier $s_b = 2$ μm for all power levels. The higher quality factor for all trap devices indicates the effective trapping of athermal quasiparticles by the low gap superconductor. The setback with $s_b$ = 150 μm outperforms all of them.

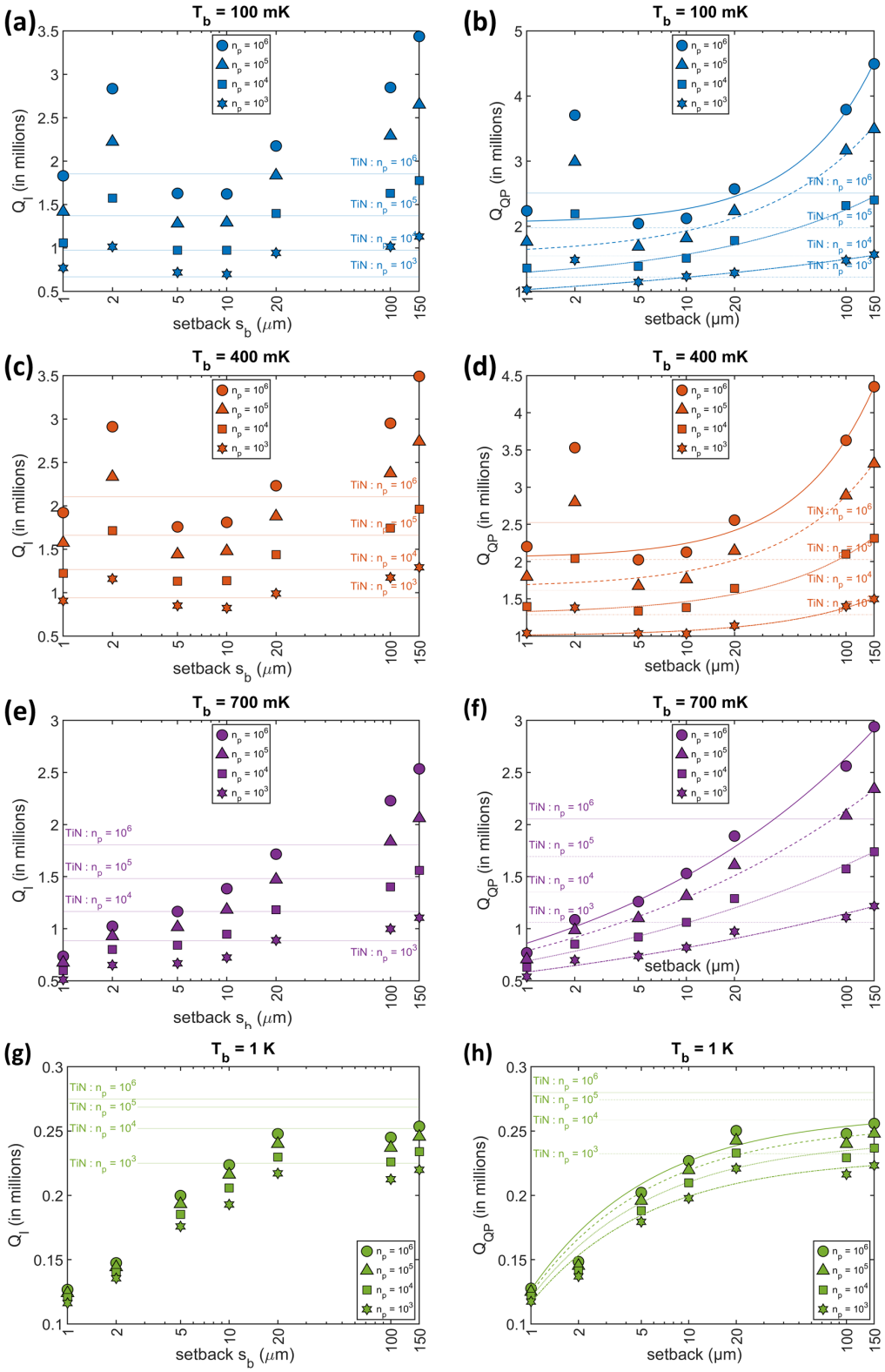


*Fig. 6.24: First column((a),(c),(e),(g)) shows plots $Q_I$ vs setback at different temperatures for different powers. Second column ((b),(d),(f),(h))) presents the corresponding $Q_{QP}$ with a phenomenological fit to map the dependency of $Q_{QP}$ on setback $s_b$.*

While at 1K, almost all the resonators with setbacks perform poorly compared to the titanium nitride. The increased participation of thermal quasiparticles from the low superconducting gap regions leads to higher losses in trap devices. The overtake of TiN resonator over trap devices at high temperatures is foreshadowed even at intermediate temperatures regions. The low setback devices are the first to fall behind TiN compared to the larger setback devices. At 400 mK, $s_b \geq 20\ \mu m$ performs better than TiN while at 700 mK, $s_b \geq 100\ \mu m$ performs better than TiN for all power levels. This trend can be observed more clearly in the temperature dependent plots of different trap devices in Fig. 6.18. At the temperature region between (400 – 900 mK), all trap devices with $s_b$ < 20 μm, have a similar trend in that the quality factor falls much faster than the TiN device. The onset of significant thermal quasiparticles from the trap regions hampers its functionality as a quasiparticle trap, and it can be argued that the low bandgap region functions as a trap for non-equilibrium quasiparticles.

Additionally, $Q_{QP}$ for all powers and temperatures is fitted with a phenomenological power function $a(s_b)^b + c$ to capture the trend as a function of the setback. Since at low temperatures, as $s_b = 2\ \mu m$ does not follow the trend, it is ignored during the fit. The power and temperature dependence of the parameters $a, b, c$ is presented in Fig. 6.25. For 100 mK, the rate of increase of $Q_I$ with setback is faster at the high powers indicating higher trapping with increased power. It is captured by an increase of $b$ with photon number. Even though the at 400 mK, $Q_I$ increases with setback, the rate of increase are almost similar for all photon numbers, which makes $b$ almost constant. This trend continues for higher temperature with a value of $b$

eventually becoming negative, indicating the saturation of the $Q_{QP}$ with increasing setback.

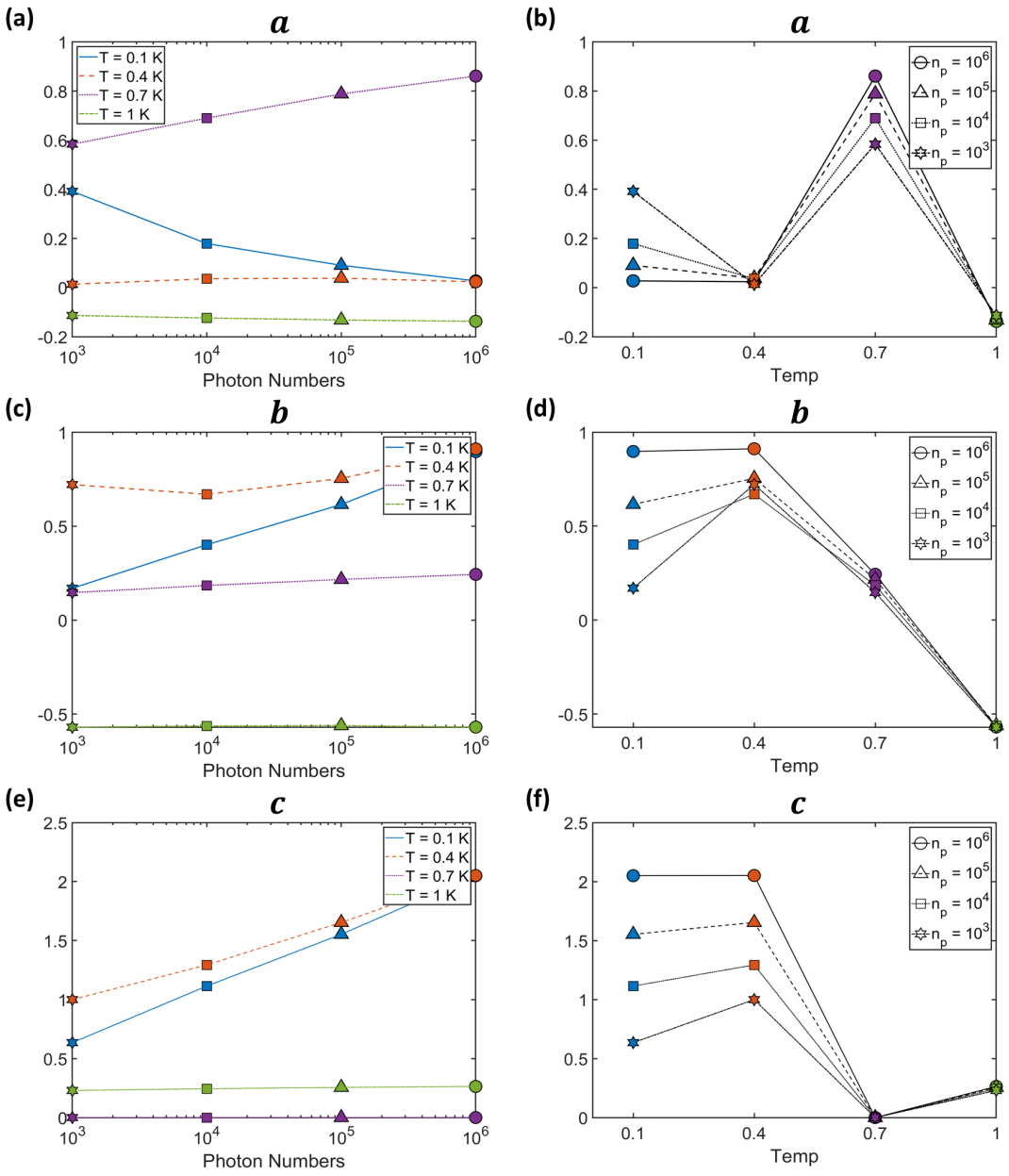


*Fig. 6.25: Power and temperature dependence of fit parameters of the fit on $Q_{QP}$ vs $s_b$ using a phenomenological relation $as^b + c$*

It is worthwhile to note that all the better-performing devices are from the same chip. Probably the chip-to-chip variation in packaging might have an impact on the comparison between the devices. A larger statistic would help to capture the trend better. The outstanding performance of $s_b = 2\ \mu m$ may not be an anomaly. An estimate of quasiparticle diffusion length ($L_d \sim \sqrt{D_{qp}\tau_{qp}}$ ) from the literature values is around $10\mu m$ [117], [119]. Hence there is a high chance that the quasiparticles move ballistically rather than diffusive process from high field region near the ground plane of the resonator. Hence the small setback devices need to be investigated more to understand their trapping efficiency.

Overall, the quasiparticle trapping performed well for larger setbacks at low temperatures. This trend is opposite to the simulation using the FDM QP trap design model. Fig. 4.6 shows the decreasing quasiparticle density with decreasing setback. The FDM model assumed the quasiparticle source close to the ground plane edge. The model needs to be modified to include the uniform QP source, not at the ground plane edge, which might help to match the observed trend.

# Chapter 7 : Conclusions and future work

## *7.1 Conclusions*

In this work, I proposed a temperature and power dependent model of resonator quality factor that includes losses from TLS and quasiparticle for different power and temperature conditions. The model combined the conventional TLS power and temperature dependence with an effective temperature non-equilibrium quasiparticle description of the superconducting loss. The quasiparticle description is based on the quasiparticle number density calculated using rate equations for an external quasiparticle generation source, recombination, and trapping. The number density is translated to an effective temperature, $T_{eff}$ described by a thermal distribution that may be different than that of the bath. The effective temperature is applied to the CPW resonator-specific quasiparticle quality factor to calculate quasiparticle loss.

I applied the model to the titanium nitride and aluminum resonators. The TiN and Al resonators were fabricated from epitaxial MBE-grown high-quality film. The fabricated resonators had single quality factors of around $4\times10^5$ at the lowest bath temperatures and over a million at high powers. Applying the model on these resonators suggests a significant non-equilibrium quasiparticle contribution even at low bath temperatures. For the TiN resonator, the quasiparticle loss is comparable with TLS loss, while the quasiparticle loss dominates the Al resonator. For the TiN resonator, the value of $\alpha$ was 0.6. The reperformed fits with theoretical $\alpha$ (0.8 for CPW and 1 for single TLS) failed to capture the data well, suggesting that the extracted value of $\alpha$ was not consistent with the loss from a uniform distribution of TLSs. Lower $\alpha$ may be

consistent with the presence of multiple TLS sources varying critical photon number $n_C$, possible multiphoton effects activating an ensemble of TLS defects with different energies, or un-isolated contributions from the quasiparticle population. On the other hand, in the Al resonator, since QP loss dominates, the TLS parameters cannot be confidently extracted.

For TiN and Al resonators, $Q_{QP}$ increased with increasing microwave power. This increase in $Q_{QP}$ was associated with an increase in the quasiparticle trapping rate $s$ with increasing microwave power for a constant external generation rate $I_{ext}$. The interdependency of $I_{ext}$ and $s$ , makes it difficult to estimate their values uniquely. But it provides the trends for one of them if the other is kept constant. In total, although the effective temperature model leads to a thermal approximation of a non-equilibrium quasiparticle distribution, one strength of the approach is that it provides a way to predict quasiparticle loss along with other losses. The model tracks the data well for a single material system.

Additionally, I designed and measured high bandgap superconductor resonators with a low bandgap superconductor as a quasiparticle trap. The dependency of the overlayer distance from the resonator's active region was investigated using a finite-difference model by solving a combined model of excess quasiparticle, phonon temperature, and overlayer quasiparticle temperature. Based on the simulation results, the optical lithography masks were designed with setbacks varying from 1-150 μm. I fabricated the resonators using two-step optical lithography and measured their temperature and power dependence. All the fabricated resonators had a single photon quality factor above $3\times10^5$ at the lowest measured temperatures and a high power

quality factor above $1\times10^6$. Resonators with an overlayer performed better than the plain TiN resonator at low temperature and low power. Notably, the resonator with setback $s_b$ with 150 μm performed 1.5x than the TiN resonator at high power levels. Additionally, a lower setback of 2 μm also had 1.25x better $Q_I$ than TiN resonators at low temperatures.

I did the broad temperature and power dependence measurements to investigate the behavior of all the resonators. Devices with quasiparticle traps worked pretty much as expected for the low temperature, where non-equilibrium quasiparticles dominate over thermal quasiparticles. As the temperature increased, the thermal quasiparticles from the low bandgap overlayer started contributing to the loss outweighing the beneficial impact of the traps. The impact of the overlayer thermal quasiparticles was most prominent for low setbacks. I used a phenomenological model to capture the quasiparticle quality factor dependency on the setback for different temperatures and powers. The quality factor increased faster with an increasing setback at higher power than lower powers for low temperatures. This trend plateaus out as temperature increases.

Overall, I found that a low superconducting bandgap material acts as a quasiparticle trap for the resonators and improved performance. The largest setback performed best with an optimum balance of trapping and reduced thermal quasiparticle poisoning at higher temperatures.

## *7.2 Future Work*

My investigation of the superconductor overlayer traps for resonators showed improved performance at low temperatures. As the qubits also suffer due to non-

equilibrium quasiparticles, exploring the superconducting traps with a superconducting qubit would be the next logical step.

The understanding of resonator performance on overlayer setback can be improved by fabricating and measuring more devices. This would help to eliminate chip-to-chip variation in fabrication and packaging. The lower setbacks are more susceptible to fabrication defects than the larger ones due to the limitations of the fabrication resolution. Apart from the large setbacks, $s_b = 2\mu m$ also had an outstanding performance. The setbacks lower than 10 μm are within the quasiparticle diffusion length of TiN, which gives a chance of ballistic movement of QP away from the ground plane edge to the overlayers. Hence it would be interesting to examine these devices.

The superconducting gap difference $\Delta_{trap} = \Delta_S - \Delta_o$ between the primary superconductor $\Delta_s$ and overlayer $\Delta_o$ may affect the relaxation mechanism in the device. Different overlayer – superconductor combinations can be explored to optimize trapping. The proximity effect can significantly modify the overlayer bandgap, which in turn may affect $\Delta_{trap}$. The proximity effect can be controlled by changing the film thickness larger than coherence length or adding a thin tunneling barrier between the films. Introducing a tunneling barrier also gives a control variable to optimize the tunneling rate and affect quasiparticle poisoning at higher temperatures.

My power-temperature model of loss could not track the presence of thermal quasiparticles from overlayer quasiparticles present at high temperatures. The model can be improved for the trap devices to include the losses from the overlayer thermal quasiparticles. Instead of using a single $T_c$ for a resonator, a $T_c$ for the region with overlayer and another $T_c$ for the plain region can be used. The loss would be determined

by the percentage of coverage of the overlayer on the ground plane and the distribution of currents in the different regions. The application of standard conformal mapping techniques to CPW geometry may help.

Even the FDM trap design model can be improved to include different kinds of quasiparticle sources. Currently, the primary source is the QP near the ground plane edge. Including more uniform QP sources and investigating its effect on overall $Q_I$ can be investigated.

# Appendix A. Jacobian for the model for QP trap simulation

As described in section 4.5, discretized equations (4.26), (4.27), and (4.28) are solved using the iterative multivariate Newton Raphson method. To guess the starting point for the next iteration, Eq. (4.29) needs to be solved, which involves a Jacobian matrix

$$\mathcal{J}_f(\boldsymbol{z}) = \begin{bmatrix} \mathbf{J_{11}} & \mathbf{J_{12}} & \mathbf{J_{13}} \\ \mathbf{J_{21}} & \mathbf{J_{22}} & \mathbf{J_{23}} \\ \mathbf{J_{31}} & \mathbf{J_{32}} & \mathbf{J_{33}} \end{bmatrix} \tag{A.1}$$

The individual terms are

$$\begin{aligned} \mathrm{J}_{11} &= \left[\frac{\partial \mathrm{f}_{\mathrm{T_{o_i}}}}{\partial \mathrm{T_{o_i}}}\right]_{\mathrm{N'\times N'}} \quad \mathrm{J}_{12} = \left[\frac{\partial \mathrm{f}_{\mathrm{T_{o_i}}}}{\partial \mathrm{n_{ex_i}}}\right]_{\mathrm{N'\times N}} \quad \mathrm{J}_{13} = \left[\frac{\partial \mathrm{f}_{\mathrm{T_{o_i}}}}{\partial \mathrm{T_{p_i}}}\right]_{\mathrm{N'\times N}} \\ \mathrm{J}_{21} &= \left[\frac{\partial \mathrm{f}_{\mathrm{n_{ex_i}}}}{\partial \mathrm{T_{o_i}}}\right]_{\mathrm{N\times N'}} \quad \mathrm{J}_{22} = \left[\frac{\partial \mathrm{f}_{\mathrm{n_{ex_i}}}}{\partial \mathrm{n_{ex_i}}}\right]_{\mathrm{N\times N}} \quad \mathrm{J}_{23} = \left[\frac{\partial \mathrm{f}_{\mathrm{n_{ex_i}}}}{\partial \mathrm{T_{p_i}}}\right]_{\mathrm{N\times N}} \\ \mathrm{J}_{31} &= \left[\frac{\partial \mathrm{f}_{\mathrm{T_{p_i}}}}{\partial \mathrm{T_{o_i}}}\right]_{\mathrm{N\times N'}} \quad \mathrm{J}_{32} = \left[\frac{\partial \mathrm{f}_{\mathrm{T_{p_i}}}}{\partial \mathrm{n_{ex_i}}}\right]_{\mathrm{N\times N}} \quad \mathrm{J}_{13} = \left[\frac{\partial \mathrm{f}_{\mathrm{T_{p_i}}}}{\partial \mathrm{T_{p_i}}}\right]_{\mathrm{N\times N}} \end{aligned} \tag{A.2}$$

## A.1 Partial derivatives of the function $f_{T_{o_i}}$

$$\frac{\partial f_{T_{o_i}}}{\partial T_{o_i}} = -\Theta(x_i - x_{trap})(x_i) \times 2$$

$$\Theta(x_i - x_{trap})\ \left(\frac{\Delta x^2}{\kappa_o t_o}\right)\left(\Pi_e + \frac{\Pi_p}{4} + \frac{3\Pi_p}{4} A_{\frac{3\Delta}{4}-O}\right)\frac{\Delta}{q_e^2 \mathcal{R}_{trap} N(0)} \times \left(-\frac{\partial n}{\partial T}|_{T=T_{O_i}}\right) \tag{A.3}$$

$$-\Theta(x_i - x_{trap})\left(\frac{\Delta x^2}{\kappa_o t_o}\right)\ t_o \Sigma \times (-5T_{o_i}^4)$$

Where

$$\frac{\partial \mathrm{n}}{\partial \mathrm{T}} = 2\mathrm{N}(0)\sqrt{2\pi \mathrm{k_b T}\Delta}\exp\left(-\frac{\Delta}{\mathrm{k_B T}}\right)\left(\frac{\Delta(\mathrm{T})}{\mathrm{k_B T^2}} + \frac{1}{2\mathrm{T}}\right) \quad (A.4)$$

$$\frac{\partial f_{T_{o_i}}}{\partial n_{ex_i}} = \Theta\left(x_i - x_{trap}\right)\left(\frac{\Delta x^2}{\kappa_o t_o}\right)\left(\Pi_e + \frac{\Pi_p}{4} + \frac{3\Pi_p}{4}A_{\frac{3\Delta}{4}-O}\right)\frac{\Delta}{q_e^2 \mathcal{R}_{trap} N(0)} \quad (A.5)$$

$$+ \Theta\left(x_i - x_{trap}\right)\left(\frac{\Delta x^2}{\kappa_o t_o}\right) A_{2\Delta-O} t_s \Gamma_R\left(2n_{ex_i} + 2n_{th}\right)\Delta$$

$$\frac{\partial f_{T_{o_i}}}{\partial T_{p_i}} = -\Theta\left(x_i - x_{trap}\right)\left(\frac{\Delta x^2}{\kappa_o t_o}\right) t_o \Sigma \times (5T_{o_i}^4) \quad (A.6)$$

$$\frac{\partial f_{T_{o_i}}}{\partial T_{o_{i+1}}} = \frac{\partial f_{T_{o_i}}}{\partial T_{o_{i-1}}} = \Theta\left(x_i - x_{trap}\right) \quad (A.7)$$

## A.2 Partial derivatives of the function $f_{n_{ex_i}}$

$$\frac{\partial f_{n_{ex_i}}}{\partial n_{ex}} = -2 - \left(\frac{\Delta x^2}{t_s D_{QP}}\right)\Theta\left(x_i - x_{trap}\right)\frac{(1-\Pi_{tun})}{\Delta}\frac{\Delta}{q_e^2 \mathcal{R}_{trap} N(0)} \quad (A.8)$$

$$-\left(\frac{\Delta x^2}{t_s D_{QP}}\right)(1 - A_{2\Delta-s}) t_s \Gamma_R\left(2n_{ex_i} + 2n_{th}\right)$$

$$\frac{\partial f_{n_{ex_i}}}{\partial T_{o_i}} = -\frac{\Delta}{q_e^2 \mathcal{R}_{trap} N(0)} \times \left(-\frac{\partial n}{\partial T}\Big|_{T=T_{O_i}}\right) \quad (A.9)$$

$$\frac{\partial f_{n_{ex_i}}}{\partial T_{p_i}} = 0 \quad (A.10)$$

$$\frac{\partial f_{n_{ex_i}}}{\partial n_{ex_{i-1}}} = \frac{\partial f_{n_{ex_i}}}{\partial n_{ex_{i+1}}} = 1 \qquad (A.11)$$

## A.3 Partial derivatives of the function $f_{T_{p_i}}$

$$\frac{\partial f_{T_{p_i}}}{\partial T_{p_i}} = -2 + \left(\frac{\Delta x^2}{(t_s+t_o)\kappa_p}\right)\Theta(x_i - x_{trap}) \;\; t_o\Sigma \times \left(5T_{p_i}^4\right) - \left(\frac{\Delta x^2}{(t_s+t_o)\kappa_p}\right)\xi \times 4T_{P_i}^3 \qquad (A.12)$$

$$\frac{\partial f_{T_{p_i}}}{\partial T_{o_i}} = \left(\frac{\Delta x^2}{(t_s+t_o)\kappa_p}\right) g_{trap}(x_i)\; t_o\Sigma \times \left(-5T_{o_i}^4\right) \qquad (A.13)$$

$$\frac{\partial f_{T_{p_i}}}{\partial n_{ex_i}} = 0 \qquad (A.14)$$

$$\frac{\partial f_{T_{p_i}}}{\partial T_{p_{i-1}}} = \frac{\partial f_{T_{p_i}}}{\partial T_{p_{i+1}}} = 1 \qquad (A.15)$$

# Appendix B. Detailed Fabrication Steps

Here I describe the detailed fabrication recipe, I used for fabricating resonators with traps.

*Table B-1: Resonator Fabrication process list*

| **BILL OF MATERIALS** | | | | |
|---|---|---|---|---|
| 1 | 16 mm Chip | | | |
| **Chemical List** | | | | |
| 1 | AZ nLOF 2020 (photoresist) | | | |
| 2 | AZ 300 MIF Developer | | | |
| 3 | Acetone | | | |
| 4 | Methanol | | | |
| 5 | Isopropanol | | | |
| 6 | DI water (goosenecks) | | | |
| 7 | Aluminum Etchant | | | |
| 8 | Microposit 1165 | | | |
| | | | | |
| **PROCESSING RECIPE STARTS HERE** | | | | |
| | **Process** | **Recipe** | **Time** | **Notes** |
| **Processing steps Day 1** | | | | |
| **INTENSE WAFER CLEAN** | | | | |
| 1 | Acetone UltraSonication | in 600 ml Beaker, Ultra Sonicate the wafers | 3 min | Beaker # 1 |
| 2 | Methanol UltraSonication | in 600 ml Beaker, Ultra Sonicate the wafers | 3 min | Beaker # 2 |
| 3 | IPA UltraSonication | in 600 ml Beaker, Ultra Sonicate the wafers | 3 min | Beaker # 3 |
| 4 | DI UltraSonication | in 600 ml Beaker, Ultra Sonicate the wafers | 3 min | Beaker # 4 |
| 5 | IPA UltraSonication | in 600 ml Beaker, Ultra Sonicate the wafers | 3 min | Beaker # 3 |
| 6 | Take Micrograph | Optical microscope | | |
| 7 | Dehydration bake | 120 $^{o}$C on hot plate | 1 min | |
| **Lithography: Overlayer pattern** | | | | |
| 8 | spin AZ nLOF 2020 | 3000 RPM with 3000 rpm/s ramp, covered | 60s | use VERY CLEAN bottle, never re-use dropper, dispense 3-4 drops onto surface. **Check** |

| | | | | |
|---|---|---|---|---|
| | | | | **/Clean back side before baking!** |
| 9 | prebake | 110°C | 60s | Hotplate with substrate vacuum on |
| 10 | cool | cool on table | 60s | Allow chip to cool about 30s |
| 11 | place wafer on stepper chuck | manual placement | | note that you should use a chuck that is +/- 50 µm within the thickness of your wafer. |
| 12 | stepper setup | stepper prompt:: "CHUCK", "C", "10" | | Command to change chuck size to 10mm die, |
| 13 | expose | stepper prompt:: "EXEC <FILENAME>" | 1 s | |
| 14 | post-bake | 110°C | 60s | Hotplate with substrate vacuum on |
| 15 | cool | cool on table | 60s | Allow chip to cool about 30s |
| 16 | develop in AZ 300 MIF Developer | beaker develop | 120s | manual agitation about 0.5 Hz |
| 17 | $H_2O$ rinse | beaker rinse | 60s | manual agitation at approximately 0.5 Hz, rinse from gooseneck after beaker, N2 blow dry |
| 18 | N2 Dry | Air gun | 60 s | |
| 19 | inspect | Optical microscope | | Take micrographs. Check resolution and guide patterns for significant defects |
| **CONVENIENT PROCESSING BREAK** | | | | |
| **Layer 1 - Al wet etch** | | | | |
| 20 | Dip in the Al etchant | Beaker | ~ 110 s for 100 nm | |
| 21 | Dip in DI water | | 60 s | |
| **STRIP Photoresist** | | | | |

| | | | | |
|---|---|---|---|---|
| 22 | Solvent Bath #1: MICROPOSIT remover 1165 | 80°C bath removed from hotplate, directly into ultrasonic 700ml Beaker | 5 min | Beaker 1: first agitation to remove bulk of photoresist and residuals. |
| | | | | |
| 23 | Solvent Bath #2: MICROPOSIT remover 1165 | beaker on hotplate 80°C | 30 min | High-temp soak in beaker 2 |
| 24 | Solvent Bath #3: MICROPOSIT remover 1165 | beaker on hotplate 80°C | 30 min | High-temp soak in beaker 3 |
| 25 | Solvent Bath #4: MICROPOSIT remover 1165 | 80°C bath removed from hotplate, directly into ultrasonic | 5 min | Beaker 4: fresh batch for any additional residue removal - |
| 26 | DI Ultrsonication | 600 ml Beaker | 3 min | Cleaning the Microposit 1165 |
| 27 | DI rinse | gooseneck | 60 s | |
| 28 | IPA pre-clean | Beaker | 60 s | |
| 29 | Dry wafer | N2 gun | | |
| 30 | inspect | optical microscope | | Inspect for residues remaining, check edges, use nomarski |
| **CONVENIENT PROCESSING BREAK** | | | | |
| **Titanium Nitride Etch** | | | | |
| 31 | Acetone Clean | Spray Bottle | 15 s | |
| 32 | Methanol Clean | Spray Bottle | 15 s | |
| 33 | IPA | Spray Bottle | 15 s | |
| 34 | Dehydration bake | 120°C on hot plate | 1 min | |
| **Lithography: Overlayer pattern** | | | | |
| 35 | spin AZ nLOF 2020 | 3000 RPM with 3000 rpm/s ramp, covered | 60s | use VERY CLEAN bottle, never re-use dropper, dispense 3-4 drops onto surface. **Check /Clean back side before baking!** |
| 36 | prebake | 110°C | 60s | Hotplate with substrate vacuum on |
| 37 | cool | cool on table | 60s | Allow chip to cool about 30s |
| 38 | place wafer on stepper chuck | manual placement | | note that you should use a chuck that is +/- 50 µm within the thickness of your wafer. |

| | | | | |
|---|---|---|---|---|
| 39 | expose | stepper prompt:: "MAP <FILENAME>", 2" | 1 s | Stepper file which enables microDFAS to align with existing alignment marks. |
| 40 | post-bake | 110°C | 60s | Hotplate with substrate vacuum on |
| 41 | cool | cool on table | 60s | Allow chip to cool about 30s |
| 42 | develop in AZ 300 MIF Developer | beaker develop | 120s | manual agitation about 0.5 Hz |
| 43 | $H_2O$ rinse | beaker rinse | 60s | manual agitation at approximately 0.5 Hz, rinse from gooseneck after beaker, N2 blow dry |
| 44 | N2 Dry | Air gun | 60 s | |
| 45 | inspect | Optical microscope | | Take micrographs. Check resolution for 0.7 μm lines (approximatley) and guide patterns for significant defects |
| **ICP Dry Etch** | | | | |
| 46 | Clean the chip holding Sapphire wafer | Using TCE bath | | |
| 47 | Apply the grease using a paper template | | | Make sure that there is no extra grease outside the chip. |
| 48 | Load to chamber | ::SERVICE->MAINTENANCE->WAFER HANDLING->LOAD | | Load wafer into chamber manually using this sequence |
| 49 | ICP etch | ::SERVICE-> MANUAL MODE (see notes) | T=300s | Use manual mode: Params $BCl_3$ - 12.5sccm $Cl_2$ - 2.5sccm P - 3.5mtorr, Bias - 50W, ICP - 500W, Temp - 35C. |
| **Post etch corrosion mitigation** | | | | |
| 50 | Wait post etch | | 30 min | |
| 51 | Unload | ::SERVICE->MAINTENANCE->WAFER | | |

| | | | | |
|---|---|---|---|---|
| | | HANDLING->UNLOAD | | |
| 52 | DI dip | 2000 ml DI Beaker, ~80C | 60s | 2000 ml of DI in 2000 ml beaker set to 80C. immidiatley dunk chip in water, mild agitation, |
| 53 | Remove chip from carrier | razor blade | <60s (Track and record time of steps 27+28) | Carefully remove chip from carrier |
| 54 | Clean off chip backside | | | wipe backside with TCE on a cleanroom wipe, do not contact Al film side |
| **Strip Photoresist** | | | | |
| 55 | Solvent Bath #1: MICROPOSIT remover 1165 | 80°C bath removed from hotplate, directly into ultrasonic 700ml Beaker | 5 min | Beaker 1: first agitation to remove bulk of photoresist and residuals. |
| 56 | Solvent Bath #2: MICROPOSIT remover 1165 | beaker on hotplate 80°C | 30 min | High-temp soak in beaker 2 |
| 57 | Solvent Bath #3: MICROPOSIT remover 1165 | beaker on hotplate 80°C | 30 min | High-temp soak in beaker 3 |
| 58 | Solvent Bath #4: MICROPOSIT remover 1165 | 80°C bath removed from hotplate, directly into ultrasonic | 5 min | Beaker 4: fresh batch for any additional residue removal - beaker in ultrasonic bath for 20 min. |
| **CONVENIENT PROCESSING BREAK** | | | | |
| 59 | DI Ultrsonication | 600 ml Beaker | 3 min | Cleaning the Microposit 1165 |
| 60 | DI rinse | gooseneck | 60 s | |
| 61 | IPA pre-clean | Beaker | 60 s | |
| 62 | Dry wafer | N2 gun | | |
| 63 | inspect | optical microscope | | Inspect for residues remaining, check edges, use nomarski |

# Appendix C. Supplementary plots from power temperature simulation

In section 6.3, to investigate the trapping efficiency for different setbacks, the quasiparticle quality factor $Q_{QP}$ was extracted from the total internal quality factor after subtracting the TLS and non-TLS-non QP loss. The extracted $Q_{QP}$ from $Q_I$ is plotted here.

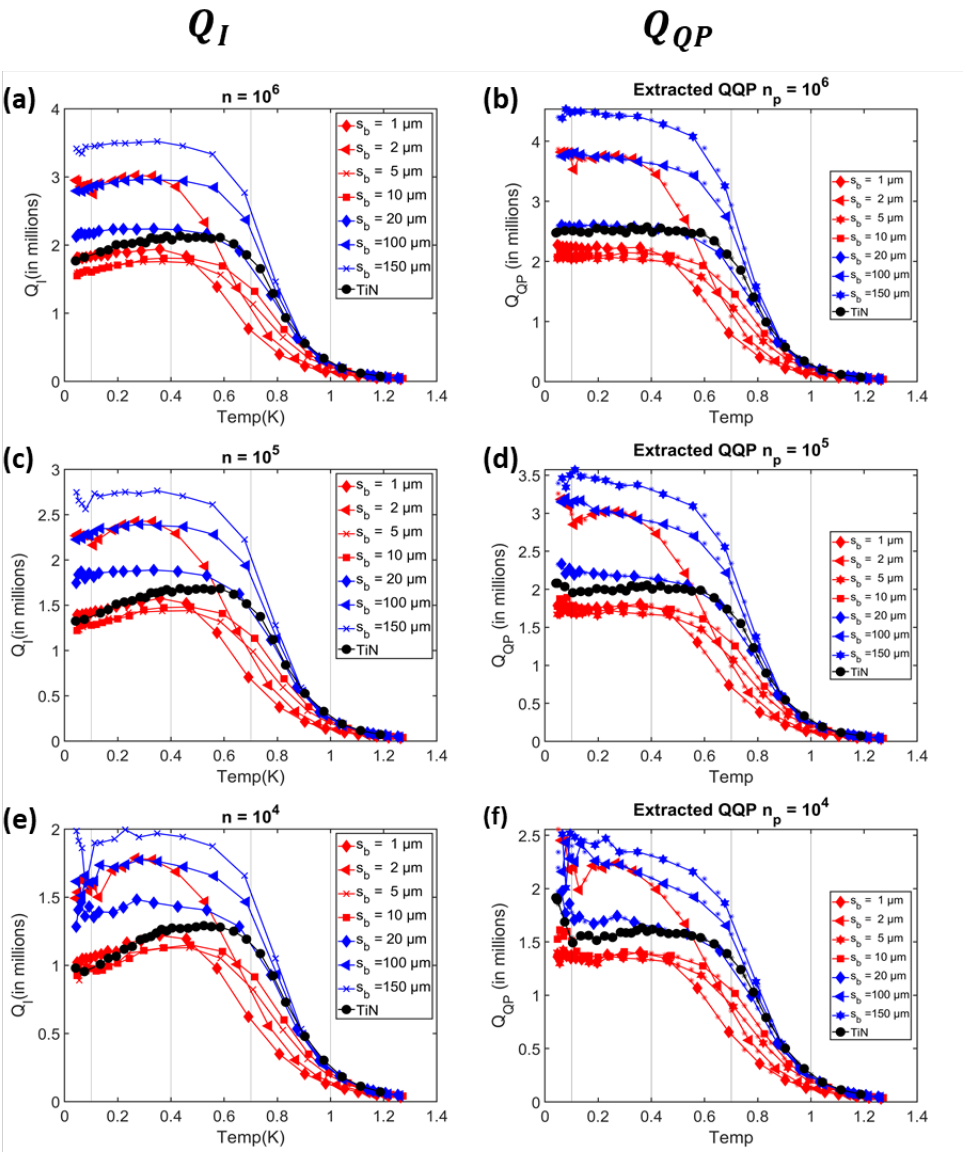

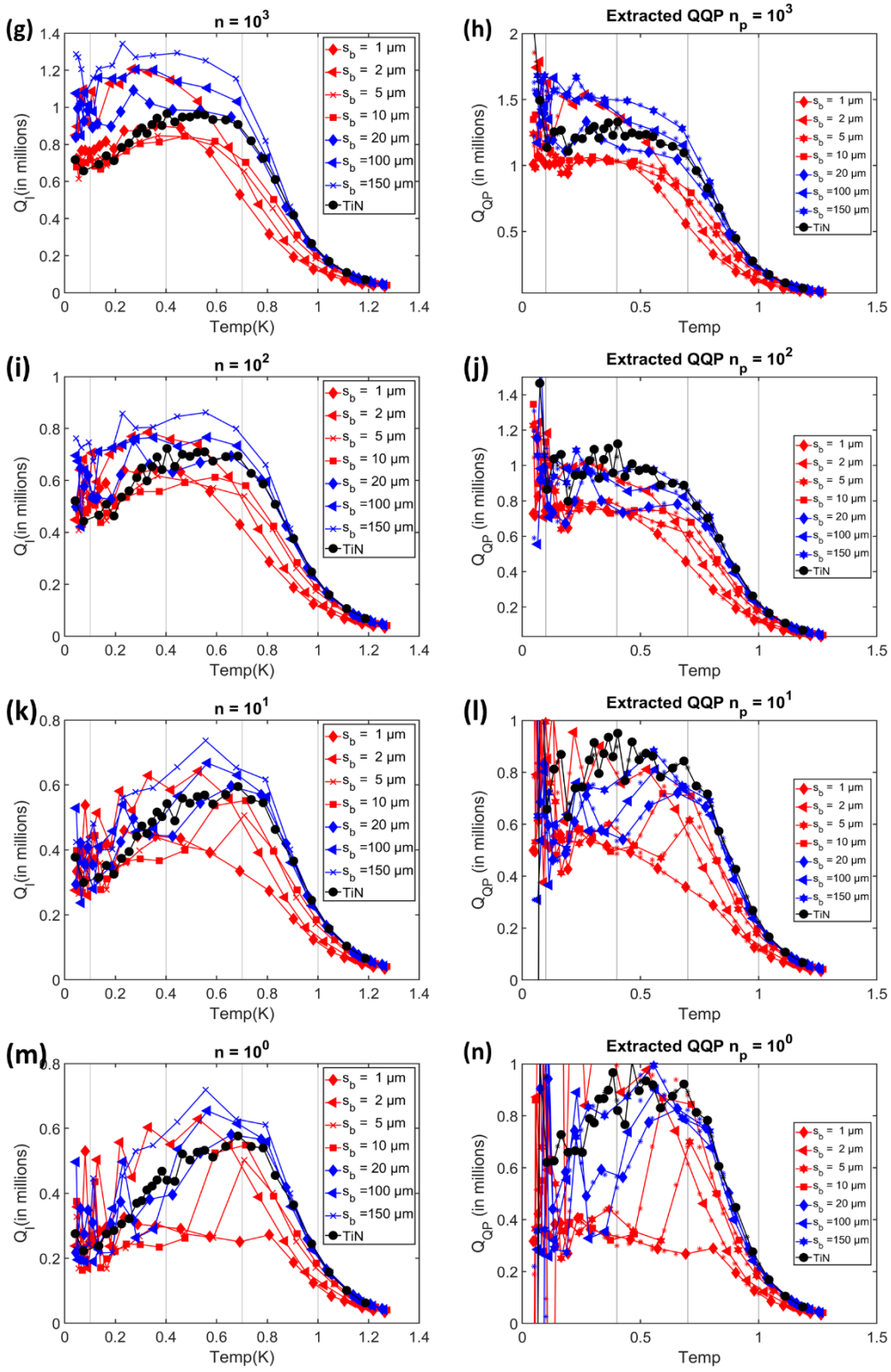


*Fig. C.1:Comparison of $Q_I$ and extracted quasiparticle $Q_{QP}$ at different powers*

# Bibliography


[1] C. P. Williams, *Explorations in Quantum Computing*, vol. 42. London: Springer London, 2011.

[2] N. D. Mermin, *Quantum Computer Science*. Cambridge: Cambridge University Press, 2007.

[3] P. Krantz, M. Kjaergaard, F. Yan, T. P. Orlando, S. Gustavsson, and W. D. Oliver, "A quantum engineer's guide to superconducting qubits," *Appl. Phys. Rev.*, vol. 6, no. 2, p. 021318, Jun. 2019.

[4] A. A. Houck, J. Koch, M. H. Devoret, S. M. Girvin, and R. J. Schoelkopf, "Life after charge noise: recent results with transmon qubits," *Quantum Inf. Process.*, vol. 8, no. 2–3, pp. 105–115, Jun. 2009.

[5] D. P. DiVincenzo, "The Physical Implementation of Quantum Computation," *Fortschritte der Phys.*, vol. 48, no. 9–11, pp. 771–783, Sep. 2000.

[6] J. N. Eckstein and J. Levy, "Materials issues for quantum computation," *MRS Bull.*, vol. 38, no. 10, pp. 783–789, Oct. 2013.

[7] R. Ozeri, "The trapped-ion qubit tool box," *Contemp. Phys.*, vol. 52, no. 6, pp. 531–550, Nov. 2011.

[8] D. Kim *et al.*, "Microwave-driven coherent operation of a semiconductor quantum dot charge qubit," *Nat. Nanotechnol.*, vol. 10, no. 3, pp. 243–247, Mar. 2015.

[9] L. Gordon, J. R. Weber, J. B. Varley, A. Janotti, D. D. Awschalom, and C. G. Van de Walle, "Quantum computing with defects," *MRS Bull.*, vol. 38, no. 10, pp. 802–807, Oct. 2013.

[10] J. Koch *et al.*, "Charge-insensitive qubit design derived from the Cooper pair box," *Phys. Rev. A*, vol. 76, no. 4, p. 042319, Oct. 2007.

[11] W. D. Oliver and P. B. Welander, "Materials in superconducting quantum bits," *MRS Bull.*, vol. 38, no. 10, pp. 816–825, Oct. 2013.

[12] M. H. devoret and J. M. Martinis, "Implementing Qubits with Superconducting Integrated Circuits," *Quantum Inf. Process.*, vol. 3, no. 1–5, pp. 163–203, Oct. 2004.

[13] A. F. Kockum and F. Nori, "Quantum Bits with Josephson Junctions," in *Springer Series in Materials Science*, vol. 286, Springer Verlag, 2019, pp. 703–741.

[14] A. Blais, R.-S. Huang, A. Wallraff, S. M. Girvin, and R. J. Schoelkopf, "Cavity quantum electrodynamics for superconducting electrical circuits: An architecture for quantum computation," *Phys. Rev. A*, vol. 69, no. 6, p. 062320, Jun. 2004.

[15] A. Blais, A. L. Grimsmo, S. M. Girvin, and A. Wallraff, "Circuit quantum

electrodynamics," *Rev. Mod. Phys.*, vol. 93, no. 2, p. 025005, May 2021.

[16] A. Megrant *et al.*, "Planar superconducting resonators with internal quality factors above one million," *Appl. Phys. Lett.*, vol. 100, no. 11, p. 113510, Mar. 2012.

[17] M. Sandberg *et al.*, "Etch induced microwave losses in titanium nitride superconducting resonators," *Appl. Phys. Lett.*, vol. 100, no. 26, p. 262605, Jun. 2012.

[18] A. Bruno, G. de Lange, S. Asaad, K. L. van der Enden, N. K. Langford, and L. DiCarlo, "Reducing intrinsic loss in superconducting resonators by surface treatment and deep etching of silicon substrates," *Appl. Phys. Lett.*, vol. 106, no. 18, p. 182601, May 2015.

[19] C. M. Quintana *et al.*, "Characterization and reduction of microfabrication-induced decoherence in superconducting quantum circuits," *Appl. Phys. Lett.*, vol. 105, no. 6, p. 062601, Aug. 2014.

[20] G. Calusine *et al.*, "Analysis and mitigation of interface losses in trenched superconducting coplanar waveguide resonators," *Appl. Phys. Lett.*, vol. 112, no. 6, p. 062601, Feb. 2018.

[21] K. M. Lang, S. Nam, J. Aumentado, C. Urbina, and J. M. Martinis, "Banishing quasiparticles from Josephson-junction qubits: Why and how to do it," *IEEE Trans. Appiled Supercond.*, vol. 13, no. 2, pp. 989–993, Jun. 2003.

[22] J. M. Martinis, M. Ansmann, and J. Aumentado, "Energy Decay in Superconducting Josephson-Junction Qubits from Nonequilibrium Quasiparticle Excitations," *Phys. Rev. Lett.*, vol. 103, no. 9, p. 097002, Aug. 2009.

[23] K. Serniak *et al.*, "Hot Nonequilibrium Quasiparticles in Transmon Qubits," *Phys. Rev. Lett.*, vol. 121, no. 15, p. 157701, Oct. 2018.

[24] J. P. Pekola *et al.*, "Single-electron current sources: Toward a refined definition of the ampere," *Rev. Mod. Phys.*, vol. 85, no. 4, pp. 1421–1472, Oct. 2013.

[25] C. Wang *et al.*, "Measurement and control of quasiparticle dynamics in a superconducting qubit," *Nat. Commun.*, vol. 5, no. 1, p. 5836, Dec. 2014.

[26] H. S. Knowles, V. F. Maisi, and J. P. Pekola, "Probing quasiparticle excitations in a hybrid single electron transistor," *Appl. Phys. Lett.*, vol. 100, no. 26, p. 262601, Jun. 2012.

[27] J. P. Pekola *et al.*, "Single-electron current sources: Toward a refined definition of the ampere," *Rev. Mod. Phys.*, vol. 85, no. 4, pp. 1421–1472, 2013.

[28] H. Q. Nguyen *et al.*, "Trapping hot quasi-particles in a high-power superconducting electronic cooler," *New J. Phys.*, vol. 15, no. 8, p. 085013, Aug. 2013.

[29] J. N. Ullom and P. A. Fisher, “Quasiparticle behavior in tunnel junction refrigerators,” *Phys. B Condens. Matter*, vol. 284–288, no. PART II, pp. 2036–2038, 2000.

[30] S. Rajauria, L. M. A. Pascal, P. Gandit, F. W. J. Hekking, B. Pannetier, and H. Courtois, “Efficiency of quasiparticle evacuation in superconducting devices,” *Phys. Rev. B*, vol. 85, no. 2, p. 020505, Jan. 2012.

[31] R. Barends, J. J. A. Baselmans, S. J. C. Yates, J. R. Gao, J. N. Hovenier, and T. M. Klapwijk, “Quasiparticle Relaxation in Optically Excited High-Q Superconducting Resonators,” *Phys. Rev. Lett.*, vol. 100, no. 25, p. 257002, Jun. 2008.

[32] U. Patel, I. V. Pechenezhskiy, B. L. T. Plourde, M. G. Vavilov, and R. McDermott, “Phonon-mediated quasiparticle poisoning of superconducting microwave resonators,” *Phys. Rev. B*, vol. 96, no. 22, p. 220501, Dec. 2017.

[33] P. K. Day, H. G. LeDuc, B. A. Mazin, A. Vayonakis, and J. Zmuidzinas, “A broadband superconducting detector suitable for use in large arrays,” *Nature*, vol. 425, no. 6960, pp. 817–821, Oct. 2003.

[34] L. Grünhaupt *et al.*, “Loss Mechanisms and Quasiparticle Dynamics in Superconducting Microwave Resonators Made of Thin-Film Granular Aluminum,” *Phys. Rev. Lett.*, vol. 121, no. 11, p. 117001, Sep. 2018.

[35] R. Barends *et al.*, “Minimizing quasiparticle generation from stray infrared light in superconducting quantum circuits,” *Appl. Phys. Lett.*, vol. 99, no. 11, p. 113507, Sep. 2011.

[36] J.-H. Yeh, J. LeFebvre, S. Premaratne, F. C. Wellstood, and B. S. Palmer, “Microwave attenuators for use with quantum devices below 100 mK,” *J. Appl. Phys.*, vol. 121, no. 22, p. 224501, Jun. 2017.

[37] H. Paik *et al.*, “Observation of High Coherence in Josephson Junction Qubits Measured in a Three-Dimensional Circuit QED Architecture,” *Phys. Rev. Lett.*, vol. 107, no. 24, p. 240501, Dec. 2011.

[38] I. Nsanzineza and B. L. T. Plourde, “Trapping a Single Vortex and Reducing Quasiparticles in a Superconducting Resonator,” *Phys. Rev. Lett.*, vol. 113, no. 11, p. 117002, Sep. 2014.

[39] R.-P. Riwar *et al.*, “Normal-metal quasiparticle traps for superconducting qubits,” *Phys. Rev. B*, vol. 94, no. 10, p. 104516, Sep. 2016.

[40] R.-P. Riwar, L. I. Glazman, and G. Catelani, “Dissipation by normal-metal traps in transmon qubits,” *Phys. Rev. B*, vol. 98, no. 2, p. 024502, Jul. 2018.

[41] J. N. Ullom, P. A. Fisher, and M. Nahum, “Measurements of quasiparticle thermalization in a normal metal,” *Phys. Rev. B*, vol. 61, no. 21, pp. 14839–14843, Jun. 2000.

[42] R.-P. Riwar and G. Catelani, “Efficient quasiparticle traps with low dissipation through gap engineering,” *Phys. Rev. B*, vol. 100, no. 14, p. 144514, Oct. 2019.

[43] J. Bardeen, L. N. Cooper, and J. R. Schrieffer, “Theory of Superconductivity,” *Phys. Rev.*, vol. 108, no. 5, pp. 1175–1204, Dec. 1957.

[44] T. Van Duzer and C. W. Turner, *Principles of Superconductive Devices and Circuits*, 2nd ed. Elsevier, 1981.

[45] A. C. Rose-Innes, E. H. Rhoderick, and A. M. Goldman, “Introduction to Superconductivity,” *Am. J. Phys.*, vol. 38, no. 8, pp. 1048–1049, Aug. 1970.

[46] J. Gao, “The Physics of Superconducting Microwave Resonators,” California Institute of Technology, 2008.

[47] M. Lenander *et al.*, “Measurement of energy decay in superconducting qubits from nonequilibrium quasiparticles,” *Phys. Rev. B*, vol. 84, no. 2, p. 024501, Jul. 2011.

[48] S. B. Kaplan, C. C. Chi, D. N. Langenberg, J. J. Chang, S. Jafarey, and D. J. Scalapino, “Quasiparticle and phonon lifetimes in superconductors,” *Phys. Rev. B*, vol. 14, no. 11, pp. 4854–4873, Dec. 1976.

[49] P. J. de Visser, D. J. Goldie, P. Diener, S. Withington, J. J. A. Baselmans, and T. M. Klapwijk, “Evidence of a Nonequilibrium Distribution of Quasiparticles in the Microwave Response of a Superconducting Aluminum Resonator,” *Phys. Rev. Lett.*, vol. 112, no. 4, p. 047004, Jan. 2014.

[50] F. Jaworski, W. H. Parker, and S. B. Kaplan, “Quasiparticle and phonon lifetimes in superconducting Pb films,” *Phys. Rev. B*, vol. 14, no. 9, pp. 4209–4212, Nov. 1976.

[51] S. B. Kaplan, “Acoustic matching of superconducting films to substrates,” *J. Low Temp. Phys.*, vol. 37, no. 3–4, pp. 343–365, Nov. 1979.

[52] F. London and H. London, “The electromagnetic equations of the supraconductor,” *Proc. R. Soc. London. Ser. A - Math. Phys. Sci.*, vol. 149, no. 866, pp. 71–88, Mar. 1935.

[53] R. Barends, “Photon-detecting superconducting resonators,” Delft University of Technology, 2009.

[54] D. C. Mattis and J. Bardeen, “Theory of the Anomalous Skin Effect in Normal and Superconducting Metals,” *Phys. Rev.*, vol. 111, no. 2, pp. 412–417, Jul. 1958.

[55] J. Gao, J. Zmuidzinas, A. Vayonakis, P. Day, B. Mazin, and H. Leduc, “Equivalence of the Effects on the Complex Conductivity of Superconductor due to Temperature Change and External Pair Breaking,” *J. Low Temp. Phys.*, vol. 151, no. 1–2, pp. 557–563, Apr. 2008.

[56] R. N. Simons, *Coplanar Waveguide Circuits, Components, and Systems*. John Wiley & Sons, Inc., 2004.

[57] I. Wolff, *Coplanar Microwave Integrated Circuits*, 1st ed. New Jersey: John Wiley & Sons, Inc., 2006.

[58] M. Gillick, I. D. Robertson, and J. S. Joshi, “Direct analytical solution for the

electric field distribution at the conductor surfaces of coplanar waveguides," *IEEE Trans. Microw. Theory Tech.*, vol. 41, no. 1, pp. 129–135, 1993.

[59] D. M. Pozar, *Microwave Engineering*, Fourth Edi. John Wiley &Sons, Inc, 2011.

[60] R. E. Collin, *Foundations for Microwave Engineering*. New York: John Wiley & Sons, Inc., 2001.

[61] J. M. Sage, V. Bolkhovsky, W. D. Oliver, B. Turek, and P. B. Welander, "Study of loss in superconducting coplanar waveguide resonators," *J. Appl. Phys.*, vol. 109, no. 6, p. 063915, Mar. 2011.

[62] C. Müller, J. H. Cole, and J. Lisenfeld, "Towards understanding two-level-systems in amorphous solids: insights from quantum circuits," *Rep. Prog. Phys.*, vol. 82, no. 12, p. 124501, 2019.

[63] W. A. Phillips, "Two-level states," *Rep. Prog. Phys.*, vol. 50, pp. 1657–1708, 1987.

[64] R. McDermott, "Materials Origins of Decoherence in Superconducting Qubits," *IEEE Trans. Appl. Supercond.*, vol. 19, no. 1, pp. 2–13, Feb. 2009.

[65] W. A. Phillips, "Tunneling states in amorphous solids," *J. Low Temp. Phys.*, vol. 7, no. 3–4, pp. 351–360, May 1972.

[66] A. L. Burin, M. S. Khalil, and K. D. Osborn, "Universal Dielectric Loss in Glass from Simultaneous Bias and Microwave Fields," *Phys. Rev. Lett.*, vol. 110, no. 15, p. 157002, Apr. 2013.

[67] C. R. H. McRae *et al.*, "Materials loss measurements using superconducting microwave resonators," *Rev. Sci. Instrum.*, vol. 91, no. 9, p. 091101, Sep. 2020.

[68] D. P. Pappas, M. R. Vissers, D. S. Wisbey, J. S. Kline, and J. Gao, "Two Level System Loss in Superconducting Microwave Resonators," *IEEE Trans. Appl. Supercond.*, vol. 21, no. 3, pp. 871–874, Jun. 2011.

[69] R. Barends *et al.*, "Minimal resonator loss for circuit quantum electrodynamics," *Appl. Phys. Lett.*, vol. 97, no. 2, p. 023508, Jul. 2010.

[70] C. J. K. Richardson *et al.*, "Fabrication artifacts and parallel loss channels in metamorphic epitaxial aluminum superconducting resonators," *Supercond. Sci. Technol.*, vol. 29, no. 6, p. 064003, Jun. 2016.

[71] J. Gao *et al.*, "Experimental evidence for a surface distribution of two-level systems in superconducting lithographed microwave resonators," *Appl. Phys. Lett.*, vol. 92, no. 15, p. 152505, Apr. 2008.

[72] J. Wenner *et al.*, "Surface loss simulations of superconducting coplanar waveguide resonators," *Appl. Phys. Lett.*, vol. 99, no. 11, p. 113513, Sep. 2011.

[73] H. Wang *et al.*, "Improving the coherence time of superconducting coplanar resonators," *Appl. Phys. Lett.*, vol. 95, no. 23, p. 233508, Dec. 2009.

[74] R. Barends *et al.*, “Niobium and Tantalum High Q Resonators for Photon Detectors,” *IEEE Trans. Appl. Supercond.*, vol. 17, no. 2, pp. 263–266, Jun. 2007.

[75] S. Kumar, J. Gao, J. Zmuidzinas, B. A. Mazin, H. G. LeDuc, and P. K. Day, “Temperature dependence of the frequency and noise of superconducting coplanar waveguide resonators,” *Appl. Phys. Lett.*, vol. 92, no. 12, p. 123503, Mar. 2008.

[76] J. Goetz *et al.*, “Loss mechanisms in superconducting thin film microwave resonators,” *J. Appl. Phys.*, vol. 119, no. 1, p. 015304, Jan. 2016.

[77] M. R. Vissers *et al.*, “Low loss superconducting titanium nitride coplanar waveguide resonators,” *Appl. Phys. Lett.*, vol. 97, no. 23, p. 232509, Dec. 2010.

[78] S. Ohya *et al.*, “Room temperature deposition of sputtered TiN films for superconducting coplanar waveguide resonators,” *Supercond. Sci. Technol.*, vol. 27, no. 1, p. 015009, Jan. 2014.

[79] J. B. Chang *et al.*, “Improved superconducting qubit coherence using titanium nitride,” *Appl. Phys. Lett.*, vol. 103, no. 1, p. 012602, Jul. 2013.

[80] A. Bruno, G. de Lange, S. Asaad, K. L. van der Enden, N. K. Langford, and L. DiCarlo, “Reducing intrinsic loss in superconducting resonators by surface treatment and deep etching of silicon substrates,” *Appl. Phys. Lett.*, vol. 106, no. 18, p. 182601, May 2015.

[81] D. S. Wisbey *et al.*, “Effect of metal/substrate interfaces on radio-frequency loss in superconducting coplanar waveguides,” *J. Appl. Phys.*, vol. 108, no. 9, p. 093918, Nov. 2010.

[82] A. Melville *et al.*, “Comparison of dielectric loss in titanium nitride and aluminum superconducting resonators,” *Appl. Phys. Lett.*, vol. 117, no. 12, p. 124004, Sep. 2020.

[83] M. V. P. Altoé *et al.*, “Localization and reduction of superconducting quantum coherent circuit losses,” pp. 1–20, Dec. 2020.

[84] M. R. Vissers, J. S. Kline, J. Gao, D. S. Wisbey, and D. P. Pappas, “Reduced microwave loss in trenched superconducting coplanar waveguides,” *Appl. Phys. Lett.*, vol. 100, no. 8, p. 082602, Feb. 2012.

[85] G. Calusine *et al.*, “Analysis and mitigation of interface losses in trenched superconducting coplanar waveguide resonators,” *Appl. Phys. Lett.*, vol. 112, no. 6, p. 062601, Feb. 2018.

[86] M. Morita, T. Ohmi, E. Hasegawa, M. Kawakami, and M. Ohwada, “Growth of native oxide on a silicon surface,” *J. Appl. Phys.*, vol. 68, no. 3, pp. 1272–1281, Aug. 1990.

[87] J. Evertsson *et al.*, “The thickness of native oxides on aluminum alloys and single crystals,” *Appl. Surf. Sci.*, vol. 349, pp. 826–832, Sep. 2015.

[88] A. P. Vepsäläinen *et al.*, “Impact of ionizing radiation on superconducting qubit coherence,” *Nature*, vol. 584, no. 7822, pp. 551–556, Aug. 2020.

[89] O. Rafferty *et al.*, “Spurious Antenna Modes of the Transmon Qubit,” pp. 1–9, Mar. 2021.

[90] P. J. de Visser, J. J. A. Baselmans, S. J. C. Yates, P. Diener, A. Endo, and T. M. Klapwijk, “Microwave-induced excess quasiparticles in superconducting resonators measured through correlated conductivity fluctuations,” *Appl. Phys. Lett.*, vol. 100, no. 16, p. 162601, Apr. 2012.

[91] D. J. Goldie and S. Withington, “Non-equilibrium superconductivity in quantum-sensing superconducting resonators,” *Supercond. Sci. Technol.*, vol. 26, no. 1, p. 015004, Jan. 2013.

[92] J.-J. Chang and D. J. Scalapino, “Kinetic-equation approach to nonequilibrium superconductivity,” *Phys. Rev. B*, vol. 15, no. 5, pp. 2651–2670, Mar. 1977.

[93] R. P. Budoyo *et al.*, “Effects of nonequilibrium quasiparticles in a thin-film superconducting microwave resonator under optical illumination,” *Phys. Rev. B*, vol. 93, no. 2, p. 024514, Jan. 2016.

[94] T. Guruswamy, D. J. Goldie, and S. Withington, “Nonequilibrium superconducting thin films with sub-gap and pair-breaking photon illumination,” *Supercond. Sci. Technol.*, vol. 28, no. 5, p. 054002, May 2015.

[95] T. Guruswamy, D. J. Goldie, and S. Withington, “Quasiparticle generation efficiency in superconducting thin films,” *Supercond. Sci. Technol.*, vol. 27, no. 5, p. 055012, May 2014.

[96] T. Guruswamy, “Nonequilibrium behaviour and quasiparticle heating in thin film superconducting microwave resonators,” University of Cambridge, 2018.

[97] A. Rothwarf and B. N. Taylor, “Measurement of Recombination Lifetimes in Superconductors,” *Phys. Rev. Lett.*, vol. 19, no. 1, pp. 27–30, Jul. 1967.

[98] J. Pearl, “CURRENT DISTRIBUTION IN SUPERCONDUCTING FILMS CARRYING QUANTIZED FLUXOIDS,” *Appl. Phys. Lett.*, vol. 5, no. 4, pp. 65–66, Aug. 1964.

[99] C. Song *et al.*, “Microwave response of vortices in superconducting thin films of Re and Al,” *Phys. Rev. B*, vol. 79, no. 17, p. 174512, May 2009.

[100] J. Zmuidzinas, “Superconducting Microresonators: Physics and Applications,” *Annu. Rev. Condens. Matter Phys.*, vol. 3, no. 1, pp. 169–214, Mar. 2012.

[101] J. Wenner *et al.*, “Wirebond crosstalk and cavity modes in large chip mounts for superconducting qubits,” *Supercond. Sci. Technol.*, vol. 24, no. 6, p. 065001, Jun. 2011.

[102] M. Abuwasib, P. Krantz, and P. Delsing, “Fabrication of large dimension aluminum air-bridges for superconducting quantum circuits,” *J. Vac. Sci. Technol. B, Nanotechnol. Microelectron. Mater. Process. Meas. Phenom.*, vol. 31, no. 3, p. 031601, May 2013.

[103] S. Huang *et al.*, "Microwave Package Design for Superconducting Quantum Processors," *PRX Quantum*, vol. 2, no. 2, p. 020306, Apr. 2021.

[104] R. Sturdivant, *Microwave & Millimeter-Wave Electronic Packaging*. Boston, London: Artech House, 2013.

[105] B. Lienhard *et al.*, "Microwave Packaging for Superconducting Qubits," in *2019 IEEE MTT-S International Microwave Symposium (IMS)*, 2019, vol. 2019-June, pp. 275–278.

[106] D. Goldie, N. Booth, C. Patel, and G. Salmon, "Quasiparticle trapping from a single-crystal superconductor into a normal-metal film via the proximity effect," *Phys. Rev. Lett.*, vol. 64, no. 8, pp. 954–957, Feb. 1990.

[107] G. C. O'Neil, P. J. Lowell, J. M. Underwood, and J. N. Ullom, "Measurement and modeling of a large-area normal-metal/insulator/superconductor refrigerator with improved cooling," *Phys. Rev. B*, vol. 85, no. 13, p. 134504, Apr. 2012.

[108] G. C. O'Neil, "Improving NIS Tunnel Junction Refrigerators : Modeling , Materials , and Traps by," University of Colorado, 2011.

[109] M. Tinkham, *Introduction to Superconductivity*, 2nd ed. Mineola, New York: Dover Publications, Inc., 2004.

[110] F. C. Wellstood, C. Urbina, and J. Clarke, "Hot-electron effects in metals," *Phys. Rev. B*, vol. 49, no. 9, pp. 5942–5955, Mar. 1994.

[111] J. N. Ullom, "Superconducting Quasiparticle Behavior: Trapping, Propagation, and Loss," Harvard University, 1998.

[112] W. A. Little, "The transport of heat between dissimilar solids at low temperatures," *Can. J. Phys.*, vol. 37, no. 3, pp. 334–349, Mar. 1959.

[113] E. T. Swartz and R. O. Pohl, "Thermal resistance at interfaces," *Appl. Phys. Lett.*, vol. 51, no. 26, pp. 2200–2202, Dec. 1987.

[114] N. Ashcroft and N. Mermin, *Solid State Physics*. Holt-Saunders, 1976.

[115] E. T. Swartz and R. O. Pohl, "Thermal boundary resistance," *Rev. Mod. Phys.*, vol. 61, no. 3, pp. 605–668, 1989.

[116] J. D. N. Cheeke, H. Ettinger, and B. Hebral, "Analysis of heat transfer between solids at low temperatures," *Can. J. Phys.*, vol. 54, no. 17, pp. 1749–1771, Sep. 1976.

[117] C. Ji, A. Beyer, S. Golwala, and J. Sayers, "Design of antenna-coupled lumped-element titanium nitride KIDs for long-wavelength multi-band continuum imaging," in *Millimeter, Submillimeter, and Far-Infrared Detectors and Instrumentation for Astronomy VII*, 2014, vol. 9153, p. 915321.

[118] H. G. Leduc *et al.*, "Titanium nitride films for ultrasensitive microresonator detectors," *Appl. Phys. Lett.*, vol. 97, no. 10, p. 102509, Sep. 2010.

[119] A. Kardakova *et al.*, "The electron-phonon relaxation time in thin

superconducting titanium nitride films," *Appl. Phys. Lett.*, vol. 103, no. 25, p. 252602, Dec. 2013.

[120] B. M. McSkimming, A. Alexander, M. H. Samuels, B. Arey, I. Arslan, and C. J. K. Richardson, "Metamorphic growth of relaxed single crystalline aluminum on silicon (111)," *J. Vac. Sci. Technol. A Vacuum, Surfaces, Film.*, vol. 35, no. 2, p. 021401, Mar. 2017.

[121] C. J. K. Richardson, A. Alexander, C. G. Weddle, B. Arey, and M. Olszta, "Low-loss superconducting titanium nitride grown using plasma-assisted molecular beam epitaxy," *J. Appl. Phys.*, vol. 127, no. 23, p. 235302, Jun. 2020.

[122] M. I. Faley, Y. Liu, and R. E. Dunin-Borkowski, "Titanium nitride as a new prospective material for nanosquids and superconducting nanobridge electronics," *Nanomaterials*, vol. 11, no. 2, pp. 1–12, 2021.

[123] C. Kittel, *Introduction to Solid State Physics*, 8th ed. New York: Wiley, 2004.

[124] W. T. Liao *et al.*, "Scanning tunneling Andreev microscopy of titanium nitride thin films," *Phys. Rev. B*, vol. 100, no. 21, pp. 1–9, 2019.

[125] P. G. De Gennes, "Boundary Effects in Superconductors," *Rev. Mod. Phys.*, vol. 36, no. 1, pp. 225–237, Jan. 1964.

[126] P. G. De Gennes and E. Guyon, "Superconductivity in 'normal' metals," *Phys. Lett.*, vol. 3, no. 4, pp. 168–169, Jan. 1963.

[127] B. Mazin, "Microwave kinetic inductance detectors," California Institute of Technology, 2004.

[128] M. S. Khalil, M. J. A. Stoutimore, F. C. Wellstood, and K. D. Osborn, "An analysis method for asymmetric resonator transmission applied to superconducting devices," *J. Appl. Phys.*, vol. 111, no. 5, p. 054510, Mar. 2012.

[129] P. J. Petersan and S. M. Anlage, "Measurement of resonant frequency and quality factor of microwave resonators: Comparison of methods," *J. Appl. Phys.*, vol. 84, no. 6, pp. 3392–3402, Sep. 1998.

[130] P. J. de Visser, S. Withington, and D. J. Goldie, "Readout-power heating and hysteretic switching between thermal quasiparticle states in kinetic inductance detectors," *J. Appl. Phys.*, vol. 108, no. 11, p. 114504, Dec. 2010.

[131] L. J. Swenson *et al.*, "Operation of a titanium nitride superconducting microresonator detector in the nonlinear regime," *J. Appl. Phys.*, vol. 113, no. 10, p. 104501, Mar. 2013.

[132] A. E. Megrant, "Simulating Quantum Chemical Dynamics with Improved Superconducting Qubits," University of California Santa Barbara, 2016.

[133] P. J. de Visser, J. J. A. Baselmans, P. Diener, S. J. C. Yates, A. Endo, and T. M. Klapwijk, "Number Fluctuations of Sparse Quasiparticles in a Superconductor," *Phys. Rev. Lett.*, vol. 106, no. 16, p. 167004, Apr. 2011.